Title
Ecoclimate: Variations, Interactions, and Teleconnections

Author
Swann, Abigail Lynn Segal

Publication Date
2010

Peer reviewed|Thesis/dissertation

Ecoclimate: Variations, Interactions, and Teleconnections

by

Abigail Lynn Segal Swann

A dissertation submitted in partial satisfaction
of the requirements for the degree of

Doctor of Philosophy

in

Earth and Planetary Science

in the

Graduate Division

of the

University of California, Berkeley

Committee in charge:

Professor Inez Y. Fung, Chair
Professor John C. H. Chiang
Professor William D. Collins

Spring 2010

Ecoclimate: Variations, Interactions, and Teleconnections

Abstract

Ecoclimate: Variations, Interactions, and Teleconnections

by

Abigail Lynn Segal Swann

Doctor of Philosophy in Earth and Planetary Science

University of California, Berkeley

Professor Inez Y. Fung, Chair

Ecosystems are an integral part of climate, interacting with the atmosphere by modifying fluxes of energy, water, momentum, and carbon—processes whose importance varies spatially. This dissertation focuses on the study of ecoclimate – unraveling the complex interactions between ecosystems and climate using a variety of tools including simple models, global scale carbon-climate models, and direct analysis of site-level data.

Using a global climate model we show that transpired water vapor from expanded vegetation in the Arctic contributes greenhouse warming with a magnitude of forcing larger than that from the associated changes in albedo. This mechanism has not been considered in previous studies and here we suggest that it may negate the negative climate feedbacks expected from the surface latent cooling associated with the expansion of deciduous forest.

Additionally we find that large-scale expansion of low albedo mid latitude forests in the model has the ability to increase Northern Hemisphere temperatures, moving the thermal equator northward and thus modifying global circulation patterns. We observe a northward shift of the intertropical convergence zone over Africa suggesting that extratropical vegetation may be partly responsible for the maintenance of precipitation over the Sahara inferred from proxy records of vegetation from ∼6000 Years Ago. The ability of vegetation to effect remote circulation has implications for the role that plants may play in the current climate as well as in climates of the past and the future.

In an analysis of nighttime respiration across the eddy covariance Ameriflux tower network we find a residual signal in respiration resembing seasonal variations in substrate mass after accounting for the effects of temperature and moisture. The prevalence of a mass signal indicates that allowing temperature sensitivity to change over time unphysically attributes variations in mass and moisture to changes in temperature. Using a simple carbon cycle model we show that ecosystems with long turnover times are most sensitive to long period forcing and therefore it will be harder to detect or attribute changes in these systems. This suggests that it may be easier to detect and attribute changes in the Tropics compared to the Boreal forest.

Contents

List of Figures

List of Tables

Acknowledgements

This dissertation is the culmination of research I began as an undergraduate analyzing European eddy covariance flux tower network—an analysis I bring up to date in Chapter 3. I left Berkeley for a two year hiatus in which I earned a Masters degree from Columbia University before returning to spend the next five years working with Inez. I owe much of my decision to stay in science to Inez and I am very grateful for her guidance and support. Inez has been honest and open about the realities of science and of being a scientist. In doing so she has helped me to understand why I am here and how I can make progress forward in my career.

Inez has also shaped my scientific upbringing. I am grateful for the breadth of topics covered by our research group and the tenor of discussion that takes place. Inez has always fostered a great sense of community within our research group, the strength of which is one of the primary reasons I returned to Berkeley for graduate school. This was happily extended to John Chiang's group as well. I wish to thank all members of the Fung and Chiang groups during my tenure at Berkeley for our scientific (and extra-scientific) discussions.

Thanks to my officemates both past and present, Charlie Koven, Phoebe Lam, Jung-Eun Lee, Zan Stine, Nir Krakauer, Chelsea Chandler, Aparna Bamzai, and Junjie Liu. Our office has been full of sunlight, discussion and chatter and it has kept me coming back to work all these years. Thanks in particular to Zan Stine who has accompanied me all the way through the latest iteration of my graduate school trajectory and has been a great scientific companion, especially in these last months as we have both figured out how to write our dissertations.

I want to thank friends from outside of my research group who have provided moral and emotional support at various times throughout the sometimes taxing adventure of grad school, always with an understanding of what I was going through. There have been many, but in particular I wish to thank Miren Vizciano, Kate Hoag, Karrie Weaver, Carmen Goodell, Ingrid Johanson, Jessie Cherry, Miriam Jones, and Shahla Ali.

Samuel Levis and Gordan Bonan have been forthcoming with their time helping me set up, run and understand the NCAR global climate model which was used in Chapters 4 and 5. Scott Doney, Jim Randerson, and Elisabeth Holland have acted as scientific consultants and mentors to me these past years. I look forward to collaborating and interacting with all of them in the future.

Funding was provided by NSF Award ATM-0628678 to the University of California, Berkeley as well as the NASA Earth Systems Science Fellowship. Zan Stine, Miren Vizciano, Jung-Eun Lee, Aparna Bamzai, Percy Link and Andrew Friedman provided comments on various parts of this dissertation. William Collins provided the radiation model used in Chapter 5. Sam Levis, Gordon Bonan, Cecilia Bitz, William Collins, Dan Feldman, and Miren Vizciano provided assistance with model configuration. Miriam Jones provided discussion on the nature of Arctic vegetation and its paleo-extent and P.J. Sellers had many helpful suggestions in his review of the paper published from Chapter 5 [*Swann et al.*, 2010].

Finally I wish to thank my family. Thanks to my parents for being ever supportive and

showing me that the exciting and interesting things are those worth doing. You have taught me to have a passion for crazy projects and adventures—arguably this dissertation is one of them. To Nick, thank you for keeping me well fed and warm when I needed it most. I would not have made it through graduate school without your love, support, and patience.

And, as I've made it this far, not even broken bones could stop me–I wish to thank the broken finger on my left hand for healing quickly enough for me to finish typing this dissertation.

Curriculum Vitæ

Abigail Lynn Segal Swann

Education

2003	University of California Berkeley B.A., Earth and Planetary Science
2005	Columbia University M.A., Earth and Environmental Sciences
2010	University of California Berkeley Ph.D., Earth and Planetary Science

Personal

Born	July 10, 1981, Healdsburg, California

Chapter 1

Introduction to Ecoclimate

1.1 An introduction to Ecoclimate

Ecosystems are an integral part of climate. Changes in ecosystem distributions around the globe, due to either natural or anthropogenic land use and land cover change, directly effect climate. Vegetation interacts with the atmosphere by modifying fluxes of energy, water, momentum, and carbon—processes whose importance varies spatially. In order to understand when, where, and how ecosystems influence climate, this dissertation focuses on unraveling these complex interactions. We use a variety of tools including simple models, global scale carbon-climate models, and direct analysis of site-level data.

This dissertation concerns the study of ecoclimate: the influence of ecosystems on climate and climate on ecosystems. Ecological climatology [*Bonan*, 2002] is the study of ecoclimate, much the way that climatology is the study of climate. Ecoclimate describes the state of the larger ecosystem-climate system, and through the description of the climate state, the hydrological state as well. As a parallel, hydroclimate refers to the interaction between climate and water over land [*Langbein*, 1967], or the interaction between climate and hydrology. An ecosystem is defined as a system of living organisms and their physical environment. This includes the vegetation, soil, animals, and atmosphere. Although the definition of ecosystem includes the physical state of the atmosphere, the actual application of the term is generally restricted to a local environment. Ecoclimate is, in the definition used here, the study of larger scale processes, from regional to global. Plants effect not only their local environment, but the global climate through fluxes of water, energy, momentum, and carbon. This communication with a broader atmosphere extends to the teleconnections discussed, for example, in Chapter 4.

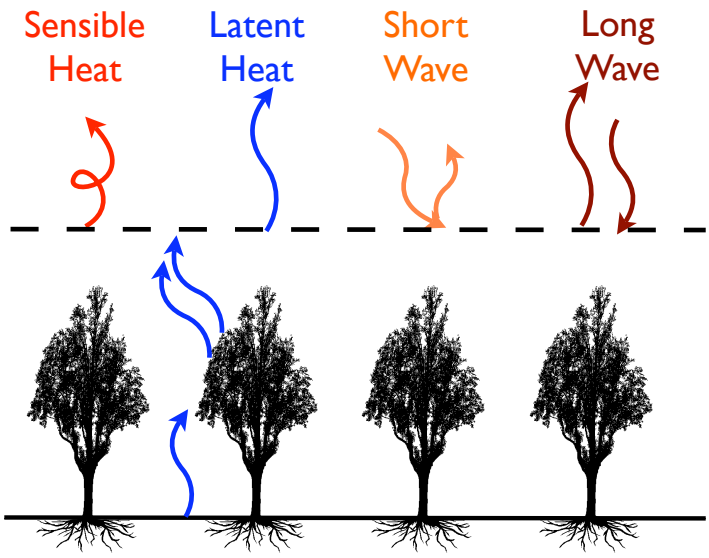

Figure 1.1. **Ecosystem Surface Energy Budget:** Diagram showing energy fluxes between an ecosystem and the atmosphere. Three fluxes of water are shown as contributing to the latent heat flux: transpiration from the vegetation, evaporation from the canopy, and evaporation from the ground surface.

1.2 Interactions Between Ecosystems and Climate

Ecosystems interact with climate through modifications of the energy budget, water budget, and through fluxes of momentum. Net radiation coming into the surface (short wave + long wave) is balanced by sensible and latent heat fluxes (Figure 1.1). Both are sensitive to changes in turbulence, but sensible heat fluxes are ultimately controlled by the gradient in temperature between the surface and the atmosphere while latent heat fluxes are controlled by the gradient in water vapor. There is additionally interplay between fluxes of energy and water. Conversion from high density to low density vegetation (as in the conversion from forest to crop) not only brightens the surface (decreasing the absorption of short wave energy) but also reduces transpiration, shifting the dominant return of energy to the atmosphere from latent to sensible heat. Transpiration is also intimately linked to the uptake of carbon as the same biological process controls both fluxes.

1.2.1 Fluxes of Water and Carbon

Plants require water for photosynthesis, thus the ability to control fluxes of water is of fundamental importance to the plant. This biotic control of water fluxes has implications for the atmosphere. Both the uptake of carbon by plants through photosynthesis and the transpiration, or release, of water by plants are controlled by small valves on leaves called stomata. The ecological modeling community has, through small-scale laboratory study as well as field campaigns, derived an empirical set of equations to model the behavior of

stomata. Many ecosystem and climate models represent the stomatal opening and closing process as a resistance or conductance, as in electrical theory. These equations, the Ball-Berry-Farquhar-Collatz equations [*Ball et al.*, 1987; *Collatz et al.*, 1991, 1992; *Farquhar et al.*, 1980], determine the conductance as the minimum of three processes causing the stomata to close: water limitation, radiation limitation, and the limitation of the rate of regeneration of rubisco (an essential enzyme used as a catalyst in the photosynthetic chemical cycle). The first two limits are controlled directly by climate and hydrology, while the third is controlled by nitrogen dynamics and chemical rates. The opening and closing of stomata is a direct link between ecosystems and climate, determining both the water loss and the carbon uptake of a plant. The modeling of this process is therefore the main way in which carbon and water fluxes from vegetation interact with climate in global climate models.

1.2.2 Fluxes of Energy and Momentum

Energy is exchanged between ecosystems and climate through the absorption of short wave energy, the emission and absorption of long wave energy, and fluxes of sensible and latent heat (Figure 1.1). The measure of the fraction of short-wave radiation absorbed by the surface is described by $(1-\alpha)$, with α representing the fraction of the short wave energy that is reflected. Dark surfaces, such as those of needleleaf trees, have an albedo of $\sim$0.08 indicating a surface where 92% of the incident solar energy is absorbed. Ice, on the other hand, has a bright surface with an albedo of $\sim$0.9 indicating that only 10% of the incident solar energy is absorbed. The albedo of ecosystems varies with vegetation type. Important to this work is the fact that needleleaf evergreen trees tend to be darker ($\alpha \sim 0.08$) than deciduous broadleaf trees ($\alpha \sim 0.10$) as can be seen in Figure 1.2. The total albedo of the surface is a function of both the type of tree and the area covered by leaves as compared to bare ground. Thus the albedo varies seasonally as deciduous trees expose the atmosphere to the underlying ground surface in the winter. Despite the loss of leaves in the winter, we find in Chapter 5, that the addition of deciduous trees reduces springtime albedo before the spring leaf-out as stems cover a bright snowy surface.

Sensible heat fluxes are controlled by the gradient in temperature between the surface and the atmosphere and latent heat fluxes are controlled by the gradient in water vapor. Fluxes of sensible and latent heat are removed from the surface by turbulent mixing. The roughness of the surface is in turn controlled by vegetation characteristics including height. With the addition of trees in the mid latitudes in Chapter 4 we see a large increase in sensible heat fluxes to compensate for an increase in absorbed short wave radiation associated with the darker albedo. Latent heat fluxes originate from three sources in the canopy: transpiration from leaves, evaporation directly from the canopy, and evaporation from the ground surface. Transpiration fluxes are controlled by vegetation and modeled using stomatal conductance (Section 1.2.1).

Figure 1.2. **Arctic Landscape:** Photo showing an Arctic landscape in Denali National Park ($63.5°N$) containing both needleleaf evergreen trees (dark, with low albedo), deciduous broadleaf shrubs and trees (brighter, higher albedo), and tundra vegetation cover.

1.2.3 Competition Between Processes and Teleconnections

Nemani et al. [2003] create a map of the spatial distribution of the limitations of temperature, radiation, and water on carbon uptake by plants. This approach neatly encompasses the control of climate on photosynthesis but the job is not so simple for quantifying the role of ecosystems in climate. This complicates the study of ecoclimate as the influence of climate on ecosystems is local, but the influence of ecosystems on climate operates on multiple scales simultaneously and can have remote impacts. For the case of photosynthesis (as in *Nemani et al.* [2003]) and respiration (as in Chapter 3), the influence of water, temperature, and radiation is inherently a local control although changes in these local controls may be dictated by larger scale climate variations. In the other extreme, local fluxes of carbon are well mixed throughout the atmosphere so that changes in carbon fluxes have a global impact. We investigate the sensitivity of the response of the carbon cycle to climate in Chapter 2.

An additional scale of influence exists in the teleconnections between local variations in energy, water, and momentum fluxes and global climate. Changes in surface temperatures and humidity resulting from local atmosphere-ecosystem changes can, for example, modify surface gradients in pressure resulting in large scale circulation changes and subsequent changes in the distribution of temperature and water vapor. Large-scale changes in Arctic vegetation in a global climate model modify not only the local absorption of solar radiation through changes in albedo, but increase the temperature across the Arctic through long wave radiation from transpired water vapor resulting in feedbacks from the ocean from melting

sea ice (Chapter 5). A large-scale expansion of mid latitude forests is capable of modifying the general circulation of the atmosphere by changing only local surface conditions in a global climate model (Chapter 4). Warming caused by changes in local albedo results in the movement of the "center of energy" northward leading to a shift of precipitation patterns. These teleconnections change local precipitation rates and thus have consequences for the ecosystems in a remote region from the original perturbation.

1.3 Tools for Studying Ecoclimate

1.3.1 Global-scale Coupled Carbon-Climate Models

In Chapters 4 and 5, we show results from climate model experiments run using the community climate model from the National Center for Atmospheric Research (NCAR). The results are from the atmosphere-land-carbon coupled model with either a simplified ocean (mixed layer) or an ocean with fixed surface temperatures (fixed ocean). The atmospheric module attempts to represent the physics of circulation, clouds, rain and the transfer of radiation through the atmosphere. The land model represents soils, vegetation, lakes, glaciers and bare ground as well as keeping track of river runoff. The simplified ocean keeps the depth of the mixed layer and horizontal heat fluxes fixed while allowing the surface temperatures to change. The carbon cycle model tracks carbon as it moves through the live biosphere and the decay pools before it is returned eventually to the atmosphere.

In our simulations the carbon cycle is not fully interactive, that is the CO_2 emitted by the biosphere is treated as an inert tracer and does not contribute to changes in radiative forcing in the atmospheric model. With the full radiative carbon coupling turned off, the climate response to plant productivity is limited only to the biophysical feedbacks. The primary role of the non-radiatively coupled carbon cycle is to predict leaf area so that albedo, surface roughness and transpiration respond to climate. Although vegetation type is fixed in any location, this allows for some dynamic response of the biosphere to changes in climate and hydrology.

This dissertation treats climate models as an experimental tool. The work is theoretical and the climate model is used for experiments to assess the effects of various large-scale changes in vegetation—something not possible in a real life experiment. There are draw backs and uncertainties in using climate models this way, but by focusing on the processes which control the response in the model we gain valuable insight into where to focus our observations in the real world and what we should consider as important influences for ecoclimate. The reader should keep in mind the limitations of climate model simulations when interpreting the results of experiments presented in the following chapters. Some aspects of the model are known to be biased and give a poor representation of the Earth when present day conditions are simulated. For example, the version of the climate model used in this dissertation is too wet in the Middle East and Australia. In some early experiments, we added grasses across

the entire globe and, sure enough, grasses grew very well in Saudi Arabia. This is obviously not a realistic representation, but within the model it is self-consistent—if the model is wet enough, the plants will grow. We have avoided adding vegetation to these regions in any of the experiments shown in this dissertation as the present day representations of the ecoclimate are clearly unrealistic. These regions are easy to identify as the current day climate conditions do not match well with observations and we exclude experiments that highlight truly non-realistic responses of the model. That being said, both the control and experiment contain the same biases so unless vegetation is added in a region with a very large bias, the anomalous response (experiment-control) should not be greatly effected by the inherent biases of the model.

1.3.2 Simple Carbon Cycle Models

We use a simple model of the carbon cycle to quantify the dependence of carbon inventories and fluxes on cyclic climate oscillations. In order to correctly estimate the biologically controlled flux of water from the vegetation to the atmosphere, the land model estimates stomatal conductance (described above). The carbon cycle model (either as a stand-alone simple model or as a component of the full global climate model) takes this estimate of carbon uptake (controlled by stomatal conductance and atmospheric CO_2 concentration) and allocates this carbon to three pools of live carbon: roots, leaves and wood. These live pools have turnover times modulated by temperature, moisture, and plant type, and eventually decay into a series of soil carbon pools which have turnover times ranging from less than one year up to several hundred years. This description holds for both the model presented in Chapter 2 as well as the CASA′ carbon model integrated into the NCAR climate model used in Chapters 4 and 5. The exercise of writing the simplified model in Chapter 2 was an excellent intuition building tool as preparation for understanding the role of CASA′ in the fully coupled climate model. More complicated models of the carbon cycle, such as those explicitly including nitrogen dynamics exist, but they are largely untested and it is not yet clear if their response make sense compared to observations (c.f. *Bonan and Levis* [2010]). We employ the simple, intuitively understandable, and well tested approach of the CASA′ model and find it well suited for experiments such as those in this dissertation.

1.3.3 Flux Tower Data Network

The FLUXNET network of eddy covariance towers [*Baldocchi et al.*, 2001] is globally distributed and covers a range of ecosystems making it a potentially good test-bed for choosing functional forms and parameters to calculate carbon fluxes in models. We ask the question: How can measurements from the Fluxnet network be used for validating global scale carbon cycle models? Our focus is on identifying the factors controlling total ecosystem respiration (R_{eco}) as well as the spatial variability in factors controlling the individual respiratory fluxes.

1.4 Dissertation Structure

Chapter 2 focuses on the temporal memory of the carbon cycle and how it may interact with cyclic climate variations. The decay time of different pools of carbon ranges across the globe from one year to several hundred years. The memory of a carbon pool with a turnover time of 100 years is significantly longer than most observations we have of carbon pool sizes. How then do we detect and attribute observed changes in carbon pools to anthropogenic signals? To begin answering this question we investigate the sensitivity of carbon pools to forcing at different frequencies. We have developed a multi-box model of the terrestrial carbon cycle, the toy carbon model (TCM), forced by climate perturbations on net primary production and turnover times for each carbon pool. With this new tool we can assess the memory of different carbon pools and discuss implications for measurement and detection of carbon pool size changes.

In Chapter 3, we examine the formulation of equations used to estimate ecosystem respiration (autotrophic & heterotropic) and compare modeled respiration to carbon flux measurements from the Ameriflux eddy covariance flux tower network. The net flux of carbon from the biosphere is a balance between photosynthesis, autotrophic respiration by the living biomass, and heterotropic respiration from decomposition of soil carbon by microbes. Temperature, moisture, mass of decomposable material, plant type, and microbial community dynamics are all expected to control the rate of ecosystem respiration but the relative importance of each factor varies geographically. We use Empirical Orthogonal Function analysis to identify spatial teleconnections and relationships between sites with similar controls on carbon flux. We find a residual signal in respiration resembing seasonal variations in substrate mass after accounting for the effects of temperature and moisture on nighttime respiration. The prevalence of a mass signal indicates that allowing temperature sensitivity to change over time unphysically attributes variations in mass and moisture to changes in temperature.

In Chapter 4, we turn to the ecoclimate of mid latitudes. Large-scale expansion of low-albedo mid latitude forests in a global climate model have the ability to increase Northern Hemisphere temperatures, moving the thermal equator northward and thus modifying global circulation patterns. This effects both the local and global climate and carbon cycle. With the resulting shift of the tropical rain belt northward over South America, precipitation over the Amazon decreases resulting in a warming and drying. Furthermore, a northward shift of the tropical rain belt over Africa associated with afforestation in mid latitudes suggests that extratropical vegetation may be partly responsible for the maintenance of precipitation over the Sahara inferred from proxy records of vegetation from $\sim$6000 Years Ago. The ability of vegetation to effect remote circulation has implications for the role that ecosystems may play in the current climate as well as in climates of the past and the future.

In Chapter 5, we investigate the ecoclimate at high latitudes where the treeline is already moving northward in response to warming and climate feedbacks are expected to be large. While land surface albedo change is considered to be the dominant mechanism by which trees directly modify climate at high-latitudes, our findings suggest that the transpired water vapor from expanded vegetation contributes additional greenhouse warming which is further magnified by melting sea ice and additional evaporation from the ocean. In fact, the forcing

from the transpired water vapor is larger than that from changes in albedo. This mechanism has not been considered in previous studies but our work suggests that it may negate the negative climate feedbacks expected from the surface latent cooling associated with the expansion of deciduous forest.

1.5 Future Work

The scope of investigating variations, interactions, and teleconnections of ecoclimate is larger than one dissertation. We will turn first to the Tropics to continue the investigation of the sensitivity of the ecoclimate at different latitudes. The Amazon basin has been shown to exhibit two stable vegetation states in a coupled carbon-climate model with dynamic vegetation [*Oyama and Nobre*, 2003]. Is deforestation capable of pushing the ecoclimate across a threshold where the forest and adjacent agriculture are no longer sustainable? This work will have implications for both scientific goals of understanding the relationship between ecology and climate in the Tropics as well as for societal decision making on the how much deforestation can progress before the remaining agricultural land is no longer viable.

In Chapter 4 we formulate the hypothesis that mid latitude forests may have played a remote role in the relatively wet conditions observed in the Sahel region of Africa ∼6000 years ago. Inferred vegetation distributions from the observation of pollen are not inconsistent with a greater deciduous forest cover in Europe ∼6000 years ago. To test the hypothesis more directly we will run simulations of both vegetation change and orbital changes consistent with that time period. In doing so we can investigate the sensitivity of Tropical precipitation to the extent and location of forest expansion or contraction in mid latitudes.

Pollen records show that deciduous vegetation at high-latitudes expanded rapidly in the wake of retreating ice sheets at the end of the last glacial maximum. Is there a threshold climate at which deciduous vegetation can rapidly expand at high latitudes thus contributing to abrupt warming behavior out of smooth orbital forcing? On what time scale can ecosystems modify the climate? Based on the findings from Chapter 5, namely that deciduous vegetation is able to increase the temperature both through a decrease in albedo and an increase in transpiration derived greenhouse warming, we expect that the vegetation could cause a positive feedback that would help bring Earths climate out of the last ice age. This work will address the role of ecosystems in longer-term climate changes and could help to identify feedback processes which play a role in glacial-interglacial cycles.

Much remains to be explained about the role of ecosystems in climate. For example, the oft-overlooked result from the fourth assessment report of the Inter-governmental Panel on Climate Change (e.g. working group 1 Figure 10.20) showing that for the same CO_2 trajectory the warming is greater in models that have interactive photosynthesis. This implies that some aspect of the interactive vegetation other than carbon flux is amplifying the warming from greenhouse gasses. We continue to be intrigued by the interaction between ecosystems and climate and will work towards understanding how that interaction varies in space and time.

Chapter 2

Sensitivity of Carbon Inventories to Climate Cycles

2.1 Abstract

The terrestrial carbon cycle is forced by climate through changes in temperature, precipitation, and radiation. Climate forcing comes through natural cycles such as El Niño but also through anthropogenic forcing from increasing greenhouse gasses in the atmosphere. Considering that carbon pools carry memories of climate variations and other perturbations for time scales of seasons to centuries, how do we detect an anthropogenic signal in carbon storage? To begin answering this question we investigate the sensitivity of carbon pools to forcing at different frequencies. We have developed a multi-box model of the terrestrial carbon cycle, the toy carbon model (TCM), forced by climate perturbations on net primary production (NPP) and turnover times for each carbon pool. The model is used to explore the background variability of carbon fluxes under "natural" conditions—variability which must be constrained in order to detect any changes in the carbon cycle induced by global warming. We calculate the response function of the TCM to cyclic perturbations and find that carbon pools with long turnover times have a greater sensitivity to perturbations at low frequencies relative to high frequencies. Outside the Tropics, the wood pool has 10x greater amplitude of response to a forcing at 50 years compared to a forcing at 5 years. In the Boreal forest, where the turnover time of carbon is long, the sensitivity to oscillatory forcing is larger than in mid latitude deciduous forests or Tropical forests. This work suggests that the detection of anthropogenically forced changes in the carbon cycle will be difficult in ecosystems with long memory, such as the Boreal forest, but may be possible with long-term measurements in ecosystems such as the Tropical forest.

2.2 Introduction

Natural climate forcing exists on many time scales and, through changes in temperature, precipitation and radiation, has the ability to modulate the net productivity of the biosphere. Anthropogenic climate change due to increases in greenhouse gasses forces climate over long time scales and with a temporal pattern more closely resembling a linear increase. Natural climate forcings such as El Niño or decadal oscillations also influence the biosphere. Anthropogenically forced trends in productivity are occurring in conjunction with the response to all these background variations, and detection of such a trend is complicated by our lack of knowledge of the forcing in the past. This chapter investigates the expected background variability of the biosphere and the sensitivity of the carbon cycle to climate forcing at different frequencies. Constraining the background variability is the first step towards quantifying our ability to detect trends in carbon pools from observations.

2.2.1 Detecting changes in the carbon cycle

The problem of detecting changes in carbon storage, such as the woody biomass of a forest, is analogous to the problem of attributing changes in the atmospheric CO_2 concentration to a particular carbon source or sink. The fluxes into and out of each carbon pool are large compared to the net change in pool size. Currently, carbon inventory of various pools are estimated from several types of measurements. Estimates of leaf density are made from satellite measurements of the absorption bands of chlorophyll through indices such as NDVI [*Tucker*, 1979]. Field measurements of biomass include collecting samples of mass and extrapolating to footprint level scales. Airborne and ground based Lidar is also used to estimate the physical size, and thus the woody biomass of trees [*Dubayah and Drake*, 2000].

These measurements are challenging and frequently require upscaling to obtain global or even regional biomass estimates. Many of the measurements are also limited in time. Ideally, we need long time series of biomass estimates in order to detect and attribute changes in pool size to any particular cause. In this chapter we additionally look at how the record of any pool, i.e. woody biomass, may be obscured by the timescales internal to the terrestrial carbon system.

2.2.2 Cyclic Climate Forcing

Climate oscillations exist on a variety of time scales, from annual to interannual, decadal and multidecadal. Beyond annual variations, we see variability in carbon flux and mass forced by interannual climate modes such as El Niño [*Woodward et al.*, 2008], the North Atlantic Oscillation (NAO, *D'Arrigo et al.* [2003]), Northern Annular Mode (NAM, *Russell and Wallace* [2004]) etc. Decadal oscillations in climate exist (e.g Pacific Decadal Oscillation) and also effect the productivity of the biosphere [*Woodward et al.*, 2008]. Tree ring records in Labrador show oscillations in density associated with the NAO, El Niño, and a multidecadal

oscillation at 40-60 years [*D'Arrigo et al.*, 2003]. Beyond even decadal scales, extended periods (decades to centuries) of prolonged drought have been found in the paleo-record for North America [*Cook et al.*, 2004; *Woodhouse and Overpeck*, 1998]. We know that the turnover time of long-lived carbon pools such as wood, woody debris, and soil range from a few years up to hundreds of years (e.g. *Parton et al.* [1987]). We expect then that the memory of climate oscillations are carried forward in time by the carbon cycle, but how are signals of the past retained by carbon pools in the present? The current mass of carbon is an integral representation of the carbon system in the past. Therefore, the background memory and variability of the carbon cycle must be constrained before we can detect and attribute any changes in carbon mass to current anthropogenic causes.

To investigate the memory of the carbon system we have developed a simple model of the carbon cycle. We force the model with oscillatory forcing at different frequencies and estimate the response of the carbon cycle. This tool can be thought of as a simple way to estimate the feasibility of the detection and attribution of measurements of cycles or trends in carbon pools. It is also an excellent intuition building tool for understanding this formulation of carbon cycle models similar to the formulation in some global climate models (i.e CASA′, *Doney et al.* [2006]).

2.3 Model description

We have developed a simple box model of the terrestrial carbon cycle, the toy carbon model (TCM) with three live (leaves, roots, wood) and three decay (leaves/roots, wood, soil) pools (Figure 2.1). Carbon flow is allocated to the live pools each year as a fraction α of net primary productivity (NPP) and decays out of the live pools over the turnover time τ. Mass decaying from the leaves and roots moves to the fast turnover litter pool (M_2) and mass decaying from the wood pool moves to the slower turnover time woody biomass pool (M_3). The M_2 and M_3 pools also loose mass over a turnover time τ, a fraction of which returns to the atmosphere and the remainder moves to the soil pool. The soil pool is the final stop for carbon which is eventually returned to the atmosphere over turnover time τ_4.

NPP is calculated interactively as a function of leaf mass with an added term to mimic climate-like variations. The decay pools of carbon are a simplified version of the representation of the CASA [*Potter et al.*, 1993] and thus CENTURY model [*Parton et al.*, 1987, 1988]. NPP calculations are based on the light use efficiency model of primary productivity [*Monteith*, 1972, 1977] where:

$$NPP = \epsilon \cdot APAR \tag{2.1}$$

$APAR$ is the absorbed radiation in the photosynthetically active wavelengths (PAR) in units of $\frac{MJPAR}{m^2 \cdot yr}$ and ϵ represents the efficiency of converting light into fixed carbon in units of $\frac{gC}{MJPAR}$. APAR can be further broken into components of incident PAR, and the fraction of total PAR (S) absorbed as a function of leaf area index (LAI) in units of $\frac{m^2 leaves}{m^2 ground}$.

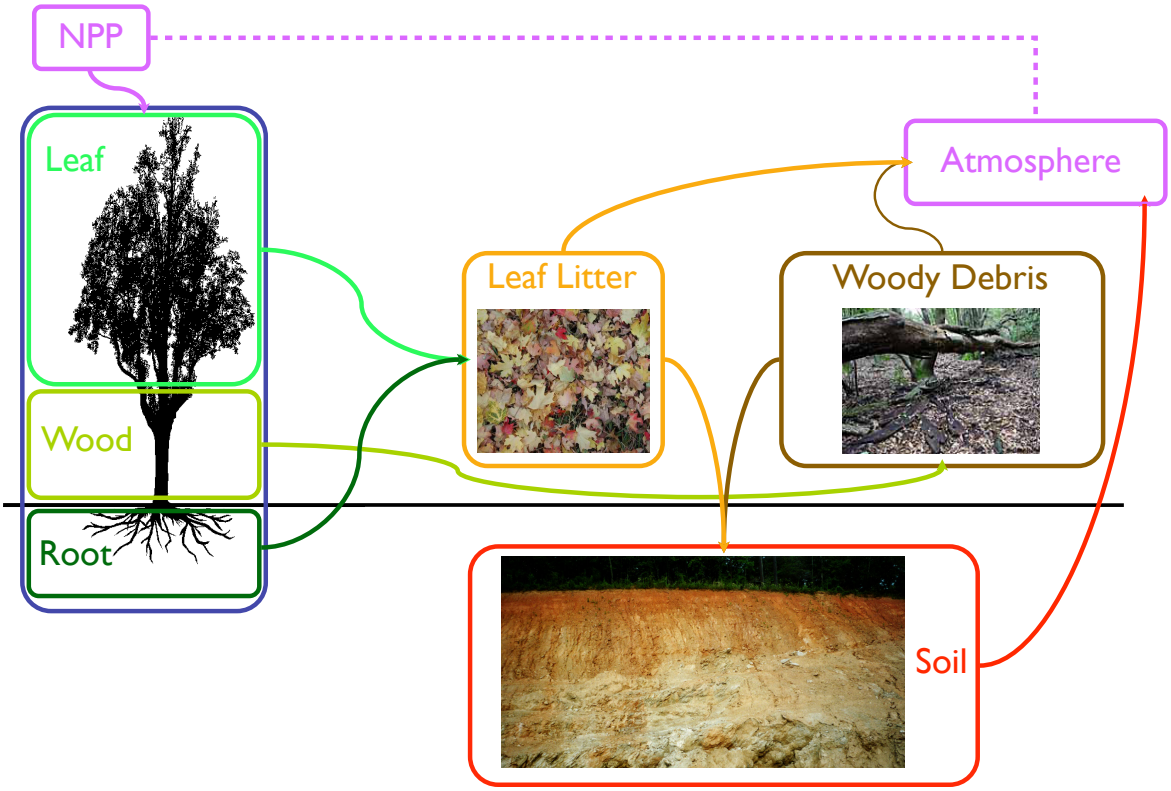

Figure 2.1. **Schematic of the Toy Carbon Model (TCM):** Arrows represent the flow of carbon between pools in the TCM. Three live pools (leaves, roots, and wood) and three decay pools (leaf litter, woody debris, and soil) are represented.

	SLA (m2/gC)	alpha$_n$	epsilon	S (MJ PAR)	NPPmean (gC/m2/yr)
Tropical	0.025	0.0683	0.50	2500	1.83E+10
Mid Lat Decid.	0.030	0.1047	0.50	2500	4.93E+09
Boreal	0.010	0.1164	0.50	2500	1.49E+09

Table 2.1. **Parameter Values:** Parameters used in the TCM for three ecosystem types.

$$APAR = S \cdot (1 - e^{-LAI}) \tag{2.2}$$

Leaf area is calculated as a function of the mass of leaves available in the leaf pool (M_L) and the specific leaf area (SLA) which converts mass of leaves to area of leaves in units of $\frac{m^2 leaf}{gC}$

$$LAI = M_L \cdot SLA \tag{2.3}$$

Combining Equations 2.1-2.3 we have a formulation for NPP as a dynamical term that is a function of the mass of the leaf pool and a climate term that scales between 0 and the magnitude of NPP:

$$NPP = \epsilon \cdot S \cdot (1 - e^{M_L \cdot SLA}) \cdot (1 + \alpha_n \cdot R_n) \tag{2.4}$$

The final term (R_n) simulates the effect of climate variations on NPP directly and will be investigated in this work as

$$R_n = sin(\omega t) \tag{2.5}$$

with maximum amplitude α_n fraction of the dynamical term. α_n represents the scale of variability in NPP. In the model experiments described here, α_n is set by the scale of variance in NPP compared to the mean NPP in the 1000 year coupled carbon cycle climate model run of *Doney et al.* [2006]. α_n could also be varied to investigate the dependence of the carbon cycle on the magnitude of variance, but we leave this branch of experiments for later work. As the climate forcing is specified, the ϵ term can be considered as a maximum efficiency reached only when the climate conditions are best for photosynthesis.

Several parameters are fixed throughout the calculations including light use efficiency ($\epsilon = 0.5\frac{gC}{MJPAR}$), total incident PAR ($S = 2500\frac{MJPAR}{m^2 yr}$), and specific leaf area (SLA) (Table 2.1). The values for SLA are derived from *Dickinson et al.* [1998]. The 1000 year coupled carbon cycle climate model run of *Doney et al.* [2006] is used to find the characteristics of NPP for different plant types. The area weighted global mean NPP time series is calculated for each plant type in the model and then used to find the mean value, variance, range and spectra. The initial NPP value is set as the mean from the 1000 year run, and α_n is set to the range of NPP for each plant type represented (Table 2.1).

	Leaves	Roots	Wood	Litter	Woody Debris	Soil
Tropical	2	2	5	2	20	10
Mid Lat Decid.	2	2	30	2	20	50
Boreal	2	2	100	5	20	100

Table 2.2. **Turnover Times:** Turnover time in years used for each carbon pool in the TCM for three ecosystem types.

NPP is allocated evenly among the three live pools with a constant fraction at each time step (α) [*Running and Coughlan*, 1988]. Mortality of live pools and turnover times of decay pools are represented by a turnover time (τ, Table 2.2). Turnover time values for the soil pool are calculated from a weighted mean estimate of the values reported for the CASA model [*Potter et al.*, 1993]. τ_4 is calculated as the weighted mean of turnover times from three soil pools by 10% OLD organic matter 80% SLOW organic matter and 10% soil microbes SM. These values are consistent with estimates from the parameters in the CENTURY model [*Parton et al.*, 1987; *Schimel et al.*, 1994]. τ_2 used directly from the CASA model Metabolic Litter turnover time. τ_3 is set as a constant value for all three ecosystems represented to aid in comparison. τ_3 should be relatively shorter in tropical ecosystems and relatively loner in Boreal ecosystems—perturbations which will be left to future work on the subject. Live carbon mortality rates are set at 2 years for leaves and roots in all ecosystems and as 5 years, 10 years, and 100 years for Tropical forest, mid latitude deciduous forest, and Boreal forest respectively (Table 2.2).

Mass leaving the leaf and root pools move into the leaf litter pool (pool 2) while live wood moves into the woody debris pool (pool 3) (c.f. Figure 2.1). Decay from the leaf litter and woody debris pools is partitioned so that a fraction (γ) is emitted to the atmosphere and the remaining fraction $(1-\gamma)$ is moved to the soil pool (pool 4) over time τ. Parameter α can be adjusted to allocate NPP between the three live pools but is set as 1/3 for these experiments. Parameter γ can be adjusted to direct more or less of the carbon emission from above ground decay pools to the atmosphere and is set as a default at 0.3. As the M_2 pool accumulates the decay from both the root and leaf pools, an γ_2 of 0.3 can be thought of as directing 70% of leaf and root litter decay to the atmosphere while an γ_2 of 0.15 will direct 70% of root litter decay and 100% of leaf litter decay to the atmosphere. This leaves the differential equations for each pool as:

$$\frac{\partial M_L}{\partial t} = \alpha_L \cdot NPP - \frac{M_L}{\tau_L} \tag{2.6}$$

$$\frac{\partial M_W}{\partial t} = \alpha_W \cdot NPP - \frac{M_W}{\tau_W} \tag{2.7}$$

$$\frac{\partial M_2}{\partial t} = \frac{M_L + M_R}{\tau_L} - \gamma_2 \cdot \frac{M_2}{\tau_2} - (1-\gamma_2) \cdot \frac{M_2}{\tau_2} \tag{2.8}$$

$$\frac{\partial M_3}{\partial t} = \frac{M_W}{\tau_W} - \gamma_3 \cdot \frac{M_3}{\tau_3} - (1 - \gamma_3) \cdot \frac{M_3}{\tau_3} \tag{2.9}$$

$$\frac{\partial M_4}{\partial t} = \gamma_2 \cdot \frac{M_2}{\tau_2} + \gamma_3 \cdot \frac{M_3}{\tau_3} - \frac{M_4}{\tau_4} \tag{2.10}$$

The initial values of each live pool are set to the steady state value which depends on the turnover time of leaves, allocation to the leaf pool, and the initial NPP so that for leaves:

$$M_{L0} = \alpha_L \cdot NPP_0 \cdot \tau_L \tag{2.11}$$

The initial value NPP_0 is set to the global mean value of that plant type from the 1000 year coupled carbon cycle climate model run of *Doney et al.* [2006] shown in Table 2.1.

The TCM can represent any global ecosystem by adjusting the turnover times of each pool as well as the α_n representing the range in NPP compared to the mean, SLA, incident solar radiation (S) and the initial NPP. In this chapter we simulate 3 ecosystems: Tropical forests, mid latitude deciduous forests, and Boreal forests. The values chosen for the above parameters are listed in Table 2.1.

We calculate response curves to assess the sensitivity of the carbon cycle to cyclic forcing at a variety of frequencies. Each value in the response curve is calculated by running the model with an oscillatory climate term (R_n, Equation 2.5) at a particular frequency. The model is run for 1000 years with 400 time steps per year and the first 400 years are discarded as spin-up. The remaining 600 years are used to calculate the Fourier transform and find the amplitude response of the model at that forcing frequency.

2.4 Model Response to Cyclic Forcing

The response of the TCM to a single forcing frequency is characterized by a low background spectrum and a large peak at the forcing frequency (Figure 2.2). The broad background spectrum (Figure 2.2b) has more power in the decay pools (i.e. soil) as opposed to the live pools (i.e. wood) as the downstream pools accumulate memory from all timescales in the pools upstream. The background spectrum is constant between simulations with different forcing frequencies save for the peak at the forcing frequency (Figure 2.2c). This implies that the shape of the response is a function of the parameters and setup of the model as opposed to the input forcing.

If we consider the amplitude of the peak at the forcing frequency, the magnitude of the response for any pool is a function of the turnover time of that pool and the aggregated memory from the turnover time of the pools upstream. If we plot the response amplitude as a function of forcing frequency at the forcing frequency only (Figure 2.3), we see that farther downstream in the carbon cycle (i.e. soil, red line Figure 2.3) the response is relatively larger

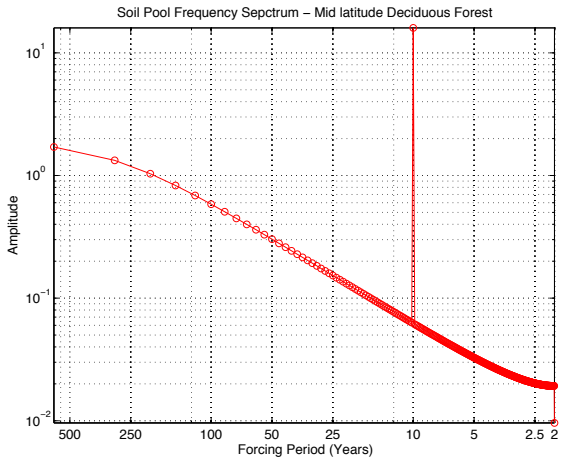

(a) Frequency Spectrum of the Soil Pool

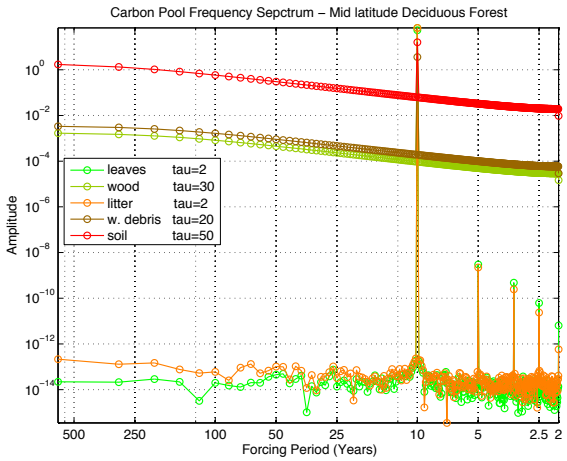

(b) Frequency Spectrum of all Pools

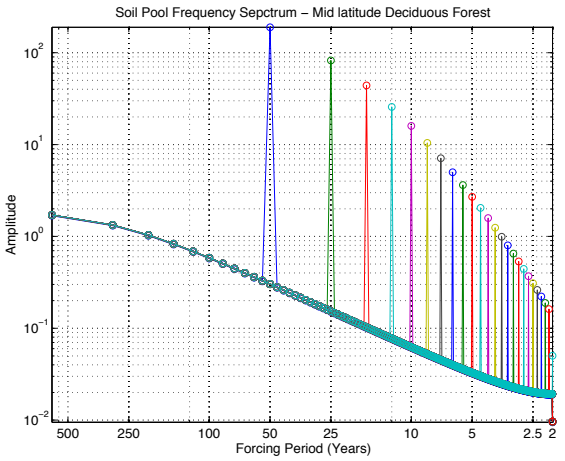

(c) Spectrum at all Forcing Frequencies

Figure 2.2. **Frequency Response to Forcing**. Frequency spectra of the response of **(a)** the soil carbon pool and **(b)** all carbon pools in the TCM to a cyclic forcing at a period of 10 years. The red line in (a) is equivalent to the red line in (b). **(c)** Frequency spectra of the soil pool to forcing at a range of frequencies showing that the red background variability is constant while only the peak at the forcing period moves between experiments.

to long period (low frequency) variations in forcing and less sensitive to short period (high frequency) variations. This means that a recent perturbation in carbon flux will be harder to identify in pools that have greater sensitivity to low frequency forcing.

In comparing our three forest types, Tropical forest, mid latitude deciduous forest and Boreal forest, the main difference is in the turnover time and memory of the carbon pools. From the observations of the TCM above, this suggests that the Boreal forest will be more sensitive to long period (low frequency) forcing than the other ecosystems represented. In fact, live, dead and total carbon all show the highest sensitivity to forcing at any frequency in the Boreal forest with both elevated sensitivity at low frequencies and a diminished damping at high frequencies (Figure 2.4). This is not the only difference between the forests in our model, but it is likely the most important for the sensitivity of the response.

The amplitude of the response of live, dead, and total carbon increases with longer period forcing to the edge of our calculation regime (Figure 2.4). In the live carbon pool, we see that the sensitivity begins to flatten at longer periods, particularly for the Tropical forest (Figure 2.4a, green solid line). The leaf pool has the shortest turnover time and, therefore, the least memory of past variations in carbon assimilation. The response of the leaf pool with a turnover time of two years (Figure 2.5a) begins to flatten out at about 10 years forcing period – or about 5 times the turnover time. In contrast, the live wood pool (Figure 2.5b) shows an increasing response to long period oscillations (at least up to the limit of our response function calculation) for mid latitude deciduous forests ($\tau_W = 30$) and Boreal forests ($\tau_W = 100$) but just begins to flatten out for Tropical forest ($\tau_W = 5$) at about 25 years, or 5x the turnover time. This suggests that the wood pool is more sensitive to longer period forcing variability than the leaves. If we consider the turnover time as the timescale of memory for a given carbon pool, it makes sense that the wood pool, which is longer lived than leaves, would be more sensitive to variations at lower frequencies. And yet, the idea that wood is relatively more sensitive to centennial or even decadal oscillations than El Niño scale oscillations is not entirely obvious.

The sensitivity of a live carbon pool to long period forcing is limited to about 5 times the residence time of that pool. Up to that timescale however, the sensitivity to forcing at these long periods increases. For example, the response amplitude of the wood pool is 5 times larger at 25 years forcing period compared to 5 years forcing period for mid latitude deciduous and Boreal forests (Table 2.3). At 50 years forcing period the response is 10 times larger than at 5 years. For Tropical forests, the response is 4x larger at 25 years and 5.75x larger at 50 years forcing period compared to 5 years. We have limited understanding of climate oscillations and forcing on NPP at these long time scales but the TCM implies that oscillations at long periods are substantially more important to the carbon pool dynamics that those at shorter time scales, particularly if the ecosystem has long turnover times associated with it.

If we go farther downstream into the carbon cycle, the woody debris pool, or M_3, is fed by the live wood pool as it decays. The woody debris pool shows a steep dependence on all periods calculated with very low sensitivity to short period forcing (Figure 2.6b). The damping of sensitivity to high frequency forcing is reduced in the Boreal forest case despite the turnover time of M_3 being equal in all three ecosystems. This suggests that some frequency dependence is carried from the live wood pool into the woody debris pool,

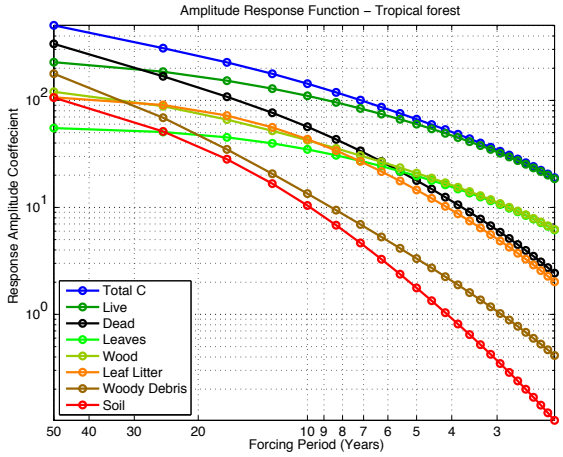

(a) Tropical Forest

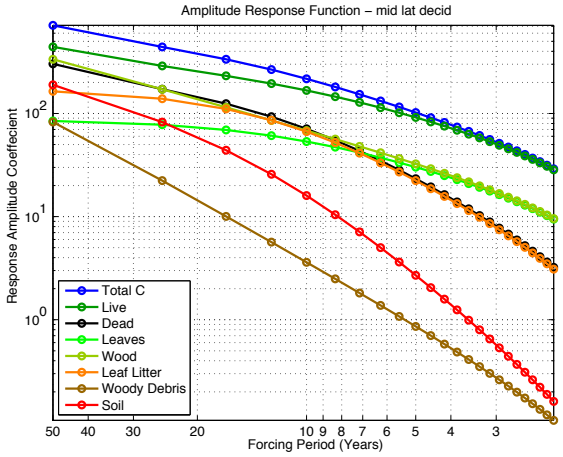

(b) Mid Latitude Deciduous

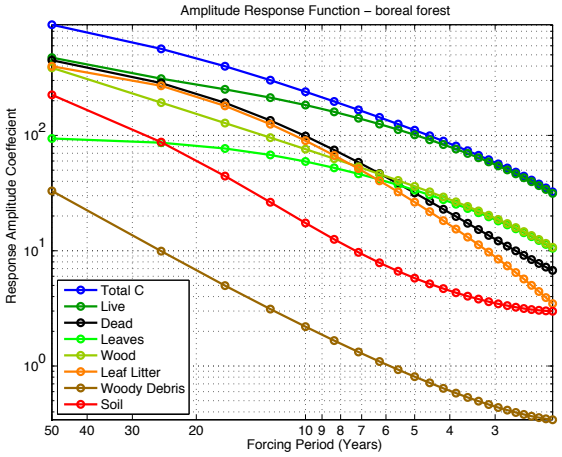

(c) Boreal Forest

Figure 2.3. **Amplitude Response Function in Different Ecosystems**. The relationship between the response amplitude at the forcing frequency and the forcing frequency for each carbon pool in the TCM as well as the aggregated measures of live carbon, dead carbon and total carbon. The relationship is shown for **(a)** Tropical forest, **(b)** mid latitude deciduous forest, and **(c)** Boreal forest.

Forcing Period (years)	50	25	16.67	12.5	10	8.33	7.14	6.25	5.56	5
Tropical	5.75	4.22	3.17	2.49	2.03	1.70	1.46	1.27	1.12	1.00
Mid Lat Decid.	10.33	5.29	3.53	2.64	2.10	1.74	1.48	1.28	1.13	1.00
Boreal	10.66	5.33	3.54	2.65	2.10	1.74	1.48	1.28	1.13	1.00

Table 2.3. **Relative Amplitude Response:** The relative amplitude response to forcing at various periods compared to the response to a forcing at 5 years.

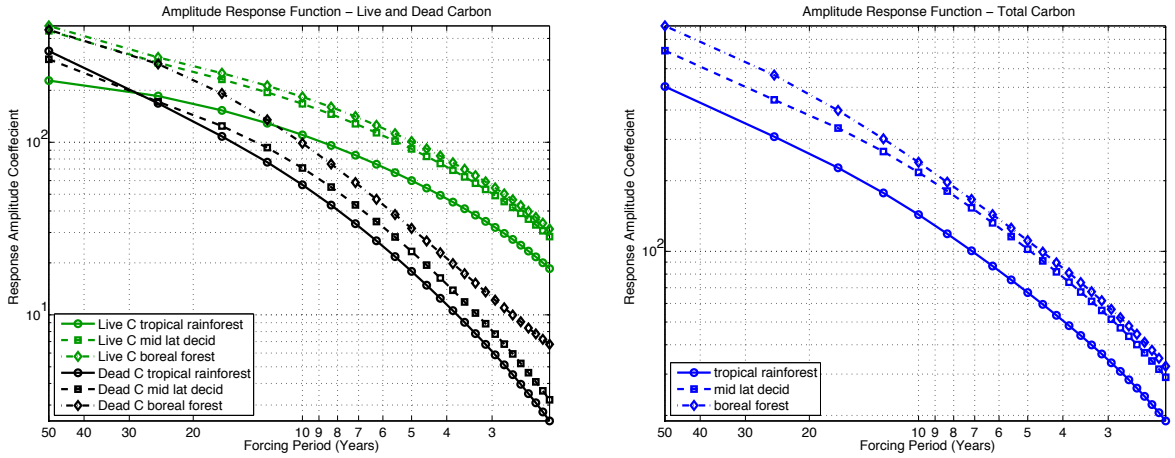

(a) Live and Dead Carbon (b) Total Carbon

Figure 2.4. **Amplitude Response Function for Live, Decay and Total Carbon**. **(a)** The relationship between the response amplitude at the forcing frequency and the forcing frequency for the aggregated live (green) and dead (black) carbon pools in the TCM shown for the Tropical forest (solid line), mid latitude deciduous forest (dashed line) and Boreal forest (dashed-dot line). **(b)** The same as (a) for the aggregated pool of total carbon.

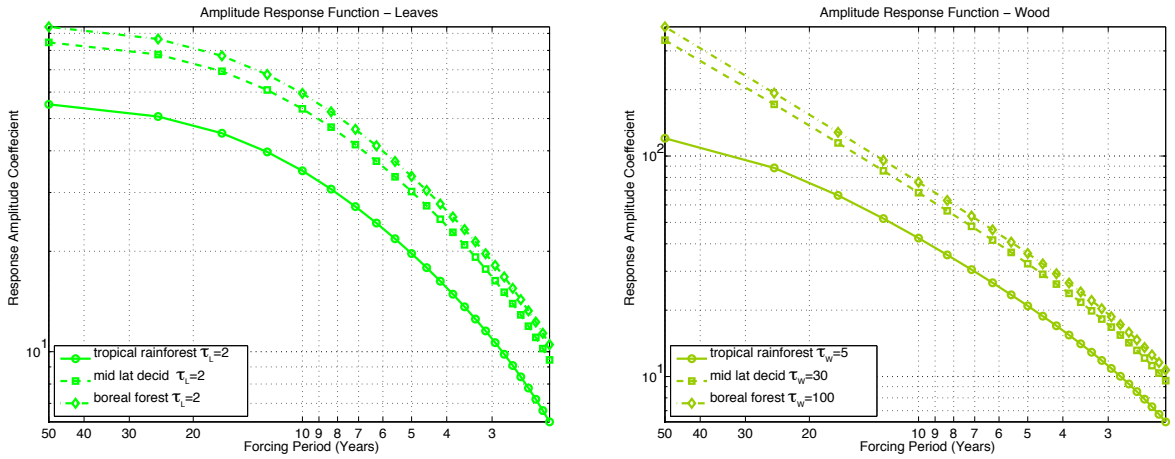

(a) Leaves/Roots (b) Wood

Figure 2.5. **Amplitude Response Function for Live Carbon Pools**. The same as Figure 2.4b for **(a)** the leaf pool and **(b)** the wood pool.

and therefore the turnover times of all pools will influence the sensitivity of carbon storage downstream to variations in input.

2.4.1 Expected Maximum Forcing Timescale

We have established that ecosystems with long turnover times such as the Boreal forest are relatively more sensitive to long period forcing than ecosystems with short turnover times, but the actual response of the earth is a convolution of the sensitivity of a system and the forcing it experiences. What forcing timescale do we expect in each of our model ecosystems? As a first guess we look at the spectrum of NPP as calculated by the coupled climate-carbon cycle model from *Doney et al.* [2006] for plant functional types representing each of our ecosystems (Figure 2.7). The spectrum is calculated for the first and second 500 year periods separately and averaged together in frequency space. What we see in the spectrum of NPP is a red profile, with greater amplitude at lower frequencies. The decorrelation frequency, the frequency at which amplitude stops increasing towards lower frequencies, is defined by the break in the slope of the frequency spectrum. This decorrelation frequency is not well constrained numerically, but qualitatively we see the highest amplitudes at lower frequencies in the Boreal Needleleaf Evergreen (at least 100 years), Temperate Broadleaf Deciduous ($\sim$20 years) and Tropical Broadleaf Evergreen ($\sim$10years) plant types respectively. The TCM is driven by NPP as an input, so if the spectrum of NPP from the global climate model is correct, the Boreal forest is being forced at lower frequencies than the other ecosystems in addition to having greater sensitivity to these frequencies. This suggests that the problem of detection is compounded and attributing changes to anthropogenic signals as outside of the forcing from natural variability is even more difficult than suggested by the TCM.

2.5 Implications

Our model finds that carbon pools are generally more sensitive to long period forcing relative to short period forcing up to periods several times the turnover time. Pools with short turnover times (i.e. leaves) will therefore not be sensitive to long period forcing but wood, dead wood, and soil will be. It is therefore generally easier to detect changes in upstream pools rather than downstream pools. Soil carbon has a red background spectrum as it accumulates the timescales and oscillations in all of the upstream carbon pools. This analysis suggests that carbon pools with long turnover times and pools that are fed by long turnover time pools are most sensitive to long period forcing and less sensitive to short period forcing. There is probably an upper limit to this timescale of sensitivity, saturating at about 5x the longest turnover time. Although we expect that variations on time scales longer than 100 years are smaller than those at shorter time scales, this model implies that forcing at these long time scales results in larger response amplitudes so that the response to a forcing at 50 years is up to 10x larger than the response to a forcing at 5 years. Ecosystems with longer turnover times are more sensitive to long period forcing and suggesting that it

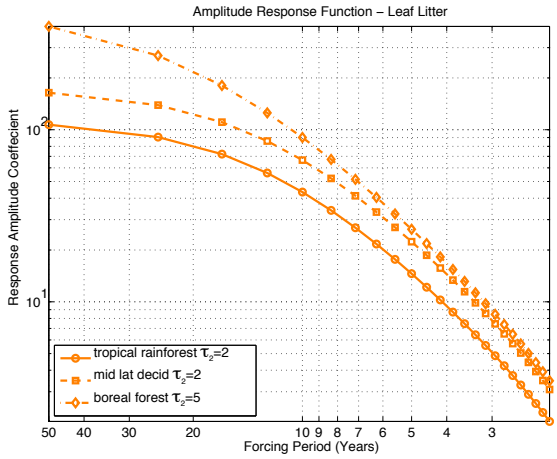

(a) Leaf Litter

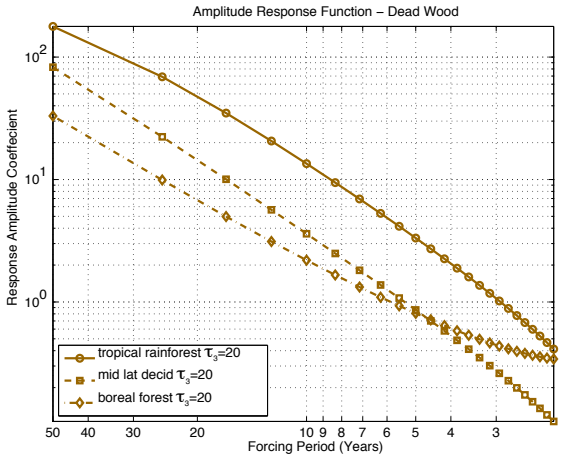

(b) Woody Debris

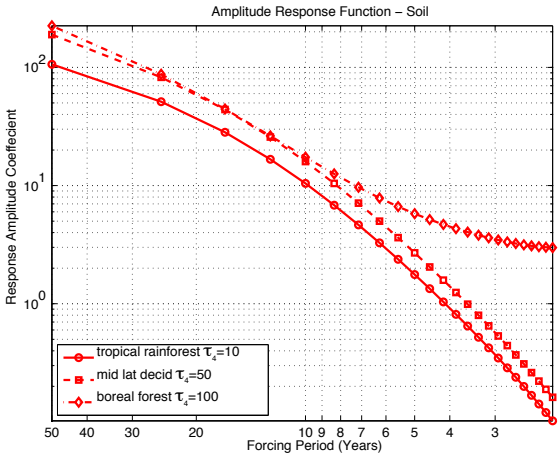

(c) Soil

Figure 2.6. **Amplitude Response Function for Decay Carbon Pools**. The same as Figure 2.4b for **(a)** the leaf litter pool (M_2), **(b)** the woody debris pool (M_3), and **(c)** the soil pool (M_4).

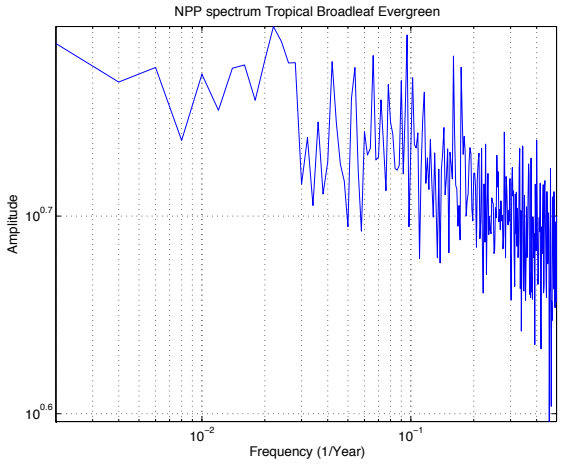

(a) Tropical Broadleaf Evergreen

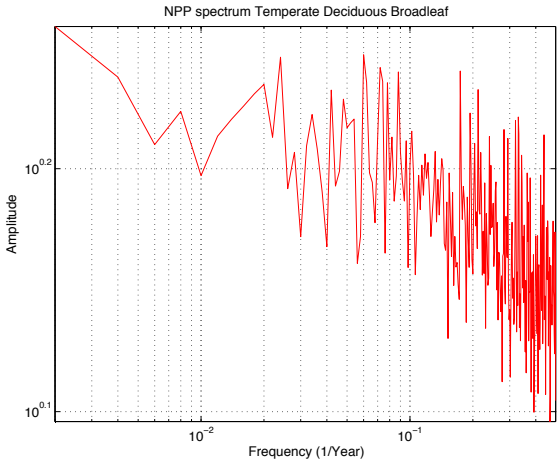

(b) Temperate Broadleaf Deciduous

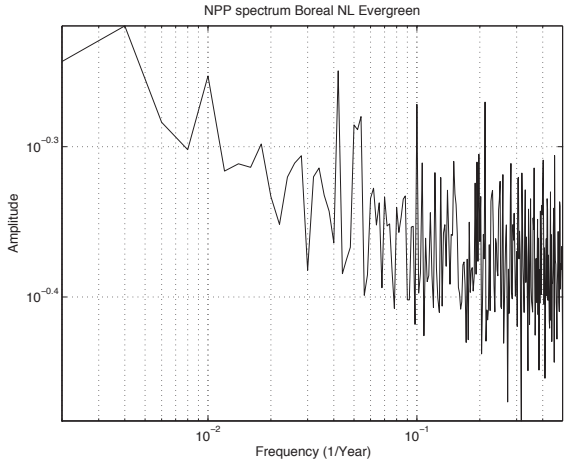

(c) Boreal Needleleaf Evergreen

Figure 2.7. **Frequency Spectrum of NPP**. Frequency spectrum of NPP as calculated by the coupled climate-carbon cycle model from *Doney et al.* [2006] for plant functional types representing each of our ecosystems: **(a)** Tropical Broadleaf Evergreen (Tropical forest), **(b)** Temperate Broadleaf Deciduous (mid latitude deciduous forest), and **(c)** Boreal Needleleaf Evergreen (Boreal forest). The spectrum is calculated from a 1000 year model run for the first and second 500 year periods separately and averaged together in frequency space.

will be easier to detect and attribute changes in the Tropics where turnover times are short compared to other global ecosystems. In contrast, it will be difficult to detect and attribute changes in the Boreal forest carbon cycle as the system is very sensitive to long timescale variations.

Chapter 3

Coherent Variability Across the Ameriflux Carbon Flux Tower Network

3.1 Abstract

Modeling of the terrestrial carbon cycle is a key component to understanding the future trajectory of atmospheric CO_2. Processes controlling the rate of carbon fluxes through photosynthesis and respiration vary spatially across the globe. Temperature, moisture, mass of decomposable material, plant type, and microbial community dynamics are all expected to control the rate of ecosystem respiration, but the relative importance of each factor varies geographically. Here we analyze nighttime carbon fluxes measured from the Ameriflux network of eddy covariance flux towers in order to asses the use of this data for validating model formulations and parameterizations of ecosystem respiration. Empirical Orthogonal Function analysis is used to assess the coherence between sites, identify outliers, and objectively assess the factors controlling this spatial variability. The effect of normalization on the information provided by this method is discussed. Across the network we find that after accounting for temperature and moisture in nighttime respiration a seasonal variation remains unaccounted for. We suggest that the remaining signal is due to changes in the mass available for decomposition. Our analysis finds that a single functional form common in ecosystem models is inadequate to explain observations even with spatially varying parameters.

3.2 Introduction

Since the industrial revolution, atmospheric concentrations of carbon dioxide have been rising at an unprecedented rate to levels not observed anytime in the past four glacial-interglacial cycles, and have created a large potential for climate change [*Solomon et al.*, 2008]. Future concentrations of greenhouse gases are dependent not only on anthropogenic outputs but also on the response of the biosphere and oceans to changing climate and atmospheric composition [*Cox et al.*, 2000; *Friedlingstein et al.*, 2006]. Carbon cycle models have been developed to represent the cycling of carbon through the atmosphere, the terrestrial biosphere, the soil, and the ocean so that ultimately we may understand the fate of these reservoirs in response to changes in anthropogenic fluxes of carbon. Terrestrial carbon cycle models represent the uptake of carbon by vegetation through photosynthesis and the release of carbon through autotrophic respiration from vegetation and heterotrophic respiration from soil. Equations in these models are based largely on functional relationships empirically determined from observations of plants and ecosystems. Many of these measurements are made at small spatial and temporal scales but must be scaled up to the site level or even the global climate model grid size to understand the global cycling of carbon. Validation of carbon cycle models is further hampered by a lack of large-scale data for comparison.

Carbon fluxes from the terrestrial biosphere consist of uptake by the surface through photosynthesis and release of carbon by plants as they grow and maintain living biomass (autotrophic) and by microbes as the digest carbon in the soil through decomposition (heterotrophic). These opposing fluxes are much larger than the difference between them, making it a difficult task to track changes in the net flux. The total net flux of carbon from the land surface is called net ecosystem exchange (NEE). We can therefore represent NEE as the balance between the uptake and release of carbon as:

$$NEE = R_h + R_a - P \tag{3.1}$$

where R_h represents heterotrophic respiration from the soil, R_a represents autotrophic respiration from living plant tissues, and P represents uptake by photosynthesis. NEE is the net effect of the terrestrial role in atmospheric carbon dioxide concentrations. The amount of carbon fixed by vegetation through photosynthesis will be referred to in the form of gross primary productivity (GPP) and is the photosynthetic flux corrected by autotrophic respiration:

$$GPP = R_a - P \tag{3.2}$$

or, alternatively we can solve for GPP as:

$$GPP = NEE - R_h \tag{3.3}$$

where the sign of carbon flux is positive into the atmosphere for all terms. Photosynthesis is the chemical reaction in which chloroplasts in the leaves of plants absorb light in both blue

and red wavelengths to drive a chemical cycle which takes up carbon from the atmosphere and returns oxygen. Except for some very specialized forms present in only a few plant types, photosynthesis only functions while there is sufficient daylight to drive the reactions. At night P goes to zero so that:

$$NEE_{night} = R_h + R_a = R_{eco} \tag{3.4}$$

The NEE at night is therefore equivalent to the sum of the two respiration terms, also called the total ecosystem respiration (R_{eco}). Process-based models treat the carbon flux terms (R_h, R_a, P) separately, but measurements of whole ecosystems cannot differentiate between them. In order to formulate parameters or test process-based models using measurements from scales larger than small chambers, estimates must be made for these fluxes (R_h, R_a, P) in order to separate the measured signal into its process-based parts. For the remainder of this chapter, all references to NEE will refer to nighttime NEE when $NEE \sim R_{eco}$ unless specified otherwise.

In this chapter, we focus on carbon fluxes measured by a network of towers across the globe. The FLUXNET network of eddy covariance towers [*Baldocchi et al.*, 2001] is globally distributed and covers a range of ecosystems making it a potentially good test-bed for choosing functional forms and parameters to calculate carbon fluxes in models. In this chapter we ask the question: How can measurements from the FLUXNET network be used for validating global scale carbon cycle models? To begin answering this question we investigate the variability represented by the spatial distribution of sites available in a subset of the FLUXNET network, the Ameriflux network (http://public.ornl.gov/ameriflux/). To characterize the network we objectively determine the coherent modes of variability in different fields using an empirical orthogonal function (EOF) analysis. In a parameter study, we test a common functional formulation used to represent respiration in carbon cycle models against measured fluxes of carbon. We use data processing methods that mimic the process-based approach of models. Our focus is on identifying the factors controlling total ecosystem respiration (R_{eco}) as well as the spatial variability in factors controlling the individual respiratory fluxes.

3.2.1 Modeling Perspective

From a modeling perspective, it is essential to identify process-based equations and parameters that can be used to estimate carbon fluxes based on the factors controlling them. Without a process-based approach, models are unable to simulate conditions outside the range of observations. If the functional form and parameters for those equations are determined for present day conditions, it is assumed that some of these properties will be kept constant as climate change progresses and, by changing the driving variables, we can predict fluxes in the future. In addition to the assumptions of constancy in time, large-scale models must make assumptions about the spatial distribution of both the functional forms and parameters necessary to model the carbon cycle. Models that are applicable over large-scales will most likely hold functional forms for respiration and photosynthesis constant in space while allowing only the parameters driving those equations to change. Identifying both the

appropriate functional forms and spatial variations in parameters to drive carbon flux equations is essential to estimating these fluxes over large spatial scales and into the past and future.

Most regional or global models of heterotrophic respiration (e.g. CENTURY or its derivative, CASA (*Parton et al.* [1987]; *Potter et al.* [1993])) adopt a formulation that partitions soil carbon into multiple pools according to their biogeochemical properties, with fluxes determined by the pool size M and a mean decomposition rate k modulated by temperature and moisture. The temperature and moisture functions $f(T)$ and $g(S)$ are normalized to vary between 0 and 1. We adopt a similar formulation with a single set of functional forms and rates where

$$F = M(t) \cdot k \cdot f(T) \cdot g(S) \tag{3.5}$$

Equation 3.5 can be readily generalized to include autotrophic respiration where M is the living biomass and k is the corresponding maximum respiration rate. To apply this model across the globe, the spatial distribution of both the functional forms and the parameters to drive each equation are required. In this chapter we will investigate using the Ameriflux network of carbon flux measurements to find parameters and assess the ability of datasets like this in determining parameters to drive models of respiration across the globe.

3.3 Introduction to FLUXNET

The Ameriflux network is a subset of the global FLUXNET network—a collection of tower sites measuring net carbon flux using the eddy covariance method as well as meteorological variables [*Baldocchi et al.*, 2001]. The sites are run by independent groups with a loose protocol for measurement technique and strategy. Access to the full global FLUXNET database is restricted to principal investigators for most sites although sites are increasingly being made available to the public (http://www.fluxdata.org/). Ameriflux data is publically available through Oak Ridge National Laboratory (http://public.ornl.gov/ameriflux/). The publicly available data files for the Ameriflux network are generally updated when errors are discovered, but the files were not identified by version numbers until recently. This makes it difficult to reproduce results unless the exact version of the data is known. The data used in this analysis was downloaded from the Ameriflux database at Oak Ridge on October 29th, 2009. There were 59 sites with sufficient data to analyze in the version we obtained. Site names, basic site information, and the version number of the data (if one was provided in the dataset) are shown in Table 3.1, sites are mapped in Figure 3.1, and a map of plant types is shown in Figure 3.2.

The eddy covariance method involves measuring the concentration of a gas at high frequency time intervals as well as the three-dimensional wind speed in order to calculate the covariance of vertical wind speed and concentration to determine the flux. The method as-

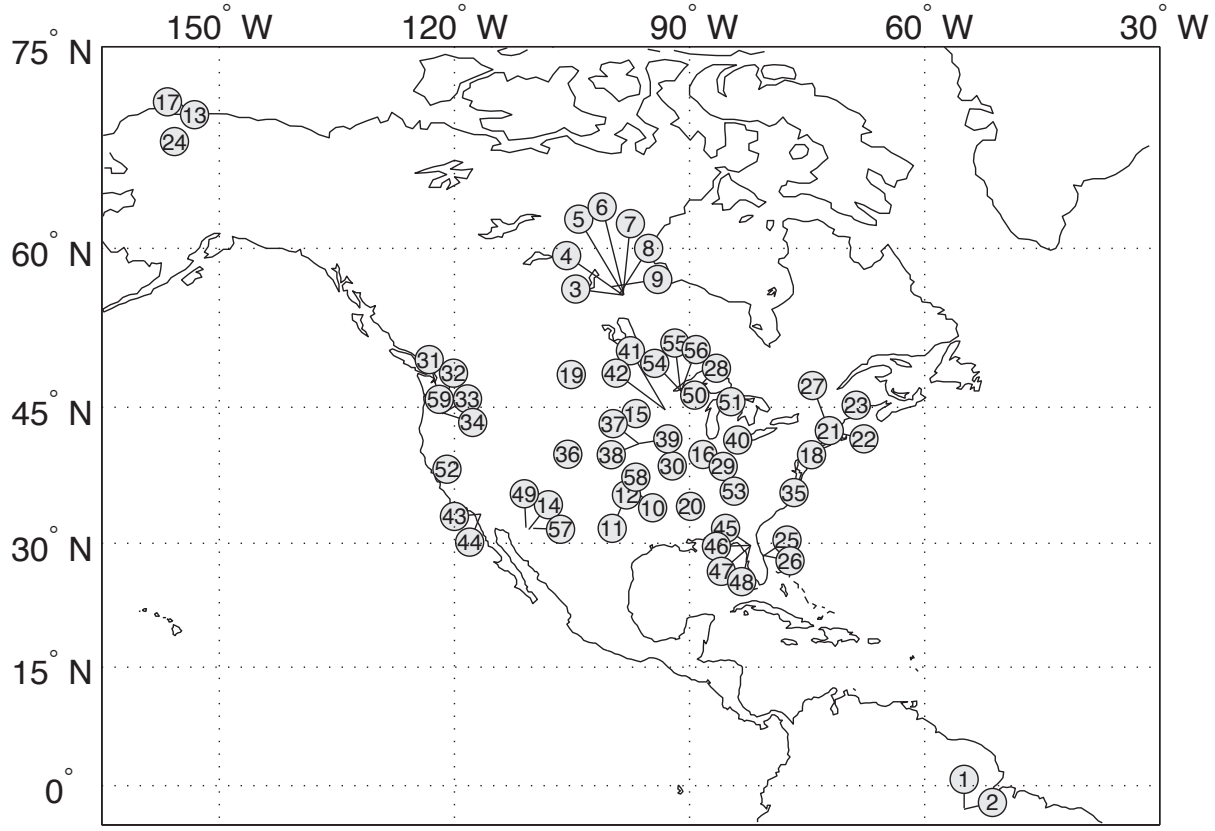

Figure 3.1. **Map of Site Numbers:** A map of Ameriflux sites used in this analysis is shown with a number corresponding to each site as listed in Table 3.1.

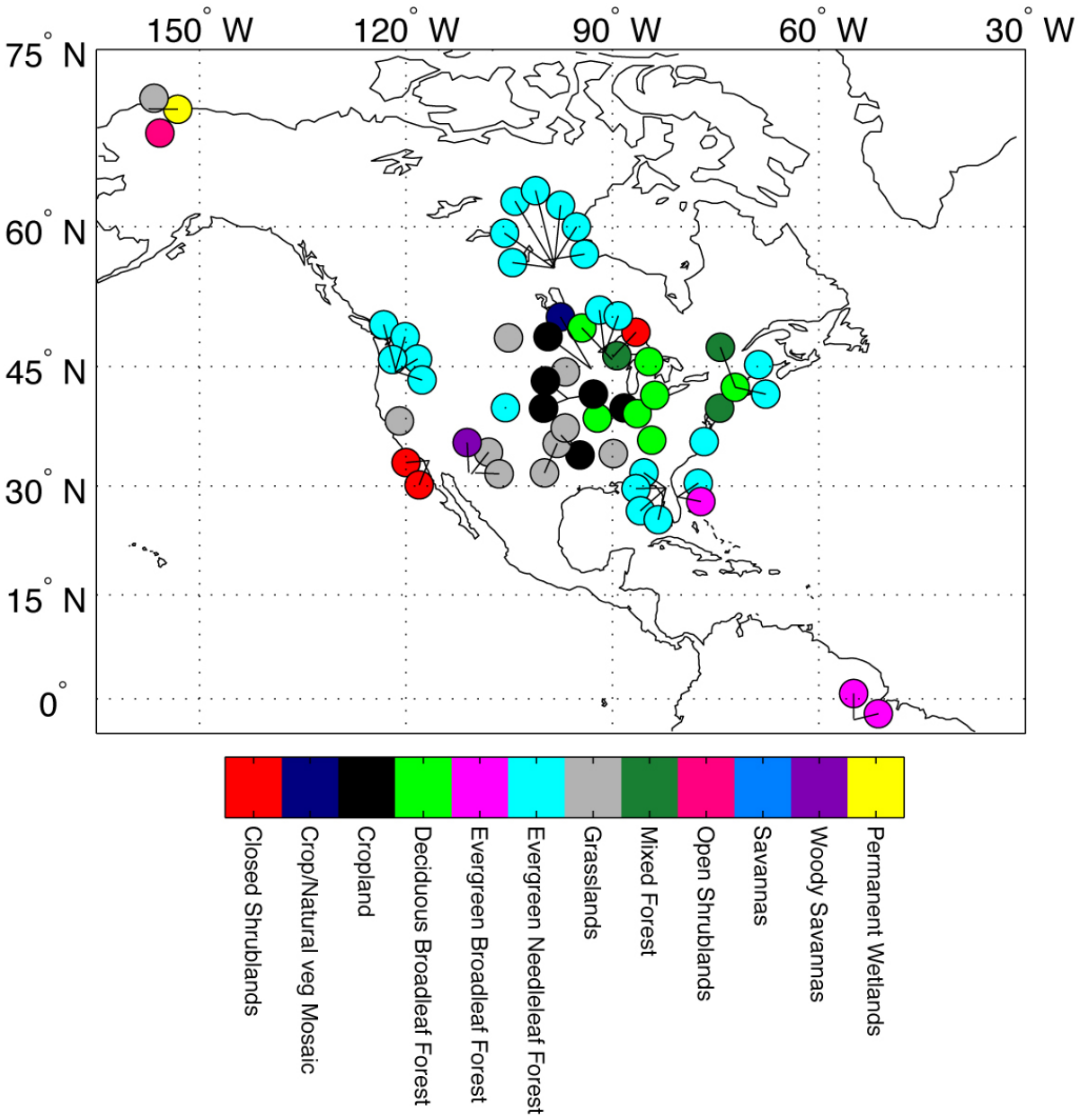

Figure 3.2. **Map of Plant Types:** A map of Ameriflux sites used in this analysis is shown with the plant type at each site signified by the color of the marker.

sumes that the mean vertical velocity wind speed is zero on time scales longer than turbulent eddies (∼30 min). The flux of a species (in our case CO_2) is then calculated as

$$F = \overline{\rho}_a \cdot \overline{\omega' c'} \tag{3.6}$$

where primes denote fluctuations from mean over timescales longer than the eddies, c is concentration, ω is vertical velocity, ρ_a is the mass of air, and F is the resulting flux [*Baldocchi et al.*, 1988].

The eddy covariance method observes the net exchange of carbon between the land surface and the atmosphere at scales up to ∼1km. On a footprint scale, these towers provide carbon, water, and energy flux measurements which can be used to study the ecosystem local to the tower, or in aggregate, ecosystems in general. Ecosystem carbon flux measurements are difficult to make and are often made on very small spatial and temporal scale (i.e. leaf chambers). Eddy covariance flux towers integrate over a slightly larger area and timescale. As the network is globally distributed, the data could be used for comparison with global scale ecosystem models. In this chapter we investigate the potential for using carbon flux measurements from these towers to validate ecosystem models.

The eddy covariance method relies on the assumption of turbulent mixing, and so, under low wind conditions, the presence of a stably stratified atmospheric boundary layer (often at night) traps the air below the sensors leading to an underestimation of the fluxes. Lateral advection, especially episodic downslope flow in the presence of topography, can also alter nighttime fluxes and affect the interpretation of the tower measurements in the context of one-dimensional budgets. Lateral advection cannot be directly detected from the tower data itself, however stable stratification can be inferred. Turbulent velocities (u*), are used as a proxy for still, stratified air and values of u* below a threshold are excluded [*Aubinet et al.*, 2000]. Gaps in the data are filled when the time period of the gap is short and is estimated for the missing values using averages made from neighboring time periods (see *Reichstein et al.* [2005]).

Due to the global distribution of eddy flux tower sites, the FLUXNET network is potentially useful for validating global models (e.g. *Jung et al.* [2009]). The Ameriflux network reports both NEE and GPP at each tower site, the former is a direct measurement while the later is a calculated product. The estimation of GPP from measured fluxes is calculated from equation 3.3 and requires empirical estimates of R_h and R_a during daytime hours. The daytime R_h and R_a fluxes are calculated using an Arrhenius-type equation (Equation 3.12) with a different temperature sensitivity calculated for each day on a running window of 30 days [*Reichstein et al.*, 2003]. This allows the temperature sensitivity to change over time to account for non-temperature related effects. This approach is empirically-based rather than process-based as the temperature sensitivity itself is thought to be at least relatively constant [*Davidson and Janssens*, 2006], making the estimate of respiration and, by equation 3.3, GPP, less useful for evaluating process-based models.

The Ameriflux dataset has many gaps in the time series of data at each site. Small gaps are filled during pre-processing by the procedures described in *Reichstein et al.* [2005], but larger gaps still remain. In any given year, only a small subset of the network has

Num	CEIP	Site Name	Country	State	Latitude	Longitude	IGBP Classification	Site Contact	Version	Contact Email
1	BRSa1	LBA Tapajos KM67 Mature Forest	Brazil		-2.86	-54.96	Evergreen broadleaf forest	Steven Wofsy		wofsy@fas.harvard.edu
2	BRSa3	LBA Tapajos KM83 Logged Forest	Brazil		-3.02	-54.97	Evergreen broadleaf forest	Mike Goulden		mgoulden@uci.edu
3	CANS1	UCI 1850	Canada	MB	55.88	-98.48	Evergreen Needleleaf Forest	Mike Goulden		mgoulden@uci.edu
4	CANS2	UCI 1930	Canada	MB	55.91	-98.52	Evergreen Needleleaf Forest	Mike Goulden		mgoulden@uci.edu
5	CANS3	UCI 1964	Canada	MB	55.91	-98.38	Evergreen Needleleaf Forest	Mike Goulden		mgoulden@uci.edu
6	CANS4	UCI 1964wet	Canada	MB	55.91	-98.38	Evergreen Needleleaf Forest	Mike Goulden		mgoulden@uci.edu
7	CANS5	UCI 1981	Canada	MB	55.86	-98.49	Evergreen Needleleaf Forest	Mike Goulden		mgoulden@uci.edu
8	CANS6	UCI 1989	Canada	MB	55.92	-98.96	Evergreen Needleleaf Forest	Mike Goulden		mgoulden@uci.edu
9	CANS7	UCI 1998	Canada	MB	56.64	-99.95	Evergreen Needleleaf Forest	Mike Goulden		mgoulden@uci.edu
10	USARM	ARM SGP Main	USA	OK	36.61	-97.49	Croplands	Margaret Torn		mstorn@lbl.gov
11	USARb	ARM SGP Burn	USA	OK	35.55	-98.04	Grasslands	Margaret Torn	V001	mstorn@lbl.gov
12	USARc	ARM SGP Control	USA	OK	35.55	-98.04	Grasslands	Marc Fischer	V001	mlfischer@lbl.gov
13	USAtq	Atqasuk	USA	AK	70.47	-157.41	Permanent Wetlands	Walter Oechel		oechel@sunstroke.sdsu.edu
14	USAud	Audubon Research Ranch	USA	AZ	31.59	-110.51	Grasslands	Tilden Meyers	V002	tilden.meyers@noaa.gov
15	USBkg	Brookings	USA	SD	44.35	-96.84	Grasslands	Tilden Meyers	V003	tilden.meyers@noaa.gov
16	USBo1	Bondville	USA	IL	40.01	-88.29	Croplands	Tilden Meyers		tilden.meyers@noaa.gov
17	USBrw	Barrow	USA	AK	71.32	-156.63	Grasslands	Walter Oechel		oechel@sunstroke.sdsu.edu
18	USDix	Fort Dix	USA	NJ	39.97	-74.43	Mixed forest	Kenneth Clark		kennethclark@fs.fed.us
19	USFPe	Fort Peck	USA	MT	48.31	-105.10	Grasslands	Tilden Meyers		tilden.meyers@noaa.gov
20	USGoo	Goodwin Creek	USA	MS	34.25	-89.87	Grasslands	Tilden Meyers	V001	tilden.meyers@noaa.gov
21	USHa1	Harvard Forest	USA	MA	42.54	-72.17	Deciduous Broadleaf Forest	J. Munger		jwmunger@seas.harvard.edu
22	USHa2	Harvard Forest Hemlock	USA	MA	42.54	-72.18	Evergreen Needleleaf Forest	Julian Hadley		jhadley@fas.harvard.edu
23	USHo2	Howland Forest West Tower	USA	ME	45.21	-68.75	Evergreen needleleaf forest	David Hollinger		davidh@hypatia.unh.edu
24	USIvo	Ivotuk	USA	AK	68.49	-155.75	Open shrublands	Walter Oechel		oechel@sunstroke.sdsu.edu
25	USKS1	Kennedy Space Center Slash Pine Flatwoods	USA	FL	28.46	-80.67	Evergreen needleleaf forest	Bert Drake		drakeb@si.edu
26	USKS2	Kennedy Space Center Scrub Oak	USA	FL	28.61	-80.67	Evergreen broadleaf forest	Bert Drake		drakeb@si.edu
27	USLPH	Little Prospect Hill	USA	MA	42.54	-72.18	Mixed forest	Julian Hadley		jhadley@fas.harvard.edu
28	USLos	Lost Creek	USA	WI	46.08	-89.98	Closed Shrublands	Paul Bolstad		pbolstad@umn.edu
29	USMMS	Morgan Monroe State Forest	USA	IN	39.32	-86.41	Deciduous broadleaf forest	Danilo Dragoni	V001	ddragoni@indiana.edu
30	USMOz	Missouri Ozark	USA	MO	38.744	-92.2	Deciduous broadleaf forest	Lianhong Gu		lianhong-gu@ornl.gov
31	USMe1	Metolius Eyerly Burn	USA	OR	44.58	-121.50	Evergreen needleleaf forest	Beverly Law		bev.law@oregonstate.edu
32	USMe2	Metolius Intermediate Pine	USA	OR	44.45	-121.56	Evergreen needleleaf forest	Beverly Law		bev.law@oregonstate.edu
33	USMe3	Metolius New Young Pine	USA	OR	44.32	-121.61	Evergreen needleleaf forest	Beverly Law		bev.law@oregonstate.edu
35	USMe5	Metolius First Young Pine	USA	OR	44.44	-121.57	Evergreen needleleaf forest	Beverly Law		bev.law@oregonstate.edu
35	USNC2	North Carolina Loblolly Pine	USA	NC	35.80	-76.67	Evergreen needleleaf forest	Jiquan Chen		jiquan.chen@utoledo.edu
36	USNR1	Niwot Ridge	USA	CO	40.03	-105.55	Evergreen Needleleaf Forest	Russ Monson		russell.monson@colorado.edu
37	USNe1	Mead Irrigated	USA	NE	41.17	-96.48	Croplands	Shashi Verma		sverma1@unl.edu
38	USNe2	Mead Irrigated Rotation	USA	NE	41.16	-96.47	Croplands	Shashi Verma		sverma1@unl.edu
39	USNe3	Mead Rainfed	USA	NE	41.18	-96.44	Croplands	Shashi Verma		sverma1@unl.edu
40	USOho	Ohio Oak Openings	USA	OH	41.55	-83.84	Deciduous broadleaf forest	Jiquan Chen		jiquan.chen@utoledo.edu
41	USRo1	Rosemount G21 Conventional Corn Soybean Rotation	USA	MN	44.71	-93.09	Cropland/natural vegetation mosaic	Timothy Griffis		tgriffis@soils.umn.edu
42	USRo3	Rosemount G19 Alternative Corn Soybean Rotation	USA	MN	44.72	-93.09	Croplands	Timothy Griffis		tgriffis@soils.umn.edu
43	USSO3	Sky Oaks Young	USA	CA	33.38	-116.62	Closed shrublands	Walter Oechel		oechel@sunstroke.sdsu.edu
44	USSO4	Sky Oaks New	USA	CA	33.38	-116.64	Closed shrublands	Walter Oechel		oechel@sunstroke.sdsu.edu
45	USSP1	Austin Cary	USA	FL	29.74	-82.22	Evergreen needleleaf forest	Timothy Martin		tamartin@ufl.edu
46	USSP2	Mize	USA	FL	29.76	-82.24	Evergreen Needleleaf Forest	Timothy Martin		tamartin@ufl.edu
47	USSP3	Donaldson	USA	FL	29.75	-82.16	Evergreen Needleleaf Forest	Timothy Martin		tamartin@ufl.edu
48	USSP4	Rayonier	USA	FL	29.80	-82.20	Evergreen Needleleaf Forest	Henry Gholz		hlgholz@ufl.edu
49	USSRM	Santa Rita Mesquite Savanna	USA	AZ	31.82	-110.87	Woody Savanna	Russell Scott		russ.scott@ars.usda.gov
50	USSyv	Sylvania Wilderness	USA	MI	46.24	-89.35	Mixed forest	Paul Bolstad		pbolstad@umn.edu
51	USUMB	UMBS	USA	MI	45.56	-84.71	Deciduous Broadleaf Forest	Peter Curtis		curtis.7@osu.edu
52	USVar	Vaira Ranch	USA	CA	38.41	-120.95	Grasslands	Dennis Baldocchi	V003	baldocchi@nature.berkeley.edu
53	USWBW	Walker Branch	USA	TN	35.96	-84.29	Deciduous Broadleaf Forest	Tilden Meyers		tilden.meyers@noaa.gov
54	USWCr	Willow Creek	USA	WI	45.81	-90.08	Deciduous Broadleaf Forest	Paul Bolstad		pbolstad@umn.edu
55	USWi4	Wisconsin Mature Red Pine	USA	WI	46.74	-91.17	Evergreen Needleleaf Forest	Jiquan Chen		jiquan.chen@utoledo.edu
56	USWi9	Wisconsin Young Jack Pine	USA	WI	46.62	-91.08	Evergreen Needleleaf Forest	Jiquan Chen		jiquan.chen@utoledo.edu
57	USWkg	Kendall Grassland	USA	AZ	31.74	-109.94	Grasslands	Russell Scott		russ.scott@ars.usda.gov
58	USWlr	Walnut River	USA	KS	37.52	-96.86	Grasslands	Richard Coulter		rlcoulter@anl.gov
59	USWrc	Wind River Crane Site	USA	WA	45.82	-121.95	Evergreen needleleaf forest	Kyaw Paw U		ktpawu@ucdavis.edu

Table 3.1. **Table of Sites:** Table of sites from the Ameriflux network with sufficient data to be used in this analysis. The table shows the full site name, site acronym, geographic location, latitude, longitude, vegetation type, data version number, and PI email contact. Sites are listed alphabetically and numbered for cross referencing (Figure 3.1).

concurrent data available. Our main focus is on the general variability across the network, so we will focus primarily on the climatology at each site. Although many site-years exist in the dataset, the number of sites with sufficient data available in any given year is limited, and many site time series are discontinuous. We make the best estimate of climatology at each site from all available data. Before averaging into climatology, the data was smoothed with a 10 day running mean to downplay the influence of any given synoptic scale variation.

3.4 Understanding Spatial Variability: EOF Analysis

3.4.1 Time Variability and Seasonality of Temperature and R_{eco}

Although the seasonality of temperature is similar in shape and character across most sites (c.f. Figure 3.3b), the annual march of R_{eco} varies widely. R_{eco} is controlled by temperature, moisture and mass of substrate—factors that vary temporally at a given site. R_{eco} is also influenced by spatially varying characteristics that may vary more between sites than in time. Spatially varying controls on R_{eco} include plant type, soil type, microbial community, moisture limitation, radiation limitation, and GPP.

If we look at the seasonal cycle in nighttime NEE, the direct measurement of R_{eco}, at several sites (Figure 3.3a) we see that the climatological seasonality is drastically different. In a Tropical forest in Brazil (USBR1, blue), the seasonality is minimal, while at a managed cropland in Indiana (USBo1, red) the seasonal cycle is clear and well defined. At a California grassland (USVar, magenta), the seasonality is nearly reversed, with virtually no nighttime NEE in the summer when the soil is very dry. Harvard forest in Massachusetts (USHa1) shows similar seasonality to the cropland site in Indiana but with a longer growing season. Temperature, on the other hand, is characteristically similar at three of the four sites shown in Figure 3.3b, only showing a drastically different seasonality in Brazil.

In addition to differences in temperature and NEE separately, the relationship between temperature and NEE varies between sites. Notably, at USVar the climatological NEE and temperature are anti-correlated. In both Brazil and California, NEE is elevated during the cool season, suggesting that a theoretical increase in respiration rate with increasing temperature is unlikely to represent the observations at these locations. How should we characterize these sites objectively so that we may accurately represent the processes important at each site? Empirical orthogonal function analysis is well suited to characterize sites that have similar patterns of variability, and we use it to help identify variability across the network.

To characterize the variability of NEE and its control factors across the Ameriflux Network, and to identify similarities across sites in the yearly cycles of temperature and respiration, we used Empirical Orthogonal Function (EOF) analysis [*Lorenz*, 1956] to examine all sites simultaneously. The decomposition of data $A(x,t)$ can be written symbolically as

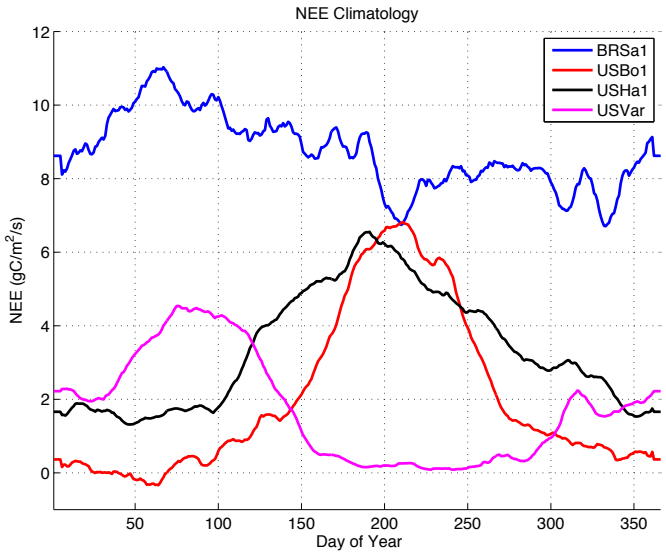

(a) Time Series of NEE

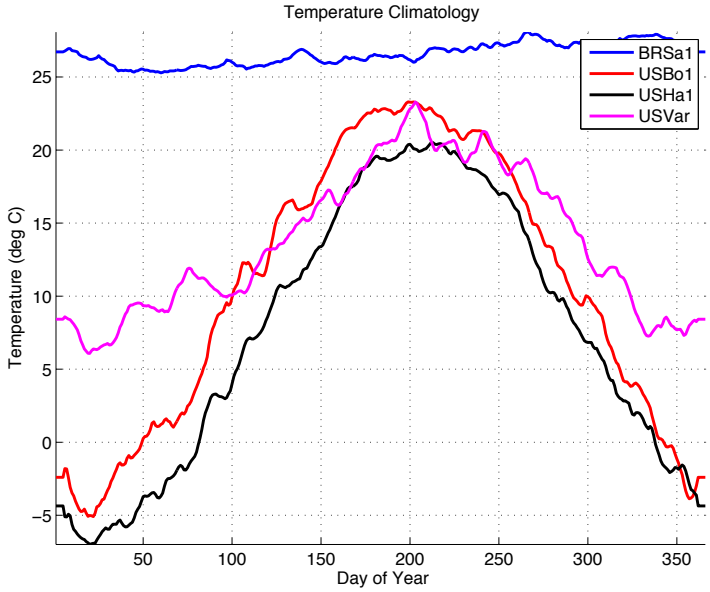

(b) Time Series of Temperature

Figure 3.3. **Time Series of NEE and T:** Time series of climatological nighttime NEE (in $gC/m^2/s$) and Temperature (in °C) at 4 sites from the Ameriflux network illustrate the large variation in seasonality across sites. Santarem (BRSa1), a tropical forest site in Brazil is shown in blue, Bondville (USBo1), a cropland site in Illinois is shown in red, Harvard forest (USHa1), a deciduous broadleaf forest is shown in black, and Varia Ranch (USVar), a California grassland, is shown in pink.

$$A(x,t) = \sum_k PC_k^A(t) \cdot EOF_k^A(x) \tag{3.7}$$

where PC_k^A and EOF_k^A are the orthogonal functions in each dimension of A. The eigenvectors $EOF_k^A(x)$, EOFs in the spatial domain, and $PC_k^A(t)$, principal components in the time domain, are ordered according to the variance captured by each component. A linear combination of the first few vectors can often explain the majority of the variance in the data. For temperature, with a strong annual fluctuation, more than 85% of variation can be represented with the first EOF/PC. The three normalizations highlight different types of variability in the data, where

$$A = A(x,t) \tag{3.8}$$

$$< A >= A(x,t) - \overline{A(x)} \tag{3.9}$$

$$\widehat{A} = \frac{A(x,t) - \overline{A(x)}}{\sigma(x)} \tag{3.10}$$

A represents a time series, $< A >$ the time series with local annual means $\overline{A(x)}$ removed, and $\widehat{A}$ the time series normalized by the local variance $\sigma(x)$. When the variable A is normalized to $\widehat{A}$ by removing the mean and dividing by the standard deviation, the EOF values correspond to the correlation between the time series at each site and the corresponding principal component (PC). Low EOF values indicate that the time series at that site differs in shape or phase from the general pattern of the rest of the network and is a good indication of an outlier. EOFs are orthogonal, ensuring that each represents separate variability, and ordered by variance, making it possible to reconstruct data products with a mode removed or to use just a few modes for analysis.

3.4.2 Variability as Illuminated by Normalization

EOF/PCs are frequently calculated on data that has been normalized in some way, usually with the mean removed ($< A >$, equation 3.8). Depending on the signal of interest, various normalizations, or no normalization at all, may yield the most illustrative results as the meaning of the spatial map changes with different initial normalizations. The most important factors controlling air temperature across the globe are relatively well understood, and thus it makes a good case for illustrating the EOF/PC method. Using nightly mean climatological air temperature measured at each tower (T) as an example, if we calculate the EOF/PCs with no normalization (T) the spatial pattern of EOF_1 primarily represents the distribution of mean temperatures (Figure 3.4a) with the highest values closest to the equator and the lowest values at high latitudes. The spatial distribution is primarily a function of

geographic location on the globe and depends on solar insolation. The time series of PC_1 looks very similar to the timeseries of PCs calculated with other normalizations except that it has a non-zero mean. The non-zero mean has consequences for the remaining modes and the variability they will be required to represent.

If we then remove the annual mean value at each site before calculating the EOF/PC we find that PC_1 of $< T >$ is almost identical to PC_1 of T, but now the spatial pattern EOF_1 represents the amplitude of the seasonal cycle in temperature (Figure 3.4b) with large amplitudes at high latitudes and in continental interiors and smaller amplitudes at low latitudes and near the coast. The degree of continentality of a site is well represented by its EOF_1 of $< T >$.

When the temperature is normalized at each site by removing the mean and dividing by the standard deviation ($\widehat{T}$, Equation 3.10) the spatial pattern shows very similar values at all sites but the most equatorward (in Brazil) (Figure 3.4c) where the seasonal cycle is different from the yearly progression of higher latitudes (c.f. Figure 3.3). The lack of a range in EOF values is a result of the difference between the tropics and higher latitudes being larger than the difference between the higher latitude sites. The EOF_1 of $\widehat{T}$ represents the seasonality, so sites with little seasonality, such as the tropical sites, will therefore be described only by higher order EOF/PCs. If our network were more globally distributed, like the FLUXNET network is, this analysis would identify clusters of sites with similar seasonality rather than isolating the tropical sites as outliers.

Climatological temperature across the network is almost entirely explained by EOF/PC 1, and the PC time series is very similar in shape for all normalizations. Much of the variance is explained by the first mode (90% and 84% for $< T >$ and $\widehat{T}$ respectively). If we look at the second modes (Figure 3.5) we see that the PC_2 of $< T >$ and $\widehat{T}$ are similar in character but have slightly different time series. Both EOFs are dominated by only a few sites. EOF_2 of $\widehat{T}$ is dominated by Brazil and the two have similar values in Arizona and in Montana (Figures 3.5b, 3.5c). The main difference in the PC_2 between these two normalizations is that the $< T >$ timeseries has a peak in late August and values above zero in February. As these characteristics of PC_2 are missing in the time series for $\widehat{T}$, we can assume that they are diminished by accounting for the standard deviation.

The PC_2 of T on the other hand has a time series similar in shape but opposite in sign from PC_1 of T (Figure 3.5a). Without removing the mean before calculating the EOF/PCs, PC_1 will have a non-zero mean (as we see in Figure 3.4a). If we think of adding the first two modes of T together (Figures 3.4a, 3.5a) we see that in Brazil the seasonality would be reduced but retain a high mean value, while in Alaska the seasonality would be amplified but the mean value would stay low. This breakdown of the variability is less intuitive, and so the mean is usually removed from time varying fields before calculating EOF/PCs.

For any site, the original time series can be recovered by summing all of the EOF/PC products (Equation 3.7). A benefit of the EOF/PC analysis is that the modes are ordered by the variance they explain. This means that often only a few modes are needed to capture almost all of the variability in a field. To reconstruct up to 93% percent of the variance in $< T >$ requires only the first two modes. For temperature, where the first mode explains

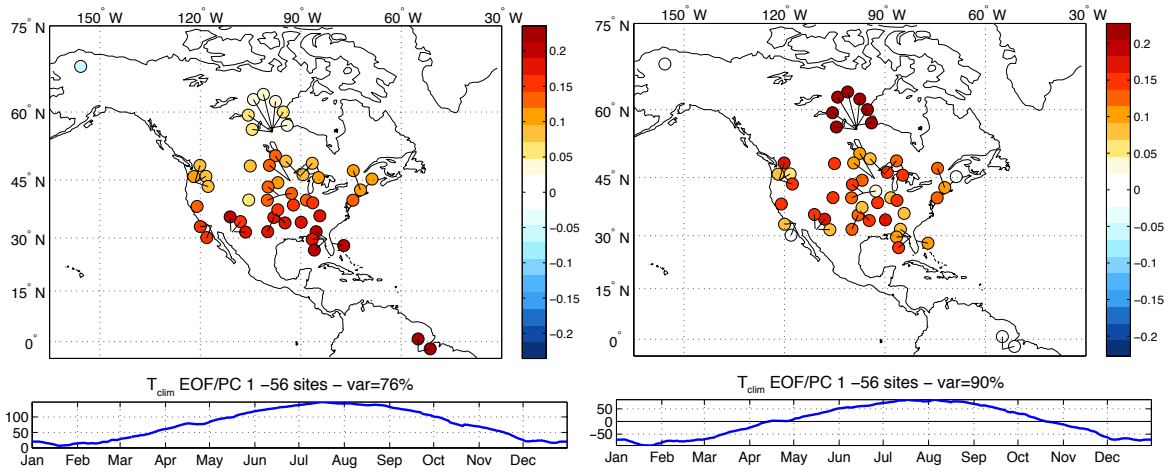

(a) EOF/PC 1 of T

(b) EOF/PC 1 of $< T >$

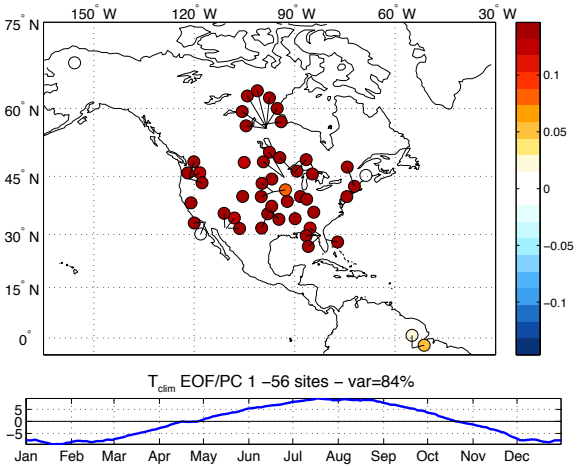

(c) EOF/PC 1 of $\widehat{T}$

Figure 3.4. **EOF/PC 1 of Temperature:** EOF/PC 1 for three different normalizations of climatological temperature: **(a)** T , **(b)** $< T >$, and **(c)** $\widehat{T}$ (Equations 3.8- 3.10). The map in each panel shows the spatial values of the EOF and the time series shows the associated PC. The variance represented by each mode is indicated in the title of the time series plot.

such a large percent of the variance, this is not as obviously useful, but for the other fields we examine several modes will contribute to the variability. This analysis of climatological temperature confirms our understanding of what controls temperature across the network and thus gives us confidence in our ability to apply the method to fields where we have less understanding of the underlying controls on variability.

3.4.3 Spatial Variability in R_{eco}

Climatological nighttime NEE varies dramatically in both mean value and seasonality across space as was illustrated in Figure 3.3a. If we repeat the EOF/PC analysis on the multiple normalizations of nighttime NEE we find that the first mode represents the typical mid-latitude seasonal cycle seen at the sites in Indiana and Massachusetts (Figure 3.3a). The PC_1 of NEE for all normalizations are similar with peak values in northern summer. The EOF_1 of NEE is largest in Brazil, where the mean value of NEE is largest even though the seasonal cycle in Brazil does not show a June-July-August (JJA) peak (c.f. Figures 3.3a, 3.6a). The EOF_1 of $< NEE >$ and $\widehat{NEE}$ (Figures 3.6b, 3.6c) have similar sites with low values indicating that these sites (i.e. Brazil, central California) do not correspond to the annual cycle represented by the principal component. If we use EOF_1 of $\widehat{NEE}$ as a mask for sites with different seasonality, EOF_1 of $< NEE >$ for the remaining sites shows the distribution of amplitude in climatological NEE as the NEE was not standardized before computing the EOFs. If the network was distributed more widely over the globe we expect that several modes would show seasonality as it varies across space, with multiple clusters of sites sharing similar seasonal behavior.

The second mode (EOF/PC 2) shows shifts to earlier or later seasons for $\widehat{NEE}$ (Figure 3.7c). The PC_2 of NEE is opposite in phase to PC_1 in the same way as for T and emphasizes the difference in seasonal cycle between the Brazilian and Californian sites from the "typical" JJA maximum in PC_1 (Figure 3.7a). The PC_2 of $< NEE >$ and $\widehat{NEE}$ are somewhat similar but opposite in sign and show a phase shift in the seasonal cycle from the typical summer max in PC_1. The effect of adding PC_1 and PC_2 (weighted at each site by EOF_1 and EOF_2) is to shift the seasonal cycle later (earlier) for positive (negative) values of EOF_2. EOF_2 of $< NEE >$ (Figure 3.7b) shows carbon fluxes peaking later in the Rocky Mountains at Niwot Ridge (USNR1, blue dot in central USA) and coming early ($\sim$June) a grassland in Kansas (USWlr, red dot in central USA). The phase shift at these sites is not evident when NEE is normalized by the standard deviation at each site (Figure 3.7c). PC_2 of $\widehat{NEE}$ shows a desert site in Arizona, a grassland in South Dakota and an agricultural site in Nebraska as having a shift towards later seasons. A cropland site in Oklahoma, and an evergreen needleaf site in Florida show strong shifts to earlier seasons. The third mode of NEE (not shown) shows an almost identical pattern to the second mode of $< NEE >$ but explains only a small percent of the variance. This indicates that without normalization, the modes will often account for these aspects of variability (i.e. distribution of mean values and seasonal amplitude) first before showing higher order variations.

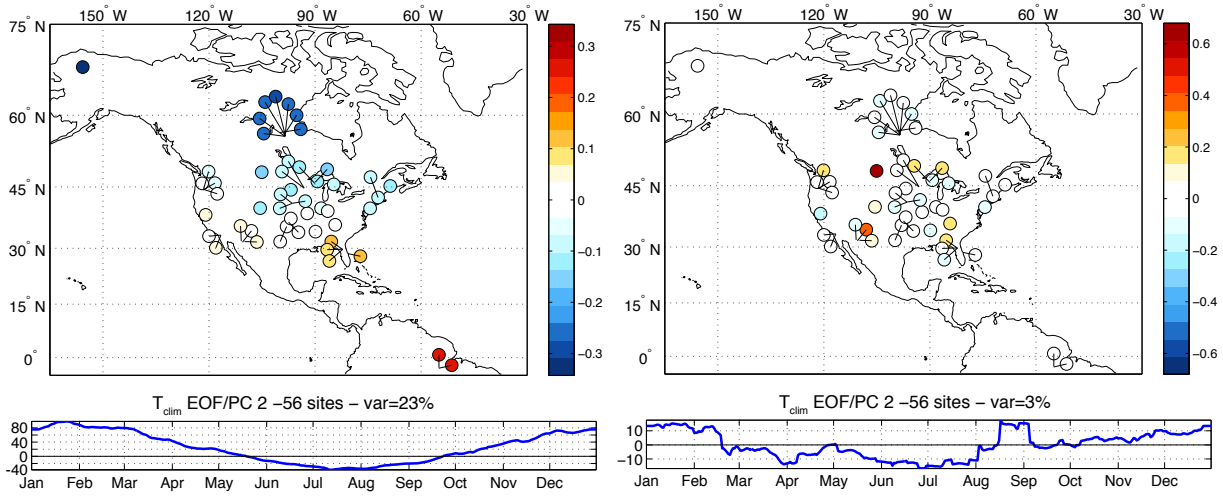

(a) EOF/PC 2 of T

(b) EOF/PC 2 of $< T >$

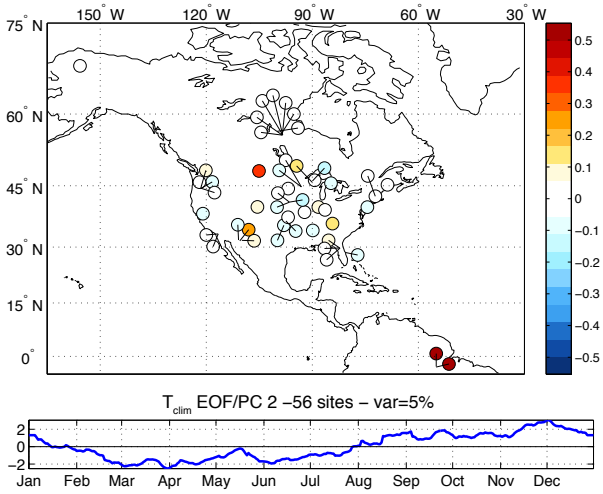

(c) EOF/PC 2 of $\widehat{T}$

Figure 3.5. **EOF/PC 2 of Temperature:** The same as Figure 3.4 for EOF/PC 2 of climatological temperature.

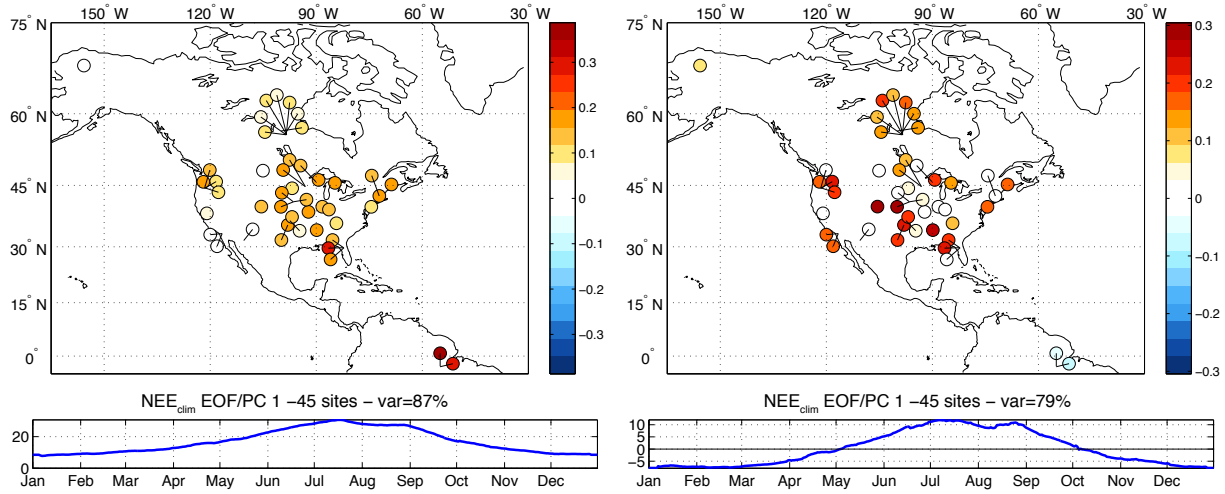

(a) EOF/PC 1 of NEE

(b) EOF/PC 1 of $< NEE >$

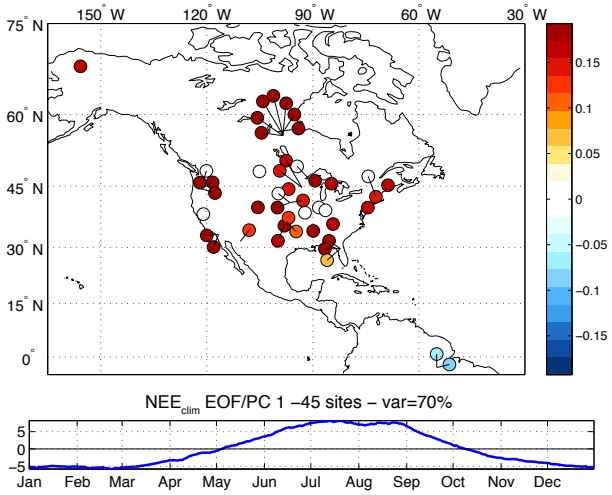

(c) EOF/PC 1 of $\widehat{NEE}$

Figure 3.6. **EOF/PC 1 of NEE:** The same as Figure 3.4 for EOF/PC 1 of climatological nighttime NEE.

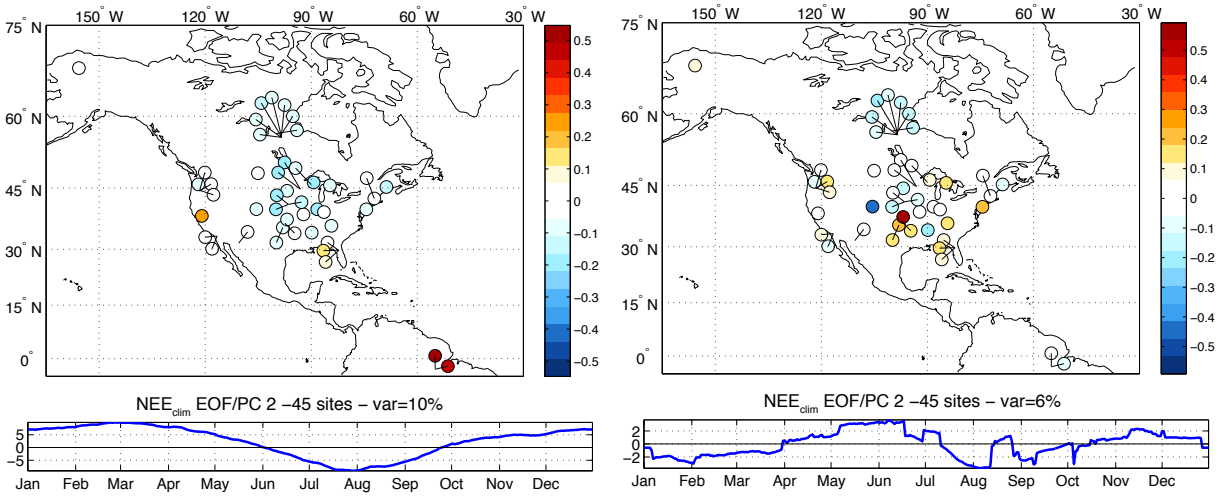

(a) EOF/PC 2 of NEE

(b) EOF/PC 2 of $< NEE >$

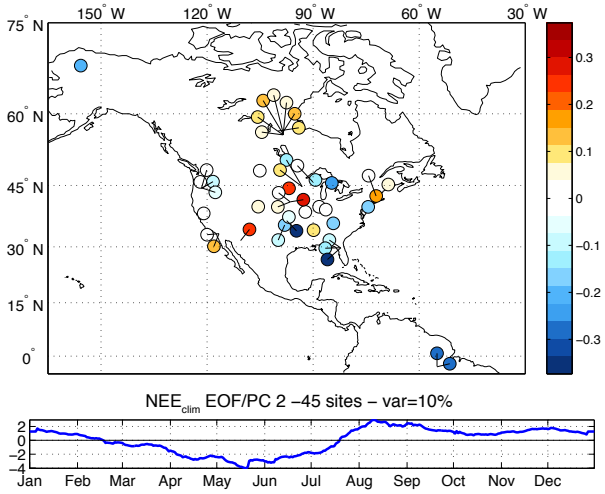

(c) EOF/PC 2 of $\widehat{NEE}$

Figure 3.7. **EOF/PC 2 of NEE:** The same as Figure 3.4 for EOF/PC 2 of climatological nighttime NEE.

3.4.4 Interannual Variability of R_{eco}

The climatological NEE is broken down into modes of variability (Figures 3.6, 3.7) but this seasonality also varies in time. Ideally, we could compute the EOF/PCs for each year at every site, but the data coverage is not uniform. Even with the gap filled data some stations have discontinuous time series. To look at the interannual variability we compute the EOF/PCs for each year separately for all available sites in any given year. Despite using a discontinuous network, the general character of the first two modes of 5-day smoothed $\widehat{NEE}$ is robust (Figure 3.8). As expected, PC_1 is similar across years. Although PC_2 also shows a consistent temporal pattern across years representing a phase shift, the spatial pattern of EOF_2 varies from year to year so that some sites show both positive and negative values depending on the year.

The interannual variability in the seasonality of NEE is shown by looking at a single site across several years. We reconstruct nighttime NEE for 2001-2006 as a weighted sum of the first two EOF/PC modes ($EOF_1(x) \cdot PC_1(x) + EOF_2(x) \cdot PC_2(x)$, Figure 3.9). The seasonal cycle in NEE is relatively uniform across 2001-2006 at Bondville (USBo1, Figure 3.9a) as expected as it is a managed cropland. Varia Ranch (USVar, Figure 3.9b) also has a consistent pattern, but one showing the opposite seasonality compared to USBo1 as expected from the climatology of temperature and NEE (Figure 3.3). We note that though the seasonal pattern is relatively constant there is interannual variability in NEE. We defer the analysis of the causes of this interannual variability in NEE until we have better understood the controls on nighttime respiration.

3.4.5 Soil Moisture Variability

The variability in the seasonality of temperature may seem too simple a field to require EOF/PC analysis to interpret, but it illustrates the thought process of interpreting other fields with less obvious patterns of variability. The negative values and near-zero of EOF_1 of $\widehat{NEE}$ at some sites shows that they have a phase opposite or uncorrelated to that of temperature (BRSa1, BrSa2, USSO3, USSO4, USVar) and indicates that temperature is not the dominant factor controlling NEE. Moisture is far more variable across space as a function of storm paths, topography and soil type and likely plays a significant role at some sites in the Ameriflux network.

The first EOF/PC of climatological soil moisture from NCEP (S_{NCEP}) shows that the mean value is similar across the entire network (Figure 3.10a). EOF_1 of $< S_{NCEP} >$ (Figure 3.10b) shows that the seasonal range is dominated by west coast stations with wet winters and very dry summers. The first two modes of $< S_{NCEP} >$ are dominated by stations in one geographical location. The corresponding modes using normalized data ($\widehat{S_{NCEP}}$) show similar PC time series but contain more information across the stations as they are not dominated by the variance at a particular location. For example, the seasonal pattern in PC_1 of $< S_{NCEP} >$ is similar to that of the first mode of $\widehat{S_{NCEP}}$ (Figure 3.10c) but when

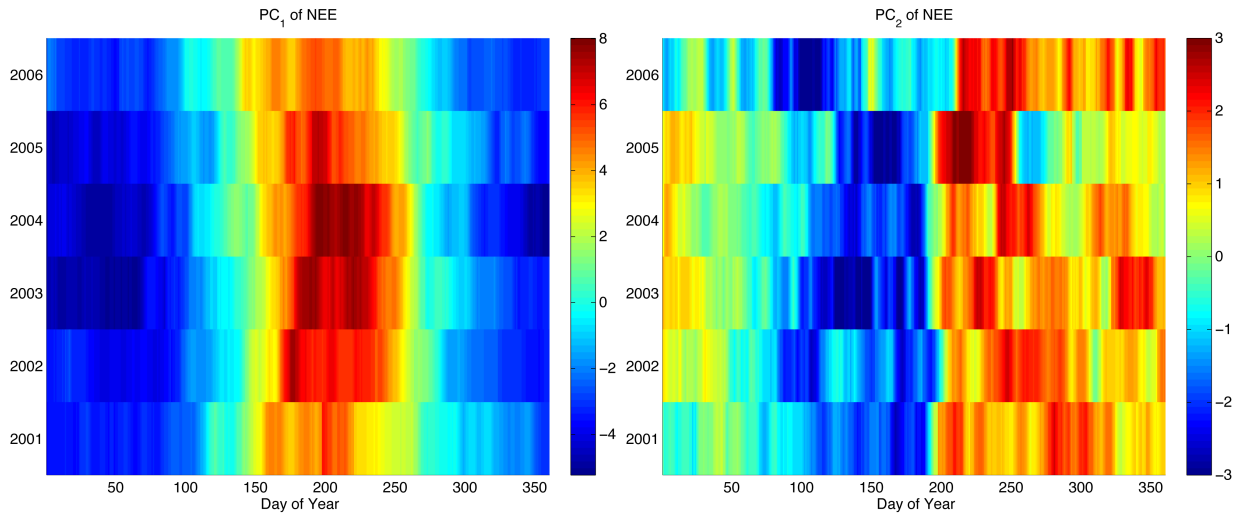

(a) PC_1 1999-2006

(b) PC_2 1999-2006

Figure 3.8. **Principal Components over Time:** The PC_1 (a) and PC_2 (b) of $\widehat{NEE}$ over the years 2001-2006. The EOF/PC for each year is calculated with data from all available sites in a given year (Table 3.2). Colors represent the value of the PC and can be thought of as the time series as viewed from above. This representation aids in comparing time series across years or sites.

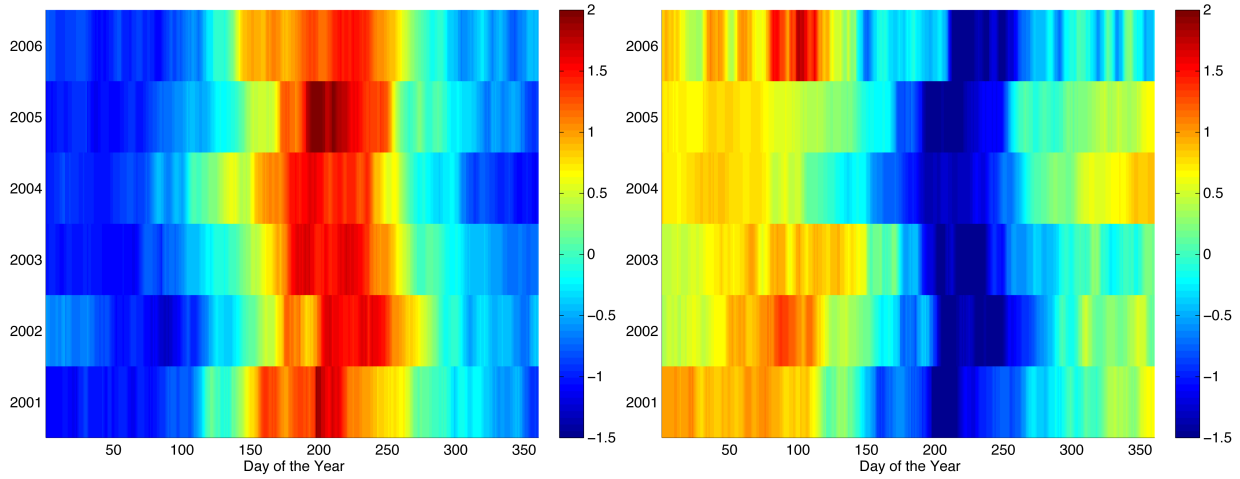

(a) Bondville(USBo1)

(b) Varia Ranch (USVar)

Figure 3.9. **Reconstructed NEE:** $\widehat{NEE}$ from years 2001-2006 reconstructed in standardized units for two sites using the first two modes from the EOF analysis for **(a)** Bondville (USBo1) and **(b)** and Varia Ranch (USVar). The plot is as in Figure 3.8, with the colors representing the value of the time series at each site.

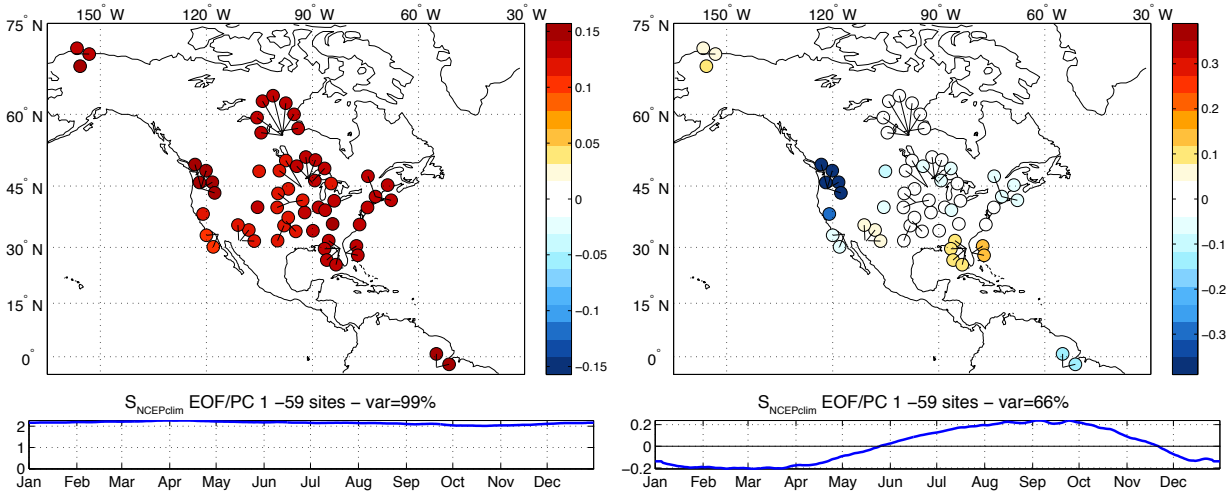

(a) EOF/PC 1 of S_{NCEP}

(b) EOF/PC 1 of $<S_{NCEP}>$

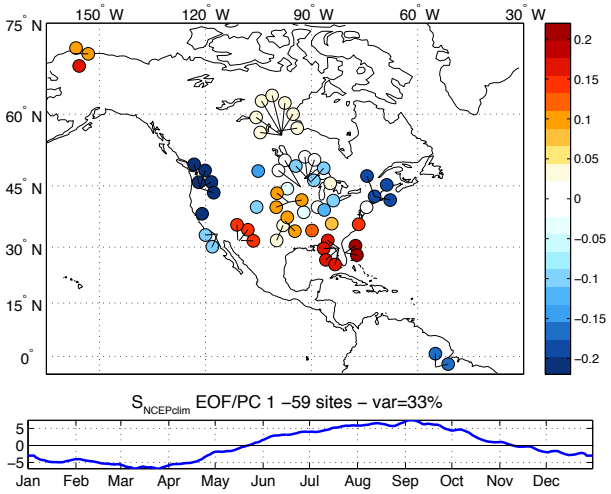

(c) EOF/PC 1 of $\widehat{S_{NCEP}}$

Figure 3.10. **EOF/PC 1 of S_{NCEP}:** The same as Figure 3.4 for EOF/PC 1 of climatological soil moisture from NCEP.

the seasonal range is accounted for the signal is no longer overwhelmed by stations in the Pacific Northwest.

EOF_1 of S_{NCEP} represents 99% of the variability and shows primarily the mean value across the network. Despite the low variance, the second mode of S_{NCEP} (Figure 3.11a) is almost identical to the first mode of $< S_{NCEP} >$ and the third model of S_{NCEP} is very similar to the second mode of $< S_{NCEP} >$. The standard deviation is the second largest mode of variability supporting the idea that when the mean and standard deviation dominate the variability, low numbered modes must represent this variability first if the field is not normalized before calculating the EOFs and PCs.

The first two modes of $\widehat{S_{NCEP}}$ (Figures 3.10c, 3.11c) explain similar amounts of variance. This suggests that the modes may be mixed (according to Norths rule, *North et al.* [1982]). Although the signal between the two modes may be mixed, taken together they still help group the stations by their moisture seasonality. Wet winter-dry summer sites have large positive EOF_2 values (Southern California), sites dominated by wet springs have large negative values of EOF_2 (central USA, Canadian sites), wet summer-dry spring sites have positive values for EOF_1 (Florida, Alaska), and wet fall-dry spring sites have positive values for both EOF_1 and EOF_2 (Arizona).

EOF/PC analysis identifies patterns of variability both in time and space. By breaking down the variability in carbon fluxes, moisture, and temperature with this method we can objectively determine the similarity between sites. The analysis presented here is limited by the spatial extent of sites in the network. If our network were more globally distributed we would expect to find multiple groupings showing variability of different character—more like in the case for moisture, where one character of seasonality does not dominate. However, even for NEE, which is dominated by one general form of seasonality in our network, the method provides an objective way of classifying sites without making prior assumptions about the factors controlling variability. In particular, the analysis can be performed on any field in space and time. In the following section we will use EOF/PC analysis to characterize the variability in the residuals of nighttime NEE after accounting for temperature and moisture.

3.5 Parameter Study: Respiration and Nighttime NEE

Respiration is one of the fundamental processes that returns biospheric carbon to the atmosphere and is hence a major control on atmospheric carbon dioxide abundance. Acceleration of respiration due to global warming is a hypothesized positive feedback on climate change [*Friedlingstein et al.*, 2003] that has been shown to exist in coupled carbon-climate models [*Friedlingstein et al.*, 2006]. Despite its importance, respiration remains poorly constrained and insufficiently represented in ecosystem models. There are no remote sensing methods or direct global field measurements of respiration, and estimations of respiratory

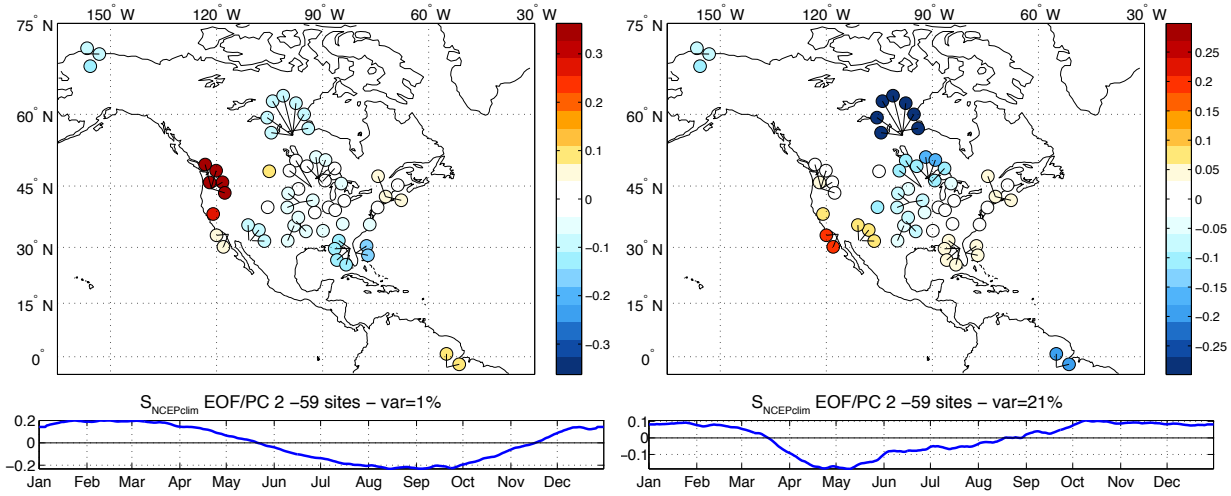

(a) EOF/PC 2 of S_{NCEP}

(b) EOF/PC 2 of $<S_{NCEP}>$

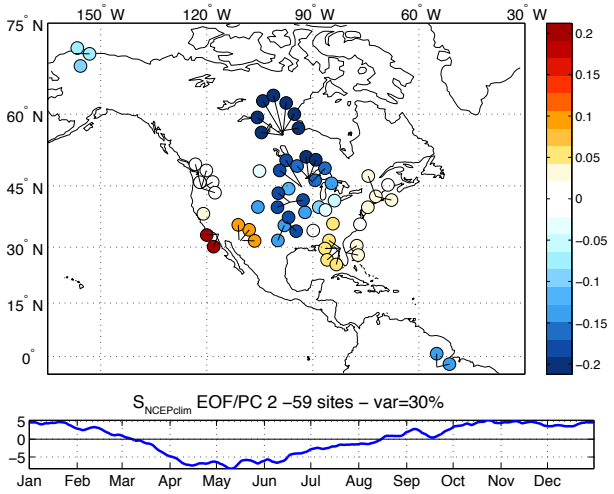

(c) EOF/PC 2 of $\widehat{S_{NCEP}}$

Figure 3.11. **EOF/PC 2 of S_{NCEP}:** The same as Figure 3.4 for EOF/PC 2 of climatological soil moisture from NCEP.

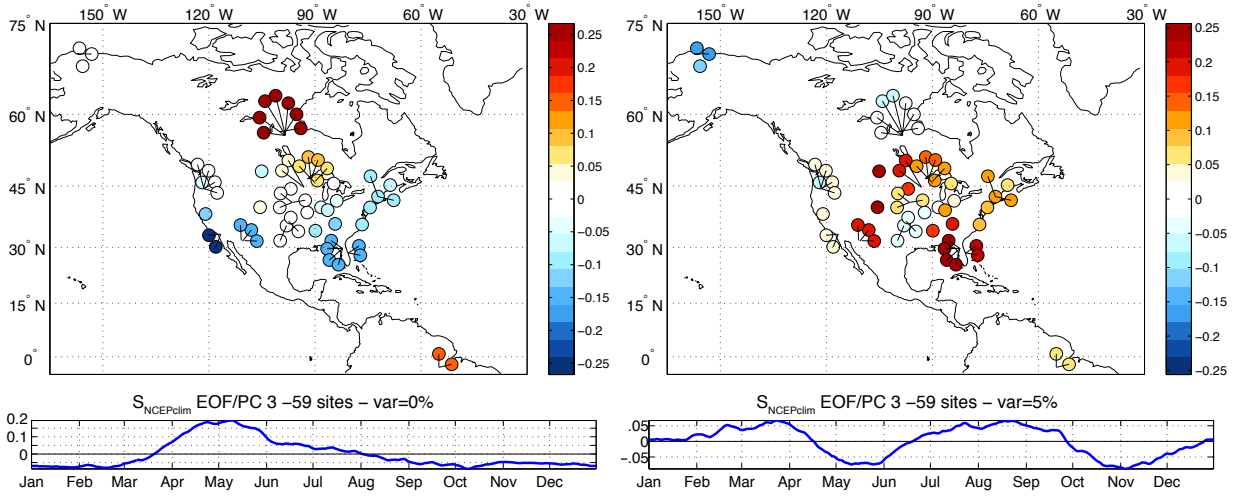

(a) EOF/PC 3 of S_NCEP (b) EOF/PC 3 of $<S_{NCEP}>$

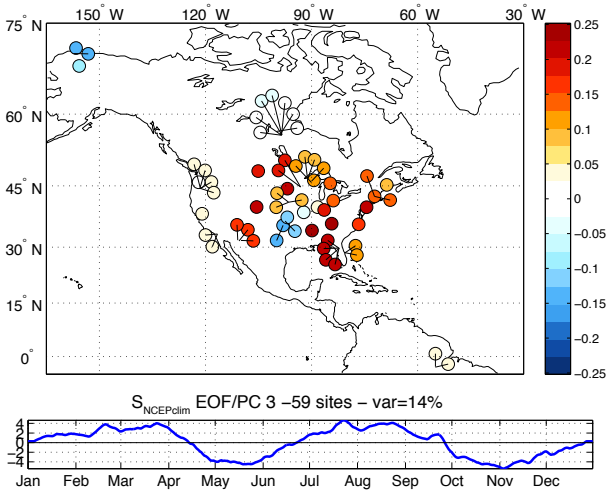

(c) EOF/PC 3 of $\widehat{S_{NCEP}}$

Figure 3.12. **EOF/PC 3 of S_{NCEP}:** The same as Figure 3.4 for EOF/PC 3 of climatological soil moisture from NCEP.

		T		NEE		S_{NCEP}		F_2	
		EOF_1	EOF_2	EOF_1	EOF_2	EOF_1	EOF_2	EOF_1	EOF_2
#	Variance (%)	92.1	3.8	77.2	9.6	33.4	30.5	37.6	18.9
1	BRSa1	0.03	0.64	-0.07	-0.28	0.16	0.15	-0.04	0.06
2	BRSa3	0.05	0.63	-0.08	-0.26	0.16	0.15	-0.13	-0.12
3	CANS1	0.14	-0.03	0.17	0.04	-0.04	0.21	-0.11	0.16
4	CANS2	0.14	0.01	0.16	0.10	-0.04	0.21	0.06	0.22
5	CANS3	0.14	0.00	0.16	0.11	-0.04	0.21	0.20	0.17
6	CANS4	0.13	0.04	0.17	0.06	-0.04	0.21	0.07	0.15
7	CANS5	0.14	0.00	0.17	0.06	-0.04	0.21	0.13	0.21
8	CANS6	0.14	0.00	0.16	0.12	-0.04	0.21	0.02	0.29
9	CANS7	0.14	0.02	0.16	0.09	-0.04	0.21	0.05	0.28
10	USARM	0.14	-0.06	0.10	-0.35	-0.09	0.17	0.01	-0.28
11	USARb	0.13	-0.10	0.15	-0.09	-0.03	0.15	0.14	-0.13
12	USARc	0.13	-0.11	0.15	-0.14	-0.03	0.15	0.15	-0.18
13	USAtq					-0.11	0.08		
14	USAud	0.14	-0.06	0.13	0.23	-0.15	-0.10	0.09	0.10
15	USBkg	0.14	-0.08	0.15	-0.18	0.02	0.11	0.19	-0.17
16	USBo1	0.14	-0.05	0.16	0.07	0.00	0.09	0.22	0.07
17	USBrw					-0.11	0.08		
18	USDix	0.13	0.01	0.14	0.03	-0.02	-0.04	0.00	0.13
19	USFPe	0.14	-0.07	0.15	-0.18	0.15	0.03	0.19	-0.15
20	USGoo	0.14	-0.07	0.16	-0.09	-0.12	-0.01	0.20	-0.13
21	USHa1	0.14	0.03	0.16	-0.05	0.19	-0.03	-0.12	0.07
22	USHa2					0.19	-0.03		
23	USHo2	0.14	0.03	0.17	0.05	0.19	0.01	0.12	-0.04
24	USIvo	0.13	0.15	0.11	0.27	-0.16	0.10	0.13	0.14
25	USKS1					-0.20	-0.03		
26	USKS2	0.13	0.01			-0.20	-0.03		
27	USLPH	0.14	0.03	0.16	-0.03	0.19	-0.03	-0.01	-0.03
28	USLos	0.14	0.07			0.10	0.16		
29	USMMS	0.14	-0.01	0.16	-0.07	0.12	0.03	0.05	-0.14
30	USMOz	0.14	-0.08	0.16	-0.14	0.04	0.15	0.13	-0.18
31	USMe1					0.22	0.02		
32	USMe2	0.13	0.03	0.16	-0.12	0.22	0.02	0.16	-0.22
33	USMe3	0.13	-0.05	0.15	-0.21	0.22	0.02	0.15	-0.21
35	USMe5	0.13	-0.02	0.15	-0.17	0.22	0.02	0.15	-0.19
35	USNC2					-0.15	-0.02		
36	USNR1	0.14	0.00	0.17	0.01	0.10	0.14	0.23	-0.01
37	USNe1	0.14	-0.05	0.16	0.09	-0.09	0.18	0.20	0.15
38	USNe2	0.14	-0.07	0.16	0.12	-0.09	0.18	0.20	0.15
39	USNe3	0.14	-0.05	0.16	0.11	-0.09	0.18	0.20	0.12
40	USOho					0.11	0.06		
41	USRo1	0.14	-0.07	0.16	0.13	0.01	0.18	0.21	0.12
42	USRo3	0.14	-0.07	0.17	0.06	0.01	0.18	0.23	0.06
43	USSO3	0.13	0.12	0.01	-0.37	0.10	-0.19	-0.18	-0.12
44	USSO4	0.13	0.10	0.05	-0.24	0.10	-0.19	-0.08	-0.18
45	USSP1	0.14	-0.01	0.14	0.02	-0.17	-0.05	0.01	-0.10
46	USSP2	0.14	-0.03	0.15	-0.05	-0.17	-0.05	-0.05	0.10
47	USSP3	0.14	0.01	0.13	-0.09	-0.17	-0.05	-0.16	-0.12
48	USSP4					-0.17	-0.05		
49	USSRM	0.14	-0.07			-0.15	-0.10		
50	USSyv	0.14	0.00	0.17	0.05	0.10	0.16	0.22	0.07
51	USUMB	0.14	0.04	0.17	0.00	-0.03	0.15	0.19	0.03
52	USVar	0.14	0.03	-0.13	-0.19	0.22	-0.03	-0.01	-0.02
53	USWBW	0.14	-0.04	0.16	-0.07	-0.08	-0.04	0.21	-0.14
54	USWCr	0.14	-0.02	0.16	-0.03	0.10	0.16	0.17	-0.08
55	USWi4					0.00	0.19		
56	USWi9					0.00	0.19		
57	USWkg	0.14	-0.06			-0.15	-0.10		
58	USWlr	0.14	-0.05	0.16	-0.14	-0.09	0.17	0.14	0.06
59	USWrc	0.14	0.01	0.16	-0.07	0.22	-0.01	0.19	-0.12

Table 3.2. **EOF Values:** Values of EOF_1 and EOF_2 for $\widehat{T}$, $\widehat{NEE}$, $\widehat{S_{NCEPclim}}$, and $\widehat{\Phi_2}$. The first row shows the variance represented by a mode. Sites are listed alphabetically and site numbers are provided for cross referencing.

fluxes are based on local empirical relationships to climate [*Valentini et al.*, 2000]. Estimates of carbon fluxes are currently being made on several scales using data acquired on platforms ranging from balloons to towers and satellites, each with its own set of constraints and problems. For this analysis we have used data from the Ameriflux tower network; site information is listed in Table 3.1.

Flux towers can measure only the net exchange of carbon between an ecosystem and the surrounding atmosphere (Equation 3.1), which is the difference between photosynthesis (uptake of carbon by plants) and respiration (the release of carbon by plants and soil), but cannot differentiate between the two. Accurate modeling of respiration is the first step towards estimating photosynthesis from flux tower data [*Falge et al.*, 2001] as the respiration signal must be removed from daytime measurements to estimate GPP (Equation 3.3). Accurate estimates of GPP can contribute to the calibration of remote sensing systems, improved assessment of global carbon exchange, and validation of global carbon cycle models.

The current method used to calculate respiration and GPP for the FLUXNET network is to use a running mean window of 30 days to calculate the temperature sensitivity of nighttime NEE as it varies over time [*Reichstein et al.*, 2005]. The temperature sensitivity for each day is then used to predict the daytime respiration and calculate GPP by Equation 3.3. Although this method may give a useful first estimate of respiration, the approach gives little insight into the physical and chemical dynamics controlling respiration as the true temperature sensitivity is not expected to vary [*Davidson and Janssens*, 2006]. Without a process-based understanding we do not have the ability to model respiration accurately in large spatial scale models or into the future. An understanding of carbon exchange is needed across varying ecosystems, latitudes, and climates to accurately assess the global carbon budget and predict the reaction of the biosphere to climate forcing.

3.5.1 Historical Background for Respiration Temperature Relationship

It has long been known that respiration is a temperature-dependent process, and attempts have been made to model the relationship using several different simple empirical equations [*Tjoelker et al.*, 2001; *Reichstein et al.*, 2005]. Vant Hoffs exponential equation [*Van't Hoff*, 1898] is often referenced, particularly in the form:

$$F = F_b \cdot Q_{10}^{\frac{T-T_b}{10}} \tag{3.11}$$

where F is the respiration fluxe at temperature T; and F_b and T_b are corresponding baseline values. Q_{10} represents the amplification factor of the respiration flux for every 10°C increase in temperature above T_b. Q_{10} is frequently assumed to be constant despite the poor fit with some data [*Davidson and Janssens*, 2006].

Atkin et al. [2000] developed a temperature-dependent Q_{10} in an attempt to describe

more of the variability in the root respiration process, but *Lloyd and Taylor* [1994] point out that attempting to fix the problem by allowing Q_{10} to be temperature-dependent ignores the underlying discrepancy; namely that respiration cannot be represented by a simple exponential dependence on temperature within a normal temperature range for ecosystems. They suggest an alternative method for fitting respiration using a modified Arrhenius-type equation [*Arrhenius*, 1889] with a temperature dependent activation energy E:

$$F = F_b \cdot e^{\frac{-E}{T - T_b}} \tag{3.12}$$

where F_b, E and T_b are parameters determined empirically. This equation had an unbiased fit to the data Lloyd and Taylor analyzed, but was found to underestimate the temperature sensitivity of soil respiration at other sites [*Janssens and Pilegaard*, 2003].

The Q_{10} derived from observations using any of the formulations described above is unique for each site, and not readily generalizable across ecosystems. Also, it assumes that respiration from leaves, trees, roots, and soil microbes have the same temperature sensitivity and that all controls of respiration can be captured because they co-vary with temperature. The overall temperature response of ecosystem respiration appears to be exponential but variable and driven by factors such as moisture and substrate availability interacting with microbial community dynamics [*Holland et al.*, 2000; *Davidson and Janssens*, 2006].

In addition to the relatively subtle problems of the exact form of exponential equation that should be used to model respiration flux as a function of temperature there is the larger question: does the exponential relationship even hold across all sites in the network? As is suggested by the range of correlation and anti-correlation in Figure 3.3, the assumption that the functional form of either Equations 3.11 or 3.12 can be used at all sites is not well justified. Figure 3.13 shows the relationship between nighttime NEE and temperature at four stations. The assumption of an exponential relationship between T and NEE appears to hold at two mid latitude stations, Harvard Forest (USHa1) and Bondville (USBo1), but does very poorly at the tropical station Santaram (BRSa1) and the California grassland, Varia Ranch (USVar). When using monthly mean nighttime values the relationship at BRSa1 looks like a negative linear relationship and nothing like an exponential (Figure 3.14). It is not surprising that in both the Tropics and in dry Mediterranean climates temperature does not appear to be the dominant control, however this complicates the ability to represent the entire network with a model using a single functional form.

Falge et al. [2002] (and later *Reichstein et al.* [2005]) describe a method to predict daytime respiration fluxes in order to calculate GPP from FLUXNET data (Equation 3.3). The method chooses a variation of Equation 3.12 to estimate a daily Q_{10} and other parameters from nighttime measurements of NEE using the best-fit regression for a running window of 30 days. The variation in the values of the daily parameters ranges considerably over the year with much of the variability remaining in the F_b term. By using daily effective parameters, this method implicitly accounts for other causes of respiration variation, such as changes in available moisture, the size of the carbon pool available for respiration, or the microbial community dynamics. Wrapping these different factors into the temperature sensitivity and allowing it to vary over time is unphysical. In addition, the form of equation 3.12 is not

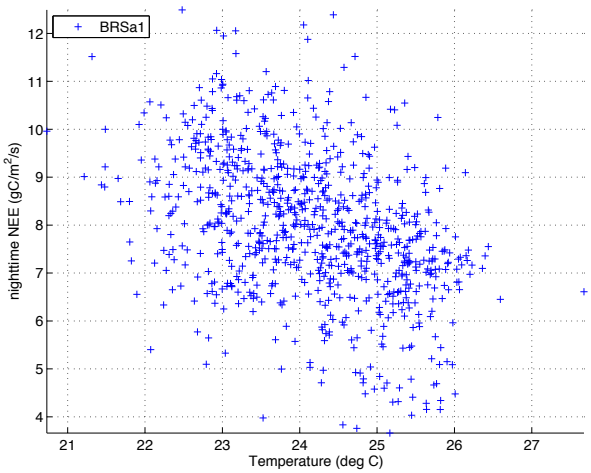

(a) T vs. NEE BRSa1

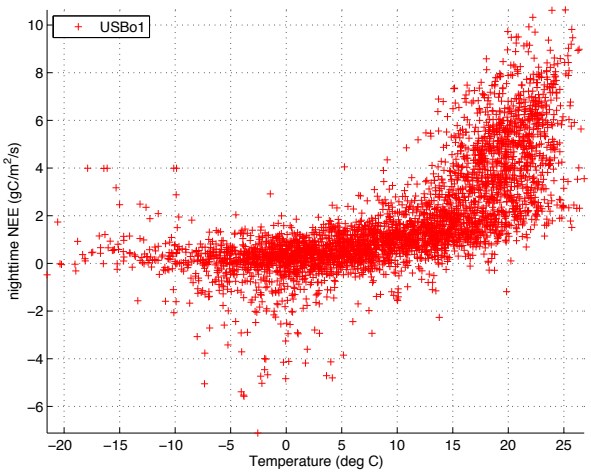

(b) T vs. NEE USBo1

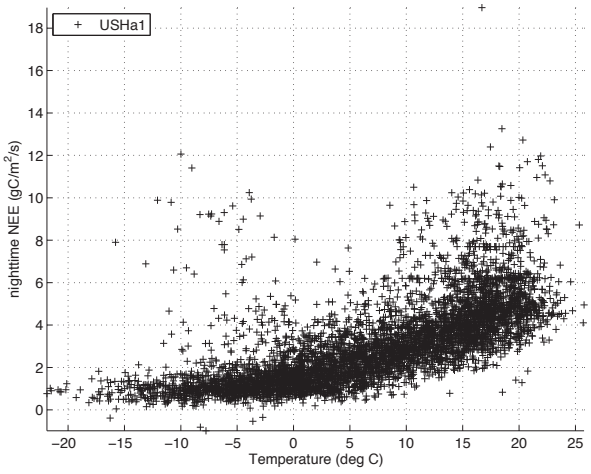

(c) T vs. NEE USHa1

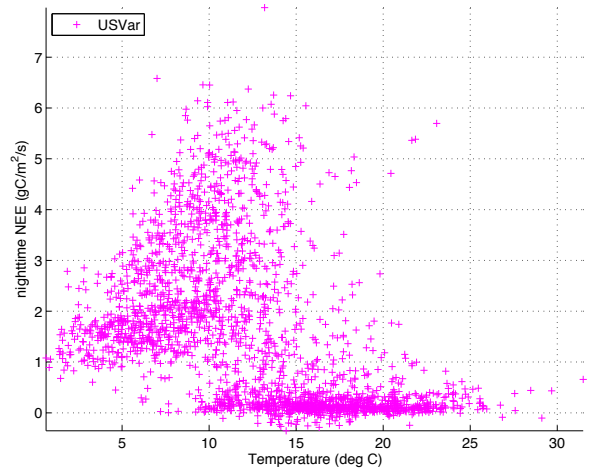

(d) T vs. NEE USVar

Figure 3.13. **T vs. NEE:** Nighttime Temperature (°C) plotted against nighttime NEE ($gC/m^2/s$) for all available data at each of four sites: **(a)** Santaram (BRSa1), **(b)** Bondville (USBo1), **(c)** Harvard forest (USHa1), and **(d)** Varia Ranch (USVar). The relationship is expected to be exponential (c.f. Equations 3.11 and 3.12).

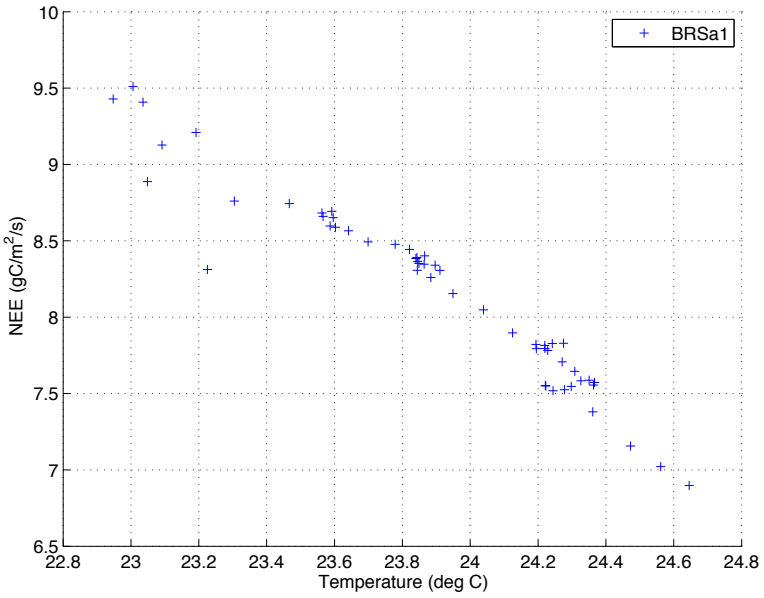

Figure 3.14. **T vs. NEE Monthly Mean:** Monthly mean nighttime Temperature (°C) plotted against monthly mean nighttime NEE ($gC/m^2/s$) for all available data at Santaram (BRSa1). The relationship is expected to be exponential (c.f. Equations 3.11 and 3.12).

necessarily the correct functional form for factors other than temperature, so that extrapolating an equation determined from nighttime values into the daytime is likely incorrect. The validity of the empirical fit when extended to higher temperatures is potentially problematic (the difference between average daytime and nighttime temperature is as large as 18°C).

Equations 3.11 and 3.12 are useful for describing the temporal evolution of respiration (or, more accurately, R_h) at a single site over the measurement time period; however, these methods are unable to assist in predicting fluxes on larger spatial scales or over time periods not captured by the measurements. As the separation of measured daytime NEE into the component fluxes of $R_a + R_h$ and P (e.g. Equation 3.3) does not follow a process-based approach, the GPP fluxes derived in this manner are likely not appropriate for use validating large-scale, process-based ecosystem models. Although it may be the best estimate that can be made with the data available from all sites, it is far from a complete representation of total R_{eco} and therefore GPP. Estimates of GPP made in this way should be viewed with an understanding of the limitations to the prediction and removal of daytime respiration.

More recent work has recognized that, particularly during winter, the direct measurements of respiration cannot be modeled well with temperature, even with time-varying parameters [*Reichstein et al.*, 2003]. The solution proposed by *Reichstein et al.* [2005] is to use summertime leaf area index as an additional factor in the empirical regression equation used to predict respiration. The physical implication of this formulation is that wintertime respiration is a function of the summertime growth. Although it is not labeled as such, the success of this approach shows that respiration is a function of the mass of substrate available for decomposition. Additionally, *Goulden et al.* [1998] find that midsummer soil respiration

rates in a boreal forest are larger than could be expected from changes in temperature. They suggest instead that the resipiration rate is controlled by the volume of thawed soil which increases in the summer as the active layer deepens. We hypothesize that changes in the mass of substrate available for decomposition influence the respiration signal measured at flux tower stations.

A model of ecosystem respiration must use a variety of predictors for variations on different time scales and take into account effects of temperature, moisture, amount of living tissue, atmospheric turbulence, and litter quantity and quality. However, not all of these variables were measured at each site or have not been reported in the Ameriflux dataset. In addition, the flux signal of any gas measured at the tower can be influenced by boundary layer turbulence, and other meteorological and abiotic processes at the tower site, so that measurements of carbon flux may not be representative of the true respiration of the local ecosystem. Soil moisture measurements can also be highly spatially variable depending on the substrate. These confounding factors make the problem of estimating R_{eco} and GPP difficult.

Webster et al. [2009] test several formulations for modeling respiration and find that including both moisture and soil carbon quantity and quality in addition to temperature improve their statistical representation of soil respiration. *Hibbard et al.* [2005] also find that local empirical relationships between temperature and respiration may not be appropriate to apply over larger spatial and temporal scales and suggest that data on the seasonality and availability of litter and root substrate are necessary to accurately predict respiration. In this chapter, we seek to evaluate the success of Equation 3.5 for modeling the seasonal variation of respiration using the nighttime NEE data from the Ameriflux network of eddy covariance towers and understand the potential use of Ameriflux data for validating ecosystem models.

3.5.2 Analysis

This analysis on the controls of respiration was approached from a modeling perspective and attempts to put the individual site analyses in the context of large-scale models. Though the network is inhomogeneous in many ways, common patterns and relationships can be identified and used as the basis for a larger scale model. We use Equation 3.5 to analyze the data across the network as a whole. We use air temperature measured at the towers and soil moisture data converted to saturation (S) as the principal control factors for nighttime respiration. Our analysis of the control factors will be sequential, first with temperature, then saturation, and finally, the residual. Respiration flux (F_0) is assumed to be a function of many variables including temperature, soil moisture, microbial community dynamics, and the mass available for decomposition (Equation 3.5). Our model will only address temperature and soil moisture directly and infer changes in the others, namely, mass of the decomposition pool.

Our analysis will focus on modeling R_{eco}. NEE measured directly by the tower consists only of respiration fluxes at night when photosynthesis is zero (c.f. Equation 3.5). We define nighttime as the half-hours with radiation reported as zero. All other times are considered

daytime. This is an imperfect measure of the radiation level at which photosynthesis begins, but should be sufficient for our analysis as we normalize by time rather than summing over the night. For our analysis of the carbon fluxes we use half-hourly measurements averaged into nighttime values. These carbon fluxes are averages over the night, not cumulative values, and are reported in units of $gC/m^2/s$.

Respiration is represented using an exponential relationship with temperature (Equation 3.11) where Q_{10} represents the amplification factor of respiration flux for every 10°C increase in temperature. Equation 3.11 is used to calculate a Q_{10} temperature function at each site of the form

$$F_0 = \Phi_1 \cdot e^{\frac{T}{10} \cdot ln(Q_{10})} \tag{3.13}$$

F_0 is the measured nightly NEE, Φ_1 is the nightly flux after removal of temperature effects, and T is the measured temperature in degrees Celsius. Equation 3.13 is identical to equation 3.11 except that the constant $T_b/10$ has been absorbed into Φ_1 and will not be calculated. We employ four approaches to calculating Equation 3.13. The first approach is commonly employed in site analysis of flux data: Q_{10} was estimated at each site as the best-fit regression parameter between the daily F_0 and T as

$$F_0^1 = \Phi_{eff} \cdot e^{\frac{T}{10} \cdot ln(Q_{10eff})} \tag{3.14}$$

We will call this parameter the effective Q_{10}, Q_{10eff}, as it attributes all variability in respiration to temperature, and does not explicitly capture the contributions of other factors to NEE variability. This Q_{10eff} could over-or underestimate the true functional effect of temperature on respiration by attributing changes in other variables correlated with temperature as a temperature dependence. Second, we estimate a companion Q_{10}, Q_{10low}, as

$$F_0^2 = \Phi_{low} \cdot e^{\frac{T_{low}}{10} \cdot ln(Q_{10low})} \tag{3.15}$$

using the monthly mean time series of both temperature and nighttime NEE to assess the realism of NEE estimation if only monthly averaged temperatures were available. Third, we calculate Q_{10clim}, as

$$F_0^3 = \Phi_{clim} \cdot e^{\frac{T_{clim}}{10} \cdot ln(Q_{10clim})} \tag{3.16}$$

from climatological estimates of temperature and NEE. The fourth approach follows that in global models (e.g. *Parton et al.* [1987]; *Potter et al.* [1993]), and specifies Q_{10}, as $Q_{10fixed}$, as

$$F_0^4 = \Phi_{fixed} \cdot e^{\frac{T}{10} \cdot ln(Q_{10fixed})} \tag{3.17}$$

where $Q_{10fixed} = 2$. The values of Q_{10eff}, Q_{10low}, and Q_{10clim} are shown in Table 3.3 and interannually varying calculations of Q_{10eff} are shown in Figure 3.16. The regression was

computed as a least squares regression in natural log space. Significance of r^2 values are reported in p-values where a p-value of 0.05 corresponds to 95% confidence that the r^2 is different than zero. P-values are determined by using a monte carlo approach to estimate the sample distribution rather than assuming the data is normally distributed. The percent of variance explained by a statistical prediction is represented by r^2.

Our model requires a representation of the saturation of soil (S). We will derive S from various measures of soil wetness. Precipitation and soil moisture are both measured at most of the Ameriflux sites. Precipitation is a highly non-linear measure and does not capture the characteristics of water available for plants and microbes as it is a measure of rate rather than storage. Soil moisture is preferable to precipitation as a predictive variable because it accounts for storage and accumulation of water in the soil, important factors for modulating respiration. Representative measurements of soil moisture are difficult to make and validate. Local measurements of soil moisture at the tower stations are problematic as the data coverage is limited—only about 60% of sites with sufficient NEE data also have soil moisture data reported. In addition, the methodology of measurements across sites and the heterogeneity of the actual soil moisture at the site is not necessarily captured.

In addition to analyzing the local soil moisture measurements available at some sites, we analyze the soil moisture product (SW) for 0-10 cm depth from NCEP-DOE Reanalysis II [*Kanamitsu et al.*, 2002]. While there are inherent uncertainties associated with any model prediction of soil moisture, due partly to uncaptured spatial inhomogeneities within the large NCEP model grid, the lack of consistent and reliable direct measurements compels us to assume the NCEP analysis products to be representative of the seasonal variations, though not of the absolute magnitudes, at each site. Because the analysis products are anchored to all available meteorological observations, the favorable comparison of NCEP reanalysis soil moisture variations with the Ameriflux precipitation data measured at each site (e.g. USVar, Figure3.15) argues that temporal variabilities in local soil moisture are well captured in the coarse-grid product. This is not surprising due to the large spatial scale ($\sim$250 km) of weather systems. Even though we are unable to quantify our confidence in the absolute magnitude of soil moisture values, we feel confident using the pattern of variation as a predictive variable.

For our analysis, we have converted both estimates of soil moisture (local and NCEP) to a non-dimensional saturation index varying between zero and one. The absolute magnitude of soil moisture is less important for calculating respiration than knowing how close the environment is to saturation. Saturation (S) at each site is derived from SW as

$$S_x = \frac{SW_x - \overline{SW_x}}{6 \cdot \sigma_{SW_x}} + 0.5 \tag{3.18}$$

where first a standardized soil moisture anomaly is calculated by removing the mean and dividing by the standard deviation at each site. Then the standardized anomaly is normalized to vary between 0 and 1 by dividing by 6 (the full range of standard deviations capturing 99.7% of the measurements) and adding 0.5 to bring the range between 0 and 1. Saturation is the parameter used in many ecosystem models to account for effects of soil moisture

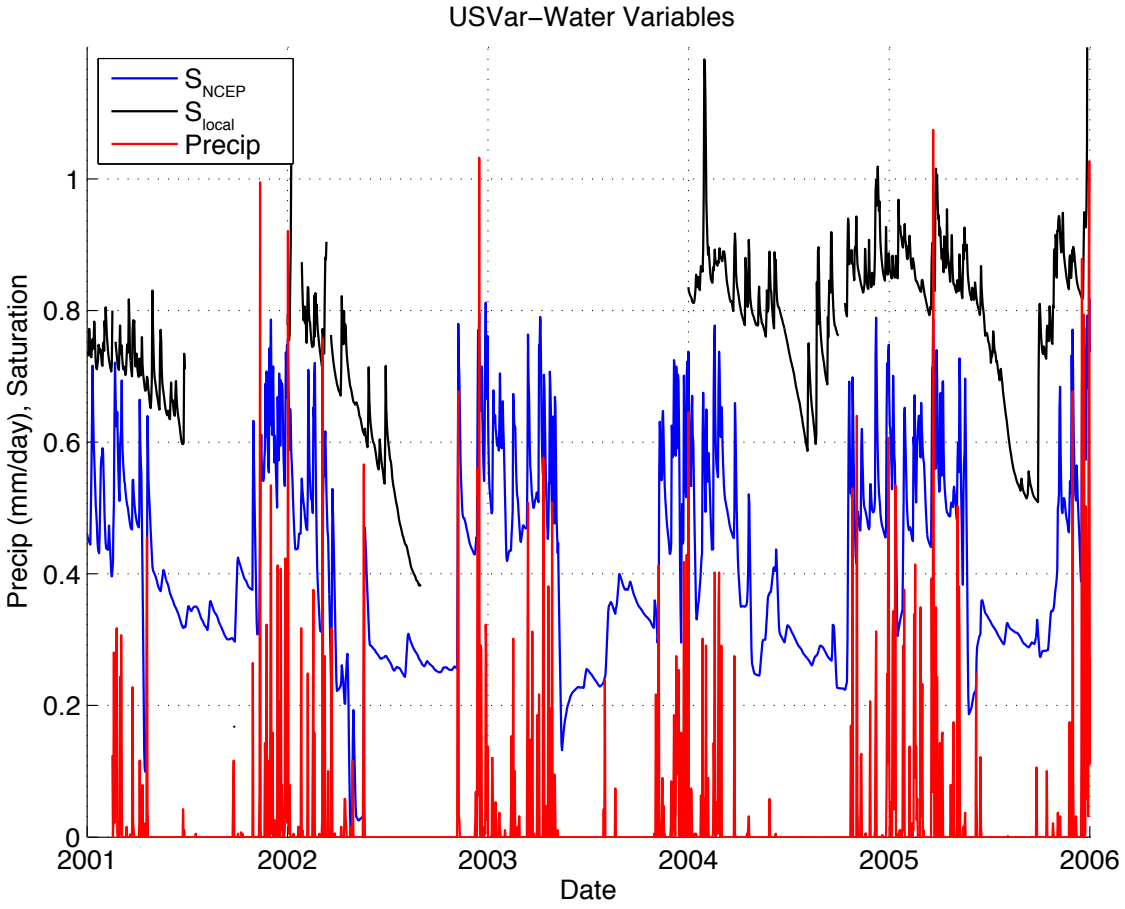

Figure 3.15. **Water Variables at Varia Ranch (USVar):** Three representations of moisture are shown for Varia Ranch (USVar). The lower red line represents the precipitation as measured at the site in mm/day. The blue line represents the soil moisture as estimated by NCEP reanalysis converted to saturation (by equation 3.18). Locally measured soil moisture converted to saturation (by equation 3.18) is shown in black. Values greater than 1 indicate a measurement outside of 3 standard deviations from the mean.

as it more closely represents the actual water availability to vegetation and the microbial population. We calculate S for both the local SW reported in the Ameriflux database as well as for the NCEP soil moisture. For the NCEP soil moisture we additionally apply a four-day running mean. A four-day window was chosen to eliminate high frequency day-to-day variations but retain synoptic scale (e.g. storm systems) variations.

To estimate the moisture dependence, the temperature function (with $Q_{10fixed} = 2$) is estimated from Equation 3.17 and removed by division

$$\Phi_{fixed} = \frac{F_0}{e^{\frac{T}{10} \cdot ln(Q_{10fixed})}} \tag{3.19}$$

This intermediate product is then regressed against saturation S to determine α and β:

$$\Phi_{fixed} = \Phi_2 \cdot (\alpha \cdot S + \beta) \tag{3.20}$$

The regression was computed by the least squares method. To elucidate other factors controlling nighttime respiration, a second residual, Φ_2, was derived in the same manner as Φ_{fixed} (Equation 3.19) as

$$\Phi_2 = \frac{\Phi_{fixed}}{(\alpha \cdot S + \beta)} \tag{3.21}$$

The Φ_2 residual is analyzed using Empirical Orthogonal Function analysis to see if it corresponds with temporal changes substrate in Section 3.5.4. This leaves our final equation in the form of equation 3.5 as

$$F_0^* = \Phi_2 \cdot (\alpha \cdot S + \beta) \cdot e^{\frac{T}{10} \cdot ln(Q_{10fixed})} \tag{3.22}$$

where F_0^* is the estimated nighttime NEE.

3.5.3 Nighttime Respiration

We calculate Q_{10eff} (Equation3.14) on interannual (Figure 3.16) and longer timescales (Table 3.3). By choosing multiple timescales over which to fit the Q_{10eff} parameter, we can see the difference in attributing all variations in respiration at these timescales to temperature. Interannual variations in Q_{10eff} at a given site are modest compared to the range in values among sites (Figure 3.16). Harvard Forest (USHa1) shows a consistent value of Q_{10eff} between 1.35 and 2.06 across years 1992 to 2006. However, many sites show values of Q_{10eff} closer to 3 and even larger. Audubon Research Ranch (USAud), a grassland in Arizona, shows values larger than 3.5 for all years available and Bondville (USBo1), a managed crop site in Illinois, shows values above 3 for all years except for 2000. These two sites are characterized by a large fraction of bare ground which may increase the temperature sensitivity by increasing the exposure of soil to the atmosphere. The Brazilian sites (BRSa1, BRSa3)

both show very low Q_{10eff}, values close to 0.5 as does Varia Ranch (USVar). These sites are characterized by a poor fit between R and NEE as seen in Figures 3.13 and 3.14.

We also calculate a single Q_{10eff} at each site using all available data across years (Table 3.3) at any given site. Deviations of Q_{10eff} from the expected value of 2 supports the idea that influences such as soil moisture, microbial community dynamics, and changes in autotrophic respiration for growth or reproductive development all influence the Q_{10eff} parameter calculated by fitting the full R_{eco} (as measured by nighttime NEE) to temperature. Some sites do not appear to have an exponential relationship between temperature and NEE (Figure 3.13) and yet the fit for Q_{10eff} is still statistically signficant. The Brazilian sites have fits which are significant and explain a large percent of the variance in NEE but do not follow the theory as intended (c.f. Figures 3.13 and 3.14).

The timescale on which data is used to calculate the Q_{10} parameter will effect the fit as processes other than temperature controlling R_{eco} will be included only in regressions over relevant time scales. We calculate a low frequency Q_{10}, Q_{10low} (Equation 3.15), from the monthly mean values of temperature and nighttime NEE (as calculated from the half hourly nighttime data). At many sites the values of Q_{10low} and Q_{10eff} are qualitatively similar (although not identical), and at others the value of Q_{10low} is unrealistically high. At a few sites (e.g. USHa2, USNe1, USRo1, USWBW, and USMe5) the values of Q_{10low} (calculated from monthly values) are systematically higher than the values of Q_{10eff} (calculated from nightly values), suggesting significant nighttime respiration during high frequency (weather) events when moisture effects may dominate. Several sites give unrealistically large values for Φ_{low} and Q_{10low} but not for Q_{10eff} or Q_{10clim}. The analysis at several sites was being strongly influenced by a few monthly mean values with very low NEE. We have removed outlier values ($NEE < 1gC/m^2/s$) before solving Equation 3.15 at the following sites: USArb, USGoo, USNR1, and USWrc.

Some values of Φ_{low} and Q_{10low} are inconsistent with $Q_{10} \sim 2$ expectation. Many of the large outlier values in Table 3.3 can be explained by a poor fit of NEE with an exponential temperature relationship. This can be seen as low amounts of variance explained by the fit (r^2) and failure of the significance test (p-value<threshold). Exceptions remain, including the Brazilian sites where low Q_{10low} values and very high Φ_{low} values give a significant fit which explains 93% of the variance at USBr1. This surprising fit is due to the lack of exponential relationship between temperature and NEE at these Tropical sites and even a negative correlation between T and NEE on monthly time scales (Figures 3.13a and 3.14). It is not clear at what value a Q_{10} parameter becomes physically unreasonable. Several sites show values in the range of 3 to 8 for Q_{10low} with significant variance explained (e.g. USAud, USHa2, and USRo1) yet may be considered very high.

We also calculate Q_{10} from climatological T and NEE, Q_{10clim} (Equation 3.16). Many estimates of Q_{10clim} are within the expected range between 1 and 3, but the values differ from those calculated on other timescales. The lack of consistency between calculations of Q_{10} made on different timescales further suggests that it is problematic to use fit values of Q_{10} to predict the process response of respiration to changes in temperature (Table 3.3). The direct fit of nighttime NEE with air temperature is sensitive both to timescale of the averaging as well as the time range over which measurements are included. This strongly indicates

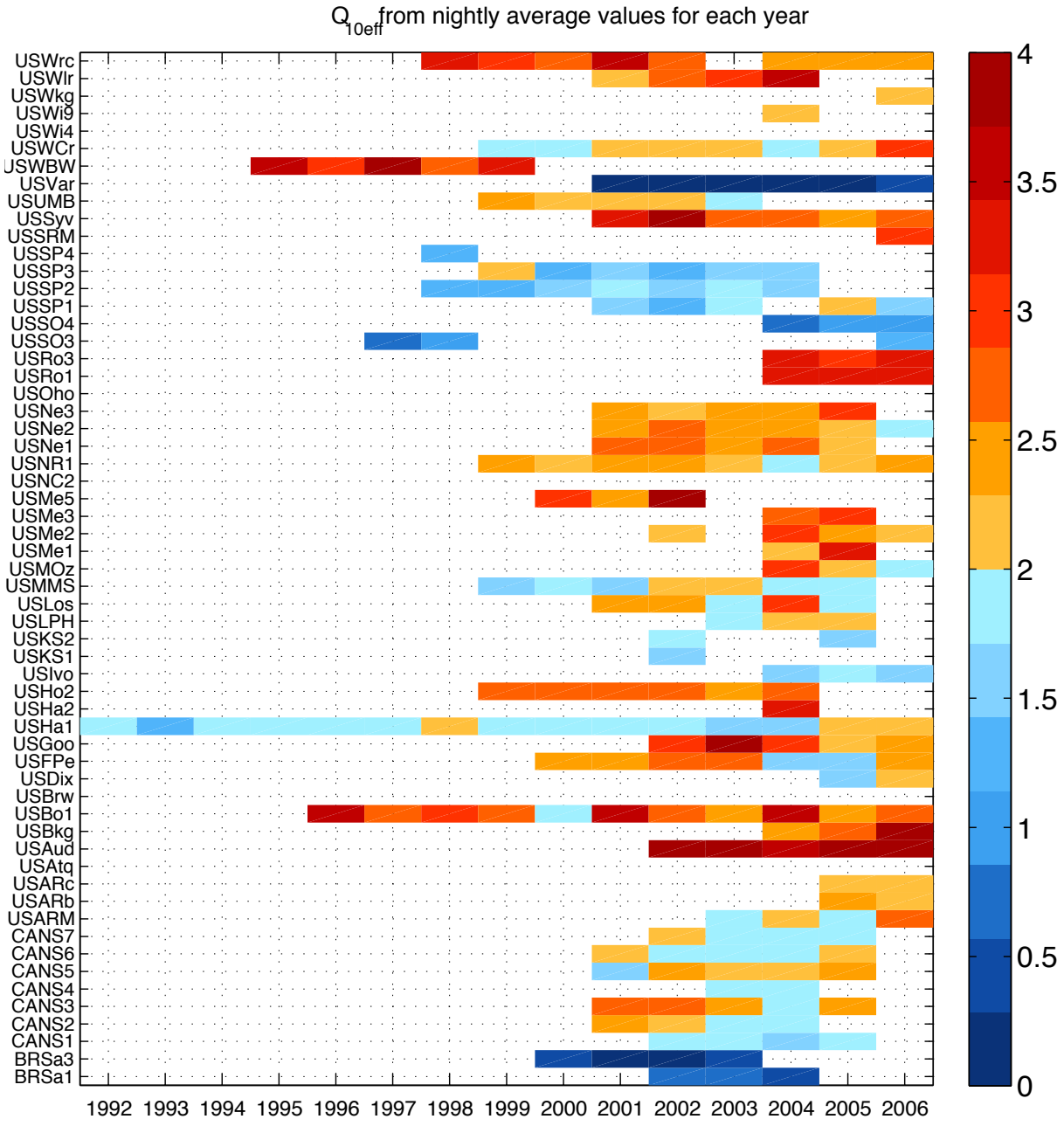

Figure 3.16. **Values of Q_{10eff}:** Q_{10eff} calculated from all data available at a given site in each year. The value of Q_{10eff} is shown in color and sites are listed alphabetically.

that processes other than temperature are distorting the expected response to temperature. Due to this blurring of processes controlling the NEE/temperature relationship we set the value of Q_{10}, as $Q_{10fixed} = 2$ for the remainder of our analysis. By setting the temperature response to a median accepted value we can focus on analyzing other processes we expect to effect R_{eco}.

After removing the effect of temperature on respiration as represented by a $Q_{10fixed} = 2$, the next variable we expect to control the rate of respiration is moisture. We compare three estimates of soil moisture, represented by saturation (S), to the residual Φ_1 as in equation 3.20 (Table 3.4). Both S_{NCEP} and S_{local} explain a significant fraction of the variance at a few sites (shown in bold), but across the network as a whole the success of saturation at predicting measured NEE fluxes is poor. $S_{NCEPclim}$ explains some of the variance at a few more sites, however the confidence in these fits being significant is lower due to the limited number of values (366 for the climatology). S_{local} explains more than 50% of the variance at USWkg (70%), USSRM (67%), and USVar (50%)—two grassland and one woody savanna site. Climatological S calculated from NCEP ($S_{NCEPclim}$) explains more than 50% of the variance at the same three sites as well as 5 more (BRSa1, BRSa3, USAud, USHo2, USWlr), two more grassland sites and two tropical evergreen forested sites. In subtropical non-forested sites we expect moisture to play a dominant role, but it appears that our skill outside of these sites is limited with the datasets we have used.

The success of using a climatological approach for S as compared to a time varying fit suggests that the noise in soil moisture variations is not well captured by the measured carbon fluxes or that the variance in soil moisture on synoptic time scales is poorly represented by NCEP. We project the carbon fluxes as they depend on soil saturation from $S_{NCEPclim}$ for all sites with p-values less than 0.15, or 85% confidence that the r^2 value is different than zero. For sites without a significant fit to saturation, we use only the temperature equation with a $Q_{10fixed} = 2$. We use this lower bar for confidence due to the limited number of samples available in the climatological fit. On visual examination, the Φ_1 residual and $S_{NCEPclim}$ seem highly correlated at the sites chosen by this method.

In a fit between temperature and respiration where Q_{10eff} is allowed to vary over time, the variations in temperature sensitivity are actually representing changes in moisture, substrate mass, and substrate quality. This representation leads to a problem of scale, particularly for moisture. The high frequency oscillations in temperature and moisture can be either correlated or anti-correlated at a single site depending on the storm track. This leads to a problem of statistical representation of one by the other. Storms can be either warm-wet (positive correlation between the anomalies) or cold-wet (negative correlation between the anomalies), allowing the sign of the correlation to change on synoptic time scales. The high-frequency variations in normalized soil moisture and temperature are shown for Harvard Forest (USHa1) and Santarem (BRSa1) in Figure 3.17. Storm scale variations show both positive and negative correlations suggesting that the representation of the effects of soil moisture through the proxy of temperature (as is done by allowing Q_{10eff} to vary over time) is unlikely to capture the true response of respiration to moisture changes.

		Effective					Low					Climatology				
#	Site ID	Φ_{eff}	Q_{10eff}	r^2	*p-val*	*n*	Φ_{low}	Q_{10low}	r^2	*p-val*	*n*	Φ_{clim}	Q_{10clim}	r^2	*p-val*	*n*
1	BRSa1	46.99	0.48	0.17	0.00	865	414	0.19	0.93	0.00	60	180.20	0.32	0.59	0.04	366
2	BRSa3	93.05	0.33	0.16	0.00	1283	76662	0.02	0.51	0.00	78	1550.65	0.14	0.83	0.00	366
3	CANS1	1.04	1.73	0.74	0.00	1152	1.54	1.74	0.97	0.00	55	1.20	1.70	0.96	0.00	366
4	CANS2	0.61	2.01	0.70	0.00	990	1.14	1.22	0.21	0.05	72	0.68	1.99	0.93	0.02	366
5	CANS3	1.02	2.35	0.74	0.00	1369	2.72	3.90	0.72	0.00	72	1.26	2.36	0.92	0.01	366
6	CANS4	0.81	1.87	0.71	0.00	499	1.78	3.98	0.65	0.00	48	0.96	1.96	0.92	0.03	366
7	CANS5	0.98	2.26	0.75	0.00	1332	1.88	2.43	0.47	0.01	65	1.23	2.09	0.96	0.00	366
8	CANS6	0.75	1.93	0.74	0.00	1411	1.44	3.19	0.97	0.00	72	0.89	1.88	0.92	0.02	366
9	CANS7	0.91	1.93	0.78	0.00	881	1.49	1.53	0.93	0.00	55	1.03	1.91	0.95	0.00	366
10	USARM	0.25	1.94	0.28	0.00	1121	0.33	2.08	0.69	0.00	48	*0.20*	*2.28*	*0.36*	*0.50*	366
11	USARb	0.49	2.11	0.35	0.03	381	0.47	3.17	0.80	0.00	20	0.43	2.43	0.34	0.06	366
12	USARc	0.71	2.14	0.56	0.02	541	0.77	2.71	0.83	0.00	22	*0.54*	*2.50*	*0.72*	*0.12*	366
13	USAtq	0.23	1.65	0.15	0.00	109	*0.48*	*1.70*	*0.08*	*0.59*	56	0.19	6.34	0.56	0.07	64
14	USAud	0.02	5.54	0.33	0.00	827	0.02	6.47	0.60	0.00	54	*0.00*	*15.07*	*0.15*	*0.74*	210
15	USBkg	0.49	3.02	0.61	0.00	875	1.08	3.84	0.91	0.00	36	*0.37*	*4.15*	*0.71*	*0.11*	345
16	USBo1	0.42	2.70	0.51	0.00	3290	0.61	3.07	0.53	0.00	125	0.25	3.80	0.93	0.02	332
17	USBrw	0.41	1.62	0.27	0.02	24	0.38	3.03	0.87	0.00	32	*0.06*	*0.76*	*0.15*	*0.22*	45
18	USDix	0.86	1.75	0.48	0.00	183	1.42	1.46	0.71	0.01	24	0.36	3.02	0.74	0.00	332
19	USFPe	0.33	2.10	0.29	0.00	1491	0.25	5.78	0.29	0.00	82	*0.18*	*3.12*	*0.68*	*0.26*	246
20	USGoo	0.48	2.69	0.53	0.00	1517	0.68	2.46	0.47	0.00	56	0.26	3.74	0.85	0.07	366
21	USHa1	1.64	1.79	0.59	0.00	5245	2.18	1.63	0.30	0.01	150	2.00	1.70	0.93	0.03	366
22	USHa2	0.74	3.39	0.89	0.00	200	0.47	7.19	0.85	0.00	36	0.68	3.53	0.95	0.00	210
23	USHo2	1.08	2.61	0.77	0.00	2186	1.46	3.64	0.95	0.00	96	1.22	2.56	0.97	0.00	366
24	USIvo	0.31	1.59	0.21	0.00	397	*0.24*	*5.04*	*0.04*	*0.69*	14	*0.15*	*1.69*	*0.40*	*0.31*	153
25	USKS1	1.24	1.70	0.71	0.00	295	0.72	2.22	0.87	0.00	42	0.82	1.99	0.88	0.00	317
26	USKS2	1.37	1.56	0.33	0.00	307	*4.83*	*0.86*	*0.01*	*0.93*	60	0.50	2.48	0.36	0.00	329
27	USLPH	1.08	1.97	0.76	0.00	883	*0.80*	*4.26*	*0.27*	*0.11*	48	1.18	1.97	0.89	0.03	366
28	USLos	0.85	2.16	0.59	0.00	1089	1.41	2.76	0.60	0.00	71	0.90	2.50	0.94	0.00	313
29	USMMS	0.92	1.90	0.68	0.00	2298	0.97	2.25	0.81	0.00	96	0.99	1.92	0.95	0.01	366
30	USMOz	0.85	2.15	0.60	0.00	909	0.40	4.63	0.59	0.02	36	0.85	2.25	0.87	0.03	366
31	USMe1	0.28	3.07	0.35	0.00	204	0.35	3.69	0.94	0.00	36	0.24	6.09	0.87	0.00	224
32	USMe2	1.03	2.35	0.50	0.00	1363	1.22	3.08	0.84	0.00	60	0.96	2.77	0.73	0.08	366
33	USMe3	0.58	2.88	0.44	0.00	598	0.50	6.64	0.86	0.00	34	*0.51*	*3.67*	*0.59*	*0.12*	340
35	USMe5	0.55	2.98	0.56	0.00	604	0.57	5.04	0.72	0.00	64	0.53	3.48	0.75	0.05	366
35	USNC2	1.14	2.07	0.54	0.00	74	0.94	3.65	0.87	0.00	24	0.28	17.28	0.47	0.00	260
36	USNR1	1.22	2.26	0.69	0.00	2204	1.57	2.49	0.56	0.00	90	1.35	2.50	0.98	0.00	366
37	USNe1	0.70	2.53	0.72	0.00	1543	0.83	4.08	0.99	0.00	72	0.76	2.54	0.91	0.01	366
38	USNe2	0.63	2.51	0.71	0.00	1473	1.25	2.78	0.34	0.00	67	0.71	2.49	0.88	0.00	366
39	USNe3	0.57	2.50	0.68	0.00	1519	0.89	2.87	0.88	0.00	67	0.60	2.55	0.85	0.02	366
40	USOho	0.86	1.85	0.48	0.02	21	0.59	5.18	0.91	0.00	21	0.10	117.37	0.81	0.00	139
41	USRo1	0.39	3.30	0.73	0.00	1004	0.57	6.32	0.95	0.00	34	0.41	3.32	0.81	0.04	366
42	USRo3	0.54	3.16	0.77	0.00	1027	0.80	4.88	0.98	0.00	36	0.59	3.06	0.89	0.02	366
43	USSO3	*0.69*	*0.88*	*0.01*	*0.57*	757	*0.97*	*0.88*	*0.02*	*0.48*	61	*0.85*	*0.92*	*0.01*	*0.87*	366
44	USSO4	*0.37*	*0.91*	*0.00*	*0.56*	793	*0.26*	*1.62*	*0.26*	*0.09*	36	*0.31*	*1.00*	*0.03*	*0.79*	362
45	USSP1	0.73	1.76	0.11	0.00	1441	0.19	4.42	0.10	0.02	72	0.57	2.08	0.73	0.04	366
46	USSP2	2.16	1.60	0.44	0.00	1950	2.89	1.37	0.56	0.00	108	2.12	1.67	0.89	0.03	366
47	USSP3	1.27	1.63	0.27	0.00	1892	0.29	4.05	0.68	0.00	96	1.46	1.60	0.75	0.00	366
48	USSP4	2.64	1.27	0.60	0.00	172	2.36	1.39	0.99	0.00	37	1.80	1.60	0.68	0.00	192
49	USSRM	*0.09*	*2.87*	*0.42*	*0.19*	242	*0.00*	*2.49E+06*	*0.82*	*0.11*	12	*0.05*	*3.40*	*0.41*	*0.42*	253
50	USSyv	0.93	2.99	0.66	0.00	1712	1.78	3.05	0.93	0.00	72	1.13	2.84	0.98	0.00	366
51	USUMB	1.20	2.19	0.84	0.00	1716	1.30	2.97	0.59	0.00	94	1.27	2.23	0.96	0.00	366
52	USVar	*6.00*	*0.19*	*0.35*	*0.28*	2093	3.82	0.50	0.41	0.00	72	*18.23*	*0.12*	*0.27*	*0.57*	366
53	USWBW	0.20	3.14	0.53	0.00	1610	0.07	8.78	0.65	0.00	88	0.14	3.81	0.92	0.00	338
54	USWCr	1.02	2.08	0.74	0.00	2347	1.51	2.07	0.91	0.00	95	1.13	2.15	0.94	0.00	366
55	USWi4	*6.72*	*0.56*	*0.18*	*0.62*	4	2.43	0.98	0.10	0.00	32	*0.00*	*10.94*	*0.30*	*0.25*	31
56	USWi9	0.77	1.76	0.11	0.00	115	*0.08*	*2.45*	*0.07*	*0.56*	6	*0.25*	*2.37*	*0.10*	*0.36*	94
57	USWkg	*0.09*	*1.69*	*0.05*	*0.83*	238	*30.73*	*0.03*	*0.04*	*0.85*	12	*0.02*	*3.59*	*0.01*	*0.95*	171
58	USWlr	0.37	2.91	0.68	0.00	1096	1.02	1.78	0.65	0.00	65	0.32	3.27	0.83	0.07	366
59	USWrc	0.85	2.73	0.44	0.00	2268	1.60	1.82	0.21	0.05	103	0.91	2.86	0.86	0.04	366

Table 3.3. **Regression Coefficients for Temperature:** Table of fit coefficients for each site from an analysis with temperature following Equations 3.14-3.16. r^2 values show the percent of variance explained, p-value indicates significance, and n represents the number of values used in each calculation with a maximum n of 5479 for Q_{10eff},180 for Q_{10low}, and 366 for Q_{10clim}. Italics indicate an r^2 that is not significantly different than zero at 90% confidence climatological calculations and 95% confidence for time varying calculations.

		$S_{NCEPclim}$					S_{NCEP}					S_{local}				
#	Site ID	α	β	r^2	*p-val*	n	α	β	r^2	*p-val*	n	α	β	r^2	*p-val*	n
1	BRSa1	-0.63	5.82	**0.72**	**0.07**	366	1.04	0.95	**0.27**	**0.00**	865	0.00	1.51	0.00	0.97	865
2	BRSa3	-1.39	6.95	**0.79**	**0.13**	366	0.98	0.54	**0.23**	**0.00**	1283	1.10	0.53	**0.23**	**0.00**	1281
3	CANS1	3.78	-8.06	0.28	0.29	366	-0.99	1.88	0.03	0.22	1152	-1.05	1.75	0.04	0.41	1028
4	CANS2	1.38	-2.12	0.04	0.27	366	-0.42	1.00	0.00	0.67	990	-0.03	0.67	0.01	0.47	591
5	CANS3	0.87	1.30	0.01	0.93	366	0.84	0.63	0.05	0.30	1369	1.47	0.52	0.10	0.27	936
6	CANS4	2.54	-4.92	**0.19**	**0.01**	366	-0.80	1.50	0.03	0.24	499	0.36	0.80	0.02	0.38	483
7	CANS5	1.59	-1.06	0.01	0.72	366	0.52	0.80	0.01	0.40	1332	1.38	0.56	**0.09**	**0.05**	967
8	CANS6	2.72	-5.65	0.15	0.19	366	-0.36	1.13	0.01	0.59	1411	-0.30	1.08	0.00	0.73	1051
9	CANS7	2.29	-3.89	0.13	0.20	366	-0.22	1.19	0.00	0.57	881	0.05	0.99	0.00	0.94	656
10	USARM	-1.55	6.43	0.15	0.42	366	0.09	0.30	0.00	0.72	1121	0.23	0.24	0.02	0.44	787
11	USARb	-4.61	18.29	**0.17**	**0.14**	366	0.78	0.25	**0.05**	**0.05**	381	0.76	0.33	0.06	0.16	378
12	USARc	-4.06	16.93	0.19	0.16	366	0.80	0.44	0.06	0.11	541	1.17	0.32	**0.19**	**0.01**	539
13	USAtq	-11.91	35.72	0.22	0.19	366	-1.45	1.47	0.08	0.38	109	0.00	0.47	0.00	0.98	109
14	USAud	-1.49	5.68	**0.58**	**0.09**	366	0.43	-0.09	**0.17**	**0.02**	827	0.08	0.13	0.01	0.52	802
15	USBkg	0.63	0.38	0.00	0.94	366	0.75	0.40	0.04	0.33	875	0.92	0.40	**0.16**	**0.05**	868
16	USBo1	-2.08	8.85	0.02	0.80	366	-0.10	0.86	0.00	0.56	3288	-0.95	1.29	0.01	0.37	2696
17	USBrw	0.64	-1.97	0.03	0.29	366	0.83	0.75	0.01	0.63	24	0.00	1.09	0.00	0.99	24
18	USDix	-3.92	14.64	0.06	0.42	366	0.87	0.42	0.01	0.62	182	0.00	1.01	0.00	0.96	182
19	USFPe	1.63	-5.39	0.10	0.65	366	0.40	0.36	0.00	0.93	1491	-0.71	1.16	0.05	0.06	918
20	USGoo	0.96	-0.58	0.00	0.93	366	-0.12	0.97	0.01	0.45	1515	0.41	0.70	0.03	0.33	1381
21	USHa1	-1.07	8.88	0.13	0.59	366	-0.36	1.95	0.00	0.35	5242	0.00	1.73	0.00	0.94	5242
22	USHa2	11.77	-33.93	0.45	0.36	366	-0.58	1.75	**0.02**	**0.02**	200	0.00	1.38	0.00	0.00	200
23	USHo2	8.92	-23.53	**0.58**	**0.08**	366	-1.06	2.14	0.09	0.29	2186	0.00	1.41	0.00	0.99	2186
24	USIvo	-6.59	16.99	0.21	0.20	366	-1.51	1.72	0.04	0.05	397	0.00	0.78	0.00	0.96	397
25	USKS1	0.35	1.13	0.01	0.76	366	-0.05	0.91	0.00	0.74	295	-0.09	0.92	0.01	0.65	250
26	USKS2	2.40	-5.36	0.16	0.30	366	0.46	0.72	0.04	0.18	307	0.40	0.76	0.05	0.08	281
27	USLPH	2.50	-4.04	**0.06**	**0.10**	366	-0.41	1.44	0.03	0.10	883	0.00	1.15	0.00	0.97	883
28	USLos	1.71	-2.55	0.01	0.85	366	-0.52	1.40	0.03	0.12	1089	0.00	1.04	0.00	0.97	1089
29	USMMS	0.66	0.88	0.01	0.88	366	0.09	0.88	0.00	0.59	2298	0.26	0.76	0.01	0.20	723
30	USMOz	-3.38	14.53	**0.22**	**0.08**	366	0.09	1.00	0.00	0.73	907	0.21	0.94	0.00	0.62	905
31	USMe1	-0.34	1.62	0.25	0.21	366	-0.03	0.39	0.00	0.91	204	0.25	0.23	0.02	0.61	178
32	USMe2	2.04	-2.14	0.09	0.70	366	-0.19	1.45	0.02	0.78	1361	-0.40	1.54	0.04	0.78	1363
33	USMe3	1.66	-2.41	0.08	0.77	366	-0.07	1.01	0.02	0.82	598	0.08	0.93	0.02	0.78	595
35	USMe5	1.33	-1.52	0.09	0.79	366	-0.09	0.88	0.00	0.85	604	-0.27	0.96	0.01	0.86	604
35	USNC2	2.92	-8.02	0.03	0.18	366	0.29	1.14	0.00	0.99	74	-0.40	1.40	0.01	0.88	63
36	USNR1	0.96	1.55	0.01	0.88	366	0.56	1.04	**0.03**	**0.04**	2202	0.53	1.07	0.03	0.19	1185
37	USNe1	-3.14	14.46	0.17	0.60	366	0.44	0.75	0.01	0.36	1543	-0.39	1.25	0.00	0.68	1536
38	USNe2	-2.09	10.44	0.14	0.65	366	0.35	0.72	0.01	0.22	1473	-0.71	1.32	0.04	0.07	1460
39	USNe3	-2.65	11.96	0.20	0.54	366	0.25	0.69	0.02	0.21	1519	-0.92	1.31	0.08	0.06	1513
40	USOho	2.45	-7.58	0.09	0.31	366	0.65	0.53	0.05	0.30	21	-0.42	1.08	0.02	0.44	20
41	USRo1	-0.34	3.66	0.02	0.86	366	-0.08	0.84	0.00	0.99	1002	0.00	0.79	0.00	0.99	1002
42	USRo3	0.04	3.07	0.01	0.87	366	0.15	0.88	0.00	0.92	1025	0.00	0.98	0.00	0.99	1025
43	USSO3	-0.09	1.87	0.08	0.78	366	0.04	0.37	0.00	0.88	755	0.59	-0.03	**0.21**	**0.00**	363
44	USSO4	0.29	-0.55	0.02	0.81	366	0.18	0.13	0.03	0.18	793	0.31	0.09	**0.10**	**0.01**	782
45	USSP1	0.93	-0.93	0.02	0.53	366	0.09	0.69	0.01	0.36	1439	0.00	0.74	0.00	0.96	1439
46	USSP2	3.78	-7.11	**0.39**	**0.14**	366	-0.07	1.65	0.00	0.74	1950	0.00	1.61	0.00	0.94	1950
47	USSP3	2.49	-4.82	0.32	0.18	366	-0.10	1.05	0.00	0.72	1892	0.00	0.99	0.00	0.97	1892
48	USSP4	5.90	-16.60	0.24	0.40	366	0.72	0.92	0.06	0.54	172	0.00	1.37	0.00	0.99	172
49	USSRM	-1.67	6.78	**0.60**	**0.01**	366	0.59	-0.13	0.32	0.11	240	0.99	-0.24	**0.67**	**0.00**	242
50	USSyv	5.29	-12.25	0.15	0.61	366	-1.49	2.45	**0.07**	**0.01**	1710	-1.51	2.27	0.04	0.22	1637
51	USUMB	1.19	0.67	0.00	0.99	366	-0.51	1.70	0.03	0.12	1716	0.00	1.35	0.00	0.95	1716
52	USVar	-2.74	12.69	**0.83**	**0.08**	366	2.70	-0.59	**0.38**	**0.04**	2091	3.31	-0.85	**0.50**	**0.05**	2046
53	USWBW	0.66	-0.75	0.00	0.80	366	0.18	0.39	0.00	0.85	1610	0.00	0.50	0.00	0.97	1610
54	USWCr	1.83	-2.01	0.04	0.61	366	-0.27	1.31	0.01	0.17	2347	-0.04	1.14	0.00	0.76	2265
55	USWi4	-0.03	0.14	0.01	0.72	366	0.04	0.60	0.00	0.96	4	-5.46	2.88	0.27	0.63	4
56	USWi9	-1.59	4.99	0.02	0.42	366	-1.20	1.62	**0.05**	**0.03**	115	0.00	0.78	0.00	1.00	115
57	USWkg	-1.26	4.91	**0.66**	**0.04**	366	0.50	-0.19	**0.35**	**0.02**	236	0.56	-0.18	**0.70**	**0.00**	238
58	USWlr	-7.33	27.99	**0.74**	**0.00**	366	0.46	0.41	0.02	0.13	1096	-0.48	0.95	0.07	0.47	1092
59	USWrc	2.42	-3.25	0.29	0.60	366	-0.74	1.81	0.04	0.09	2268	-0.45	1.55	0.01	0.26	1888

Table 3.4. **Regression Coefficients for Saturation:** Table of fit coefficients for each site for a regression between Φ_1 and saturation from Equation 3.20 using climatological soil moisture derived from NCEP ($S_{NCEPclim}$), time-varying NCEP derived soil moisture (S_{NCEP}), and locally measured soil moisture (S_{local}). r^2 values show the percent of variance explained, p-value indicates significance, and n represents the number of values used in each calculation with a maximum n 366 for $S_{NCEPclim}$, and 5479 for S_{NCEP} and S_{local}. Bold values indicate an r^2 that is significantly different than zero at 85% confidence climatological calculations and 95% confidence for time varying calculations.

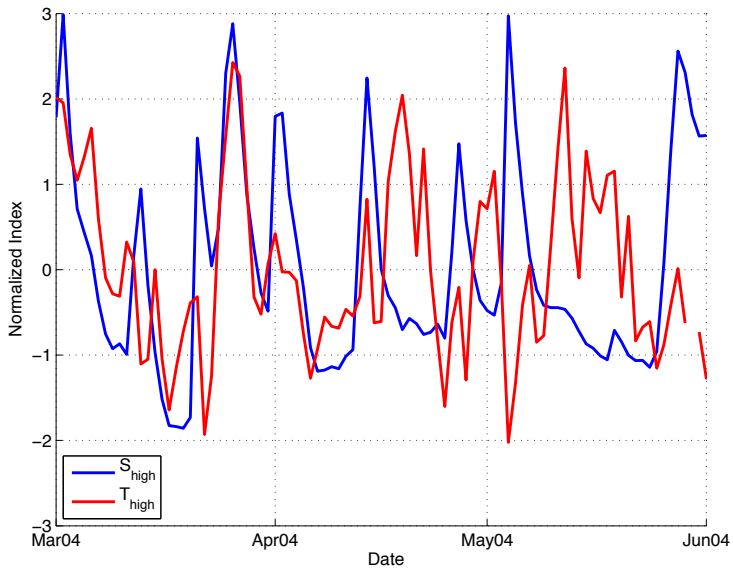

(a) Harvard Forest (USHa1)

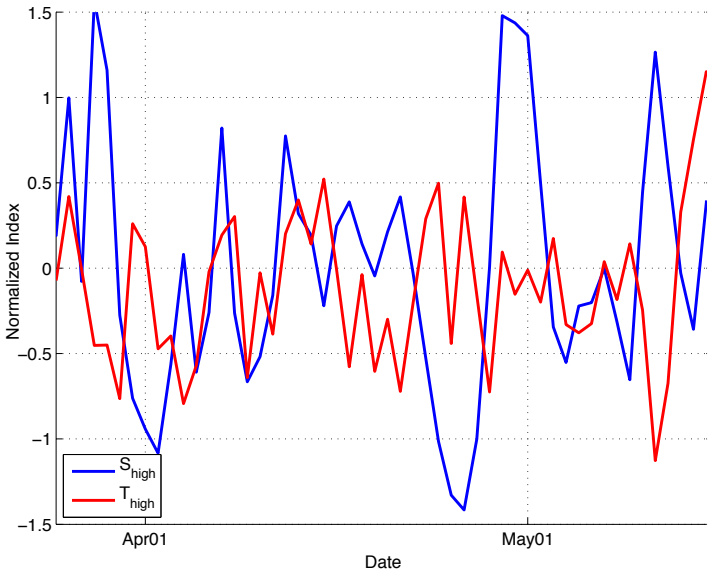

(b) Santarem (BRSa1)

Figure 3.17. **High Frequency Temperature and Saturation:** High frequency standardized temperature (red) and soil moisture (blue) for **(a)** Harvard Forest (USHa1) and **(b)** Santarem (BRSa1). High frequency variations are calculated as anomalies from climatology by removing the climatological T or S from the full time-varying signal.

3.5.4 Model Residuals: Time Varying Substrate?

As we have captured the effects of temperature and soil moisture, we can now analyze the Φ_2 residual (Equation 3.21) with respect to other processes that remain un-captured by our analysis. We expect that the remaining processes controlling nighttime NEE will depend on the mass of leaf and fine root litter available for decomposition. We calculate the EOF/PCs of the $\widehat{\Phi_2}$ residual using $S_{NCEPclim}$ as our saturation dataset (Table 3.2). The PC_1 time series (representing 37% of the variance) has a seasonal cycle with a peak in mid August (Figure 3.18a). The EOF_1 of $\widehat{\Phi_2}$ shows positive values in the central US, as well as in Oregon, Alaska, Arizona, and one site each in the Northeast USA and Canada. Southern California grasslands show a negative EOF_1 value as do the stations in Florida and USHa1. PC_2 of $\widehat{\Phi_2}$ (Figure 3.18b) has a strong peak in late January and a low peak in mid August with large EOF_2 values at the Canadian sites. This suggests that these sites experience a pulse of respiratory fluxes during winter. The negative EOF_2 amplitudes in the Pacific Northwest, Southeast USA and Southern California suggest high respiratory fluxes in the late spring, possibly from respiratory fluxes associated with construction of new plant material. EOFs 3 and 4 show shorter time-scale pulses of respiration.

High EOF_1 values indicate that seasonal respiration fluxes with a peak in late summer-early fall are unaccounted for. We suggest that the remaining residual may be due to seasonal variations in mass of material available for decomposition. Mass of the substrate also changes throughout the year due to changes in above ground leaf litter, below ground root mass, and variations in autotrophic respiration. The PC_1 of $\widehat{\Phi_2}$ can therefore be though of as a mass function at sites where EOF_1 is positive. We note that *Reichstein et al.* [2003] find a time varying signal with similar seasonality in F_b from Equation 3.12 when they allow the parameters to vary over time although they do not identify it as a seasonal variation in substrate mass.

Whatever processes control the remaining variance in nighttime NEE vary over time and space. The annual and interannual fluxes in substrate available for decomposition are not considered in the operational approach estimating fluxes of respiration (c.f. *Falge et al.* [2002]) but the effects are wrapped into the Q_{10eff} term. In a process-based approach, the mass should be considered independently. In addition to mass there are likely other processes controlling respiration fluxes including changes in substrate quality and microbial community dynamics over time. Accurate modeling of respiration, and thus GPP, will likely require observations of the temporal variation of these additional factors.

3.6 Conclusions

Modeling ecosystem respiration is no easy task. Several processes with spatial and temporal variability control the rate of soil respiration and direct measurements for the validation of models are unavailable at large-scales. The partitioning of carbon flux measurements from eddy covariance flux towers into photosynthesis and ecosystem respiration is further

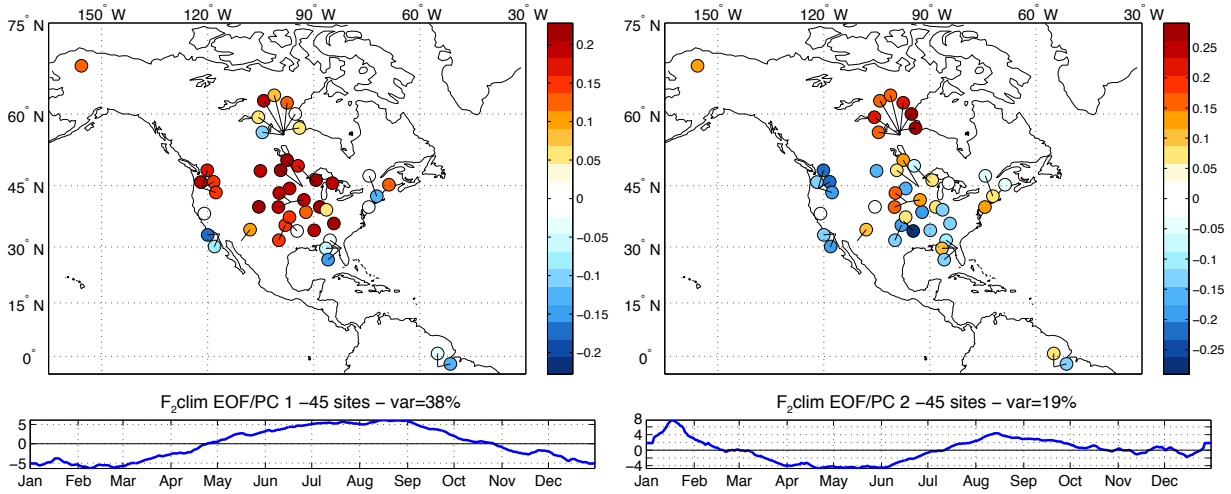

(a) EOF/PC 1 of $\widehat{\Phi_2}$

(b) EOF/PC 2 of $\widehat{\Phi_2}$

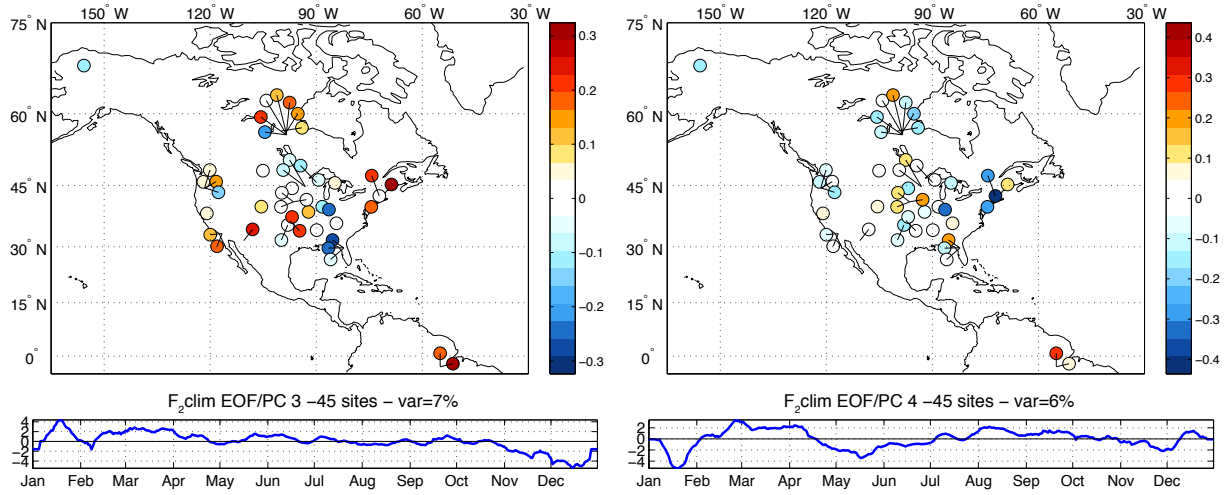

(c) EOF/PC 3 of $\widehat{\Phi_2}$

(d) EOF/PC 4 of $\widehat{\Phi_2}$

Figure 3.18. **EOF/PCs of $\widehat{\Phi_2}$:** EOF/PCs 1-4 **(a-d)** of $\widehat{\Phi_2}$. The map in each panel shows the spatial values of the EOF and the time series shows the associated PC. The variance represented by each mode is indicated in the title of the time series plot.

complicated by the fact that the measured signal includes respiration fluxes from the entire ecosystem. Despite the difficulty of the problem, respiration must be estimated both in ecosystem models to obtain a net carbon flux from the surface, and from measurements of net carbon flux at eddy covariance flux towers to estimate photosynthetic fluxes. Models of the global carbon cycle represent these fluxes with process-based empirical formulations. Parameters for these formulations are usually found from small-scale observational data. With its extensive spatial coverage the Ameriflux carbon flux data has the potential for validating parameters to be used in global scale ecosystem models.

We expect the temperature sensitivity of biogeochemical processes to be relatively constant. Allowing the temperature sensitivity (as represented by Q_{10}) of the respiration-temperature relationship to change over time implicitly assigns variability from other processes controlling the rate of respiration to a temperature dependence. Our analysis shows that the fit parameter Q_{10eff} depends on both the timescale of variation as well as the time range over which we calculate the parameter. This strongly suggests that Q_{10eff} is capturing the effects of processes other than temperature. These other processes implicitly captured by Q_{10eff} do not necessarily scale with temperature when daytime respiration fluxes are extrapolated from nighttime parameters.

By fixing the temperature sensitivity we analyzed the effects of other variables on the rate of respiratory fluxes. Moisture, as measured by a saturation index, is able to explain a significant percent of the variability at a few sites, but overall across the network the skill of moisture for explaining variability in respiration is poor. Sites showing a strong relationship with moisture are subtropical grasslands and shrublands—ecosystems that are water limited.

Ecosystem respiration is modulated not only by temperature and moisture, but also by the availability of substrate and fluctuations in mass available for decomposition should follow a seasonal pattern. The Φ_2 residuals of our respiration flux after accounting for temperature and moisture show that substrate seasonality is an important factor for respiration. We hypothesize that the remaining signal represents seasonal variations in substrate mass, probably from changes in fine root decomposition as well as leaf litter.

The Ameriflux data network is potentially useful for gaining insight into the range of relationships possible for respiration and photosynthesis but much work is needed to develop a more successful representation of respiration before the published estimates of GPP can be trusted for use in the validation of large-scale models. Temporal information on soil moisture conditions, soil organic matter mass, and leaf litter mass at site locations will be necessary in order to estimate respiration, and thus GPP, defensibly on a large-scale. Although much can be learned from the global Ameriflux network, the GPP product should be viewed cautiously, especially when used to validate large-scale carbon-cycle climate models.

Chapter 4

Remote Effects of Mid Latitude Afforestation

4.1 Abstract

We find that large scale increases in mid latitude forests have the ability to modify northern hemisphere temperatures and global circulation patterns resulting in effects on both the local and global climate and carbon cycle. A northward shift of the intertropical convergence zone over Africa associated with afforestation in mid latitudes suggests that extratropical vegetation may be partly responsible for the maintenance of precipitation over the Sahara observed in proxy records of vegetation from the Mid Holocene. The ability of vegetation to effect remote circulation has implications for the role that plants may play in the current climate as well as in climates of the past.

4.2 Introduction

The local impact of forests on climate at both low and high latitudes is relatively well understood. In the northern high latitudes, trees create warming due to low albedo (e.g. *Bonan et al.* [1992]), particularly when leaves cover snow, and increases in water vapor due to transpiration [*Swann et al.*, 2010]. In the tropics, trees increase evapotranspiration from the surface keeping temperatures cool and precipitation rates high by recycling water through the surface back to the atmosphere. The local impact of trees in mid latitudes is less well constrained. Changes in both albedo and transpiration compete to control the local surface

temperature response and models disagree on the net effect of adding tree cover in mid latitudes [*Bonan*, 2008].

Changes in land cover have both biophysical and biochemical effects, modifying energy, water, carbon and momentum fluxes from the surface. In general, vegetation is thought to have primarily local effects on climate by modifying local energy balances. Changes in carbon fluxes associated with changes in vegetation cover, on the other hand, are long-lived and therefore transported throughout the atmosphere to modify the global CO_2 concentration. While small compared to the radiative forcing from fossil fuel emissions, the carbon emitted by the land surface has global radiative forcing effects.

Afforestation, the re-growth of trees on non-forested land, is one of the proposed actions for climate change mitigation as it is assumed that the growth of forests will take up and store carbon from the atmosphere. Carbon stocks of forests may be included in a market for trading carbon credits worldwide. The expansion of forest crops for conversion to biofuel is also a real possibility, one that is proposed as potential land cover for representative concentration pathways specified in the IPCC AR5 protocol [*Moss et al.*, 2010].

In this study we investigate the impact of large-scale changes in mid latitude deciduous tree cover and identify processes that control the interaction between ecosystems and climate. We find that large increases in tree cover at mid latitudes decreases albedo across the northern hemisphere leading to widespread warming and a shift of the general circulation. As the intertropcial convergence zone (ITCZ) moves northward, precipitation totals rise over the Sahel and Sahara regions in Africa and decrease over parts of the Amazon basin. This results in a drop in productivity over the Amazon and creates conditions for the growth of plants in the Sahara. We suggest the hypothesis that mid latitude tree cover may be partly responsible for supporting sufficient precipitation to maintain green vegetation over the Sahel and lower Sahara region ∼6000 years ago during the Mid Holocene.

4.3 The 6Kya problem

The Sahel and lower Sahara region in Africa are thought to have been far wetter 6Kya. These regions lie on the edge of the Tropics but are currently dry and, in the case of the Sahara, home to little vegetation. Paleo-vegetation proxies in Africa indicate that at 6Kya grassland steppe was found as far north as 23° and desert vegetation was not found south of 20° [*Jolly et al.*, 1998]. Paleo proxies also indicate that lakes were more widespread in Africa [*Street-Perrott et al.*, 1989]. Two mechanisms have been invoked for how the Sahara was capable of maintaining sufficient precipitation for vegetation in the past despite its current state as desert. First, the orbital forcing at 6Kya was such that the earth was slightly closer to the sun in the summer and farther in the winter compared to present day. This leads to an increase in the seasonality of temperature in the Northern Hemisphere with warmer summers and cooler winters [*Braconnot et al.*, 2007a].

Charney et al. [1975] (as well as *Charney* [1975]) introduced a second mechanism as a theory for why the Sahara is maintained as a desert. The contrast in albedo between a bright

desert and a dark ocean surface maintains an east-west circulation cycle with updraft over the ocean and enhanced downwelling of hot, dry air over the desert. This east-west circulation couples with the north-south circulation associated with the Hadley cell to reinforce the hot, dry conditions in the Sahara desert. If the desert is instead vegetated, the surface is darker and provides less of an albedo contrast to the adjacent ocean reducing the zonal circulation. By removing the east-west circulation component of the downwelling of hot, dry air the Sahara is allowed to get wetter. The Charney hypothesis does not explain how the earth may move from one state (desert) to the other (vegetated) but does provide the concept of multiple stable states and suggests that if the Sahara were somehow vegetated, it may maintain its own precipitation by decreasing the downwelling of hot, dry air relative to the desert state.

Modeling work has been done attempting to incorporate and evaluate the effects of orbital forcing, local vegetation changes and changes in ocean surface temperatures (e.g. *Joussaume et al.* [1995]; *Braconnot et al.* [2000]) to explain the difference in vegetation distribution between 6Kya and today in the Sahara/Sahel region. A northward shift in the ITCZ is observed in the model experiments of the second phase of the paleo model intercomparison project (PMIP2) due simply to the change in orbital forcing. The vegetation in PMIP2 experiments is specified as present day vegetation (as is represented by each participating modeling group). Some of the model runs in the project also include dynamic vegetation, an interactive calculation of what vegetation type is best suited for the conditions allowing for changing vegetation distributions. Within the PMIP2 project, none of the model experiments, either with dynamic vegetation or not, are able to reproduce a shift in the ITCZ far enough north to sustain sufficient precipitation to support the observed changes in vegetation *Braconnot et al.* [2007a].

Additional modeling work outside of the PMIP projects have had greater success (i.e. *Claussen and Gayler* [1997]; *Claussen et al.* [1999]; *Levis et al.* [2004]; *Zeng et al.* [1999]). *Bonfils et al.* [2001] find that the initial albedo value of the hot desert in a model determines the change in albedo when vegetation establishes and thus the initial albedo controls the potential for response to changes in vegetation cover. *Levis et al.* [2004] show a sufficient increase in precipitation for 6Kya using the CCSM2 climate model. The increase in precipitation is found to depend on the albedo of the bare soil within northern Africa, so that changes in soil texture and color due to moistening have a large impact on the shift of the ITCZ northward. The response is also partly due to ocean feedbacks, but primarily they enlist local land surface feedbacks to explain changes in precipitation. In contrast, we propose that an additional forcing, from the remote effects of mid-latitude vegetation changes, could also play a role in the shift of precipitation patterns at 6Kya as compared to today.

Vegetation distributions from 6Kya show that deciduous forests were widespread in mid latitudes, especially in Europe [*Prentice et al.*, 1998]. The distribution of grasslands in Eurasia was diminished and replaced by deciduous trees [*Tarasov et al.*, 1998] consistent with the conversion of vegetation we impose in our experiments. The conversion of cultivated land to trees over North America is defensible as a realistic representation of prior vegetation, however the natural grasslands of North America appear to have retained their distributions from 6Kya to present [*Prentice et al.*, 1998]. Our conversion of cultivated land and C3

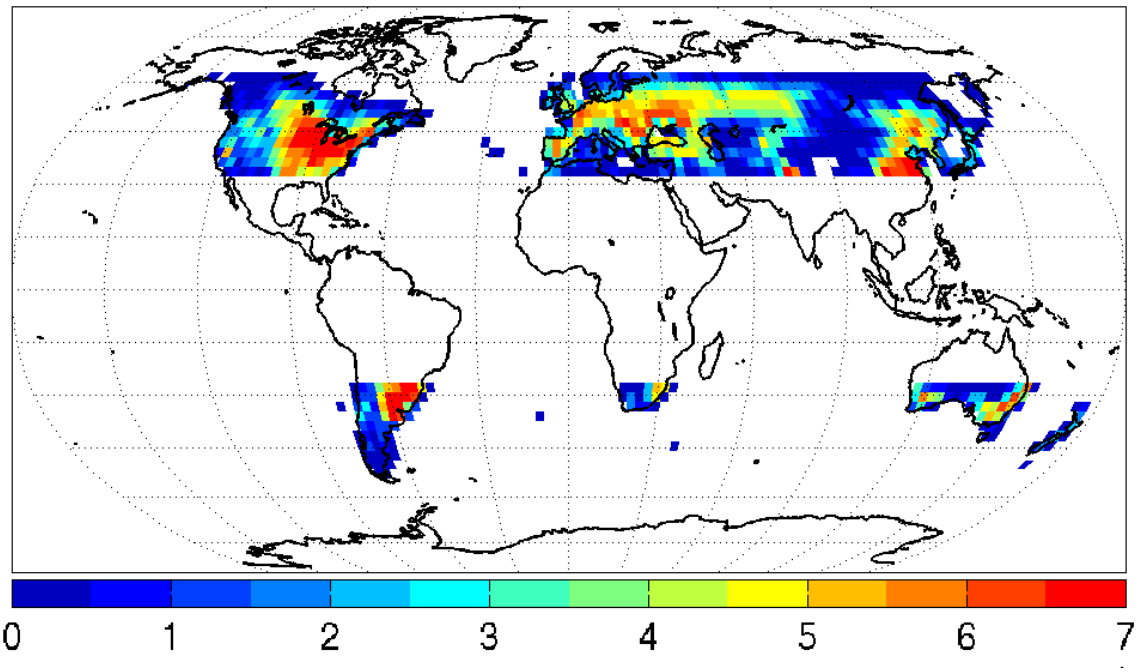

Figure 4.1. **Map of New Trees:** Map of area of new deciduous trees in V-FO and V-IO in units of $10^4 km^2$. The area is occupied by C3 grasslands and cultivated land in C-FO and C-IO. The total area converted is 2.1 x $10^7 km^2$. New vegetation is added between 30° and 60° both north and south.

grassland to deciduous trees is qualitatively consistent with the published maps of vegetation cover reconstruction over Europe and eastern North America [*Prentice et al.*, 2000]. We suggest that this study provides a maximum estimate of the effect of deciduous trees in mid latitudes on remote circulation and precipitation patterns.

4.4 Methods

To investigate the role of vegetation changes in mid latitudes, we use the National Center for Atmospheric Research (NCAR) Community Atmosphere and Land models with an interactive carbon cycle (CAM 3.0-CLM 3.5-CASA') [*Collins et al.*, 2006; *Doney et al.*, 2006; *Kiehl et al.*, 2006]. All mid latitude area in the map of present day vegetation between 30° and 60° currently occupied by either C3 grasses or agriculture is converted to broad-leaf deciduous trees and all previously designated vegetation is left unmodified, as are glaciers and lakes. The converted area totals 21,000,000 km^2. This particular conversion (from grass and crops to forest) is used to simulate the re-forestation of current grasslands. The area of forest represented by the vegetation experiments is qualitatively consistent with the distribution of vegetation inferred from proxy records of 6Kya (see Section 4.3). The exact distribution of

vegetation used in these simulations is extreme and should be viewed as a maximum effect of afforestation in mid latitudes.

The model control (C, standard land cover) and experiment (V, modified land cover) are each run with two representations of the ocean: an interactive slab ocean model (IO) with thermodynamic sea-ice [*Oleson et al.*, 2008], and a fixed ocean (FO) wherein sea surface temperature and sea-ice are set to the monthly-mean conditions in the C-IO control run. The four model runs are integrated for 30 years, and the results presented are averages of the last 20 years. The spin-up time of 10 years is sufficient to bring climate variables into equilibrium. The spatial resolution of the model is T42 which corresponds to approximately 2.8° by 2.8° gridcells. Values in Tables 4.1-4.3 are reported as the mean over three months (June, July, and August - JJA, and December, January, and February - DJF) or the annual mean over either the land or ocean area in the averaging region. Water import is calculated as the flux into the averaging region. Significance is calculated using an estimated 10 degrees of freedom for each 20-year period and reported as p-values where a p-value of 0.05 indicates that we reject the null hypothesis that the anomaly is zero with 95% confidence (shown in bold).

Due to the mass fixer in the non-conservative semi-lagrangian transport scheme we cannot calculate the actual model transport of water vapor [*Rasch and Williamson*, 1990]. We are able to estimate model transport but using this estimate we cannot close the water budget, even on annual time scales, indicating that the estimated transport is far from the actual transport experienced in the model. As the true model transport is unknown and the turnover time of water in the atmosphere is assumed to be of order 10 days, we infer an effective transport for each month as the residual of P-E (including transpiration, canopy evaporation, ground evaporation and ocean evaporation). This effective import is used in Tables 4.1, 4.2, and 4.3.

Fields from our equilibrium climate model experiments will be reported as anomalies, represented by $\Delta\phi$, and are calculated as the difference in climate variable ϕ simulated by the experiments with expanded forest cover and present day vegetation distribution with the same ocean module (either ΔV-IO or ΔV-FO). The vegetation interacts with climate through changing stomatal conductance, leaf area, and mass and hence albedo and transpiration. The ΔV-FO anomalies are an approximation of the response to direct forcing from vegetation expansion as any feedbacks associated with changes in ocean temperature or sea ice-cover are damped. The ΔV-IO anomalies can be considered as the whole earth system response including the response both to direct forcing and any associated feedbacks. The difference between the two anomalies, $\delta\Delta\phi = \Delta\phi$ (ΔV-IO) - $\Delta\phi$ (ΔV-FO), represents the additional feedback (from both land and ocean) experienced when the ocean and sea ice are allowed to adjust. Average anomalies and control values are calculated over the mid-latitudes defined by the region between 30° and 60° both north (Table 4.1) and south (Table 4.2) and also as the northern hemisphere mid and high latitude mean calculated as the mean over the region north of 30° N (Table 4.3).

			Interactive						Fixed					
Month	Variable Name	Units	Land			Ocean			Land			Ocean		
Annual Mean			μ	Δ	p	μ	Δ	p	μ	Δ	p	μ	Δ	p
	Surf. Air Temp.	K	280.77	1.29	**0.00**	285.99	1.05	**0.00**	280.71	0.54	0.08	285.95	0.04	0.25
	Precipitation	mm/day	1.74	0.01	0.41	2.82	0.00	0.51	1.74	-0.05	0.34	2.80	-0.09	0.21
	Albedo	albedo	0.22	-0.05	**0.00**	0.07	0.00	0.41	0.22	-0.05	**0.00**	0.08	0.00	0.23
	Latent Heat	Wm-2	33.64	1.26	0.26	80.49	2.01	0.29	33.53	-0.30	0.25	79.79	-1.73	0.32
	Sensible Heat	Wm-2	26.43	7.94	0.13	21.33	-0.73	0.49	26.31	8.82	**0.00**	21.40	-0.04	0.40
	Water Vapor	kgm-2	13.16	1.09	**0.00**	20.75	1.30	**0.00**	13.08	0.35	0.14	20.70	0.17	0.32
	Low Cloud	fraction	0.29	-0.03	0.08	0.54	-0.01	0.27	0.29	-0.03	**0.04**	0.54	0.01	0.32
	Eff. Water Import	kg s-1	-	-	-	-2421.26	-15.51	0.57	-	-	-	-2421.56	12.30	0.46
	Snow Fraction	fraction	0.12	-0.01	0.15	-	-	-	0.13	0.00	0.16	-	-	-
	Transpiration	Wm-2	9.86	3.48	**0.00**	-	-	-	9.70	2.65	**0.00**	-	-	-
JJA														
	Surf. Air Temp.	K	293.50	1.83	**0.00**	290.01	1.09	**0.00**	293.42	1.25	**0.00**	290.00	0.09	0.21
	Precipitation	mm/day	2.26	-0.08	0.34	1.63	-0.01	0.55	2.23	-0.11	0.25	1.62	-0.09	0.33
	Albedo	albedo	0.18	-0.04	**0.00**	0.05	0.00	0.56	0.18	-0.04	**0.00**	0.05	0.00	0.67
	Latent Heat	Wm-2	63.82	1.30	0.34	42.14	2.12	0.28	63.71	-1.86	0.25	42.07	-1.25	0.57
	Sensible Heat	Wm-2	49.20	15.45	**0.00**	4.72	0.11	0.89	49.23	16.40	**0.00**	4.75	0.20	0.79
	Water Vapor	kgm-2	20.78	1.92	**0.00**	28.97	1.69	**0.00**	20.60	0.96	**0.00**	28.75	0.47	**0.03**
	Low Cloud	fraction	0.17	-0.03	**0.00**	0.61	0.00	0.45	0.17	-0.03	**0.00**	0.61	0.02	**0.01**
	Eff. Water Import	kg s-1	-	-	-	-2843.00	-21.82	0.51	-	-	-	-2844.81	-15.99	0.59
	Snow Fraction	fraction	0.00	0.00	0.59	-	-	-	0.00	0.00	0.63	-	-	-
	Transpiration	Wm-2	24.40	6.57	**0.00**	-	-	-	24.12	4.76	**0.00**	-	-	-
DJF														
	Surf. Air Temp.	K	267.98	1.22	**0.00**	282.03	1.01	**0.00**	268.13	-0.09	0.32	281.94	-0.01	0.35
	Precipitation	mm/day	1.40	0.08	0.16	4.08	0.05	0.15	1.41	0.02	0.37	3.97	0.00	0.43
	Albedo	albedo	0.28	-0.07	**0.00**	0.11	0.00	0.17	0.28	-0.07	**0.00**	0.11	0.00	**0.01**
	Latent Heat	Wm-2	10.22	1.99	0.12	114.37	3.96	0.26	10.34	1.24	0.22	112.44	0.65	0.56
	Sensible Heat	Wm-2	3.93	1.00	0.50	43.52	-1.64	0.16	3.74	1.67	**0.00**	43.51	0.36	**0.03**
	Water Vapor	kgm-2	7.29	0.48	**0.01**	14.73	0.88	**0.00**	7.22	0.02	0.42	14.73	-0.04	0.73
	Low Cloud	fraction	0.43	-0.02	0.31	0.55	-0.01	0.12	0.43	-0.01	0.14	0.55	-0.01	0.30
	Eff. Water Import	kg s-1	-	-	-	-1941.09	-17.43	0.55	-	-	-	-1941.07	23.49	0.29
	Snow Fraction	fraction	0.32	-0.02	**0.00**	-	-	-	0.32	0.01	**0.00**	-	-	-
	Transpiration	Wm-2	0.79	0.65	**0.00**	-	-	-	0.77	0.46	**0.00**	-	-	-

Table 4.1. **Climate Field Values, 30°N to 60°N:** Variables of interest are shown from the four global climate model runs averaged over the entire year (annual mean), summer months (June, July, and August - JJA), and winter months (December, January, and February - DJF). Values are reported as the mean of the control run (C-FO and C-IO), the anomaly (ΔV-FO or ΔV-IO), and p-value of significance for spatial averages over either land or ocean area north of 30°N and south of 60°N. The exception is effective water import (see Section 4.4) which is an estimate of the monthly average $P - E$. p-values of 0.05 or less indicate significance of at least 95% confidence and are shown in bold.

			Interactive						Fixed					
Month	Variable Name	Units	Land			Ocean			Land			Ocean		
Annual Mean			μ	Δ	p	μ	Δ	p	μ	Δ	p	μ	Δ	p
	Surf. Air Temp.	K	288.51	-0.49	0.18	283.21	0.20	0.24	288.38	-0.49	**0.03**	283.20	0.00	0.91
	Precipitation	mm/day	1.52	0.20	0.48	2.64	0.00	0.58	1.53	0.18	0.54	2.64	-0.02	0.46
	Albedo	albedo	0.16	-0.04	**0.00**	0.07	0.00	0.47	0.16	-0.04	**0.00**	0.07	0.00	0.66
	Latent Heat	Wm-2	38.15	5.22	0.41	65.47	0.24	0.58	38.49	4.05	0.52	65.46	-0.36	0.40
	Sensible Heat	Wm-2	51.22	6.70	**0.02**	11.82	0.07	0.71	51.13	7.01	0.06	11.97	0.09	0.64
	Water Vapor	kgm-2	16.57	0.28	0.55	15.85	0.20	0.24	16.42	0.23	0.56	15.84	0.02	0.69
	Low Cloud	fraction	0.20	0.00	0.63	0.53	0.00	0.46	0.20	0.00	0.39	0.53	0.00	0.66
	Eff. Water Import	kg s-1	-	-	-	-2148.95	-64.56	0.23	-	-	-	-2138.74	60.92	0.21
	Snow Fraction	fraction	0.00	0.00	0.66	-	-	-	0.00	0.00	0.66	-	-	-
	Transpiration	Wm-2	14.37	6.29	**0.00**	-	-	-	14.52	5.54	**0.00**	-	-	-
JJA														
	Surf. Air Temp.	K	282.44	-0.54	**0.02**	281.70	0.20	0.07	282.26	-0.36	**0.00**	281.69	-0.01	0.82
	Precipitation	mm/day	1.26	0.06	0.78	3.25	0.01	0.68	1.36	0.03	0.92	3.24	0.03	0.41
	Albedo	albedo	0.17	-0.04	**0.00**	0.10	0.00	0.08	0.17	-0.04	**0.00**	0.10	0.00	0.07
	Latent Heat	Wm-2	22.42	2.34	0.50	78.14	0.52	0.52	22.36	2.28	0.36	78.20	0.46	0.39
	Sensible Heat	Wm-2	5.59	2.48	**0.01**	17.87	-0.12	0.72	5.58	1.82	0.14	18.09	0.25	0.47
	Water Vapor	kgm-2	13.53	-0.15	0.67	13.41	0.11	0.56	13.47	-0.03	0.93	13.39	-0.03	0.83
	Low Cloud	fraction	0.26	-0.01	0.61	0.54	0.00	0.26	0.27	-0.01	0.19	0.54	0.00	0.47
	Eff. Water Import	kg s-1	-	-	-	-2027.59	-61.11	0.33	-	-	-	-2026.06	90.19	**0.00**
	Snow Fraction	fraction	0.00	0.00	**0.00**	-	-	-	0.00	0.00	**0.00**	-	-	-
	Transpiration	Wm-2	7.02	2.93	**0.00**	-	-	-	6.81	2.89	**0.00**	-	-	-
DJF														
	Surf. Air Temp.	K	294.89	-0.58	0.22	284.85	0.20	0.47	294.62	-0.59	0.06	284.85	0.00	0.98
	Precipitation	mm/day	1.95	0.43	0.12	2.07	-0.04	0.47	1.94	0.45	0.06	2.06	-0.04	0.46
	Albedo	albedo	0.15	-0.04	**0.00**	0.05	0.00	0.91	0.15	-0.04	**0.00**	0.05	0.00	0.97
	Latent Heat	Wm-2	54.32	10.30	0.18	51.04	0.13	0.76	55.39	8.01	0.38	50.95	-0.77	0.41
	Sensible Heat	Wm-2	98.51	9.59	**0.04**	6.42	0.08	0.87	98.72	9.66	0.06	6.39	0.08	0.91
	Water Vapor	kgm-2	20.14	0.74	0.24	18.85	0.21	0.11	19.89	0.61	0.18	18.79	0.11	0.40
	Low Cloud	fraction	0.15	0.00	0.66	0.55	0.00	0.37	0.15	0.01	0.29	0.54	0.00	0.66
	Eff. Water Import	kg s-1	-	-	-	-2312.31	-115.90	0.06	-	-	-	-2286.71	-15.82	0.69
	Snow Fraction	fraction	0.00	0.00	1.00	-	-	-	0.00	0.00	1.00	-	-	-
	Transpiration	Wm-2	20.93	10.87	**0.00**	-	-	-	21.54	9.16	**0.00**	-	-	-

Table 4.2. Climate Field Values, **30°S to 60°S:** As in Table 4.1 but for the region between 30°S and 60°S.

			Interactive						Fixed					
Month	Variable Name	Units	Land			Ocean			Land			Ocean		
Annual Mean			μ	Δ	p	μ	Δ	p	μ	Δ	p	μ	Δ	p
	Surf. Air Temp.	K	277.59	1.25	**0.00**	281.26	1.10	**0.00**	277.46	0.42	**0.04**	281.01	0.05	0.44
	Precipitation	mm/day	1.69	0.03	0.30	2.45	0.03	0.51	1.69	-0.04	0.36	2.43	-0.06	0.27
	Albedo	albedo	0.25	-0.04	**0.00**	0.13	0.00	0.19	0.25	-0.04	**0.00**	0.13	0.00	0.07
	Latent Heat	Wm-2	29.43	1.13	0.30	66.56	1.66	0.28	29.30	-0.22	0.24	66.03	-1.48	0.30
	Sensible Heat	Wm-2	21.39	6.04	0.10	20.10	-0.67	0.38	21.29	6.82	**0.00**	20.14	-0.21	0.43
	Water Vapor	kgm-2	12.22	1.03	**0.00**	17.92	1.20	**0.00**	12.14	0.31	0.15	17.85	0.18	0.37
	Low Cloud	fraction	0.36	-0.02	0.11	0.57	0.00	0.36	0.36	-0.02	0.06	0.58	0.01	0.33
	Eff. Water Import	kg s-1	-	-	-	-2568.05	-17.16	0.53	-	-	-	-2568.97	13.00	0.47
	Snow Fraction	fraction	0.20	-0.01	**0.00**	-	-	-	0.21	0.00	**0.00**	-	-	-
	Transpiration	Wm-2	8.61	2.77	**0.00**	-	-	-	8.46	2.07	**0.00**	-	-	-
JJA														
	Surf. Air Temp.	K	291.21	1.61	**0.00**	287.01	0.98	**0.00**	291.14	1.01	**0.00**	286.97	0.10	0.45
	Precipitation	mm/day	2.21	-0.02	0.47	1.50	0.02	0.59	2.19	-0.08	0.25	1.49	-0.05	0.51
	Albedo	albedo	0.19	-0.03	**0.00**	0.10	-0.01	**0.00**	0.19	-0.03	**0.00**	0.10	0.00	0.09
	Latent Heat	Wm-2	58.00	1.26	0.44	35.67	1.49	0.33	57.82	-1.48	0.21	35.50	-1.16	0.49
	Sensible Heat	Wm-2	42.28	11.62	**0.00**	4.84	-0.09	0.87	42.28	12.53	**0.00**	4.89	-0.04	0.81
	Water Vapor	kgm-2	20.04	1.82	**0.00**	25.92	1.65	**0.00**	19.90	0.85	**0.00**	25.71	0.51	**0.00**
	Low Cloud	fraction	0.25	-0.02	**0.00**	0.64	0.00	0.52	0.25	-0.02	**0.00**	0.64	0.02	**0.00**
	Eff. Water Import	kg s-1	-	-	-	-3000.81	-25.11	0.41	-	-	-	-3004.43	-13.74	0.64
	Snow Fraction	fraction	0.02	0.00	**0.00**	-	-	-	0.02	0.00	**0.00**	-	-	-
	Transpiration	Wm-2	22.07	5.23	**0.00**	-	-	-	21.80	3.73	**0.00**	-	-	-
DJF														
	Surf. Air Temp.	K	264.03	1.24	**0.00**	275.67	1.06	**0.00**	264.05	-0.13	0.14	275.06	-0.01	0.16
	Precipitation	mm/day	1.33	0.09	0.06	3.43	0.07	0.25	1.35	0.01	0.36	3.36	-0.01	0.40
	Albedo	albedo	0.32	-0.06	**0.00**	0.12	0.00	0.54	0.32	-0.05	**0.00**	0.13	0.00	**0.04**
	Latent Heat	Wm-2	8.21	1.56	0.12	93.44	3.43	0.15	8.31	0.95	0.22	92.03	0.34	0.55
	Sensible Heat	Wm-2	0.66	0.87	0.40	39.06	-1.09	0.09	0.48	1.39	**0.00**	38.97	0.09	0.28
	Water Vapor	kgm-2	6.47	0.44	**0.00**	12.28	0.75	**0.00**	6.40	0.02	0.41	12.24	-0.01	0.86
	Low Cloud	fraction	0.48	-0.01	0.41	0.57	-0.01	0.15	0.49	-0.01	0.22	0.58	-0.01	0.30
	Eff. Water Import	kg s-1	-	-	-	-2056.26	-17.77	0.55	-	-	-	-2055.12	22.70	0.29
	Snow Fraction	fraction	0.43	-0.02	**0.00**	-	-	-	0.43	0.01	**0.00**	-	-	-
	Transpiration	Wm-2	0.61	0.51	**0.00**	-	-	-	0.60	0.36	**0.00**	-	-	-

Table 4.3. Climate Field Values, **30°N to 90°N:** As in Table 4.1 but for the region between 30°S and 90°N.

4.5 Results and Discussion

4.5.1 Climate Effects of Afforestation

The addition of trees at mid latitudes results in the warming (ΔT) of the northern hemisphere (Figure 4.2). Local warming over land is seen in ΔV-FO and hemispheric-wide warming is seen in ΔV-IO. The mid latitude land warms by 1.5 (0.46) °C in the annual mean and 1.7 (1.1) °C in summer for IO (FO) (see Table 4.1). In high latitudes, the fraction of snow cover decreases in ΔV-IO with the addition of mid latitude trees during winter and spring months (Table 4.1, DJF; Figure 4.3, MAM).

Notably, the ITCZ appears to move northward in both ΔV-IO and ΔV-FO (Figure 4.5) by up to 2° globally in ΔV-IO (Figure 4.17). The shift happens globally, but over Africa precipitation reaches into the Sahel and lower Sahara desert. In a latitudinal transect of Africa, precipitation increases by more than 200 mm/yr north of $20°N$ in IO and up to 150 mm/yr in FO (Figure 4.4). The precipitation increase in ΔV-IO is consistent with predictions of the necessary excess precipitation needed to maintain steppe vegetation observed to inhabit the region at 6Kya [*Joussaume et al.*, 1999].

Surface albedo decreases in the mid-latitudes with the addition of trees (Figure 4.6) and is the primary cause of the warming by causing an increase in absorbed solar radiation at the surface. The albedo difference is evident in all seasons, indicating that the modeled representation of deciduous forest albedo is darker than that of grasses and the change in albedo is not entirely due to snow masking by trees. Figure 4.7 shows that the largest Δ of absorbed solar radiation at the surface in mid latitudes occurs during the summer and fall. In addition to the albedo changes over land, there are albedo changes over ocean in both the high northern and southern latitudes associated with a decrease in sea ice area (Figure 4.8, also Figure 4.7).

4.5.2 Water Fluxes

The flux of water from the surface by transpiration increases with the addition of trees as compared to grasses (Figure 4.10). The net change in latent heat flux is mostly near zero as the increase in transpiration flux is largely balanced by a decrease in ground evaporation flux (Figure 4.11). As the net change in latent heat flux is small, sensible heat fluxes balance almost all of the additional absorbed solar radiation (Figure 4.13). As albedo decreases with the expansion of trees, the additional absorbed solar radiation is primarily transferred out of the surface as sensible heat at an almost one to one ratio in Wm^{-2} (Figure 4.14).

Though the net latent heat flux is small, the compensating fluxes in transpiration and ground evaporation are not. At first consideration, trees shelter the ground from the atmosphere and so ground evaporation fluxes are expected to be lower under trees due to a decrease in radiation reaching the surface. This would lead to the expectation that the decrease in ground evaporation is a direct consequence of the increase in leaf area (measured

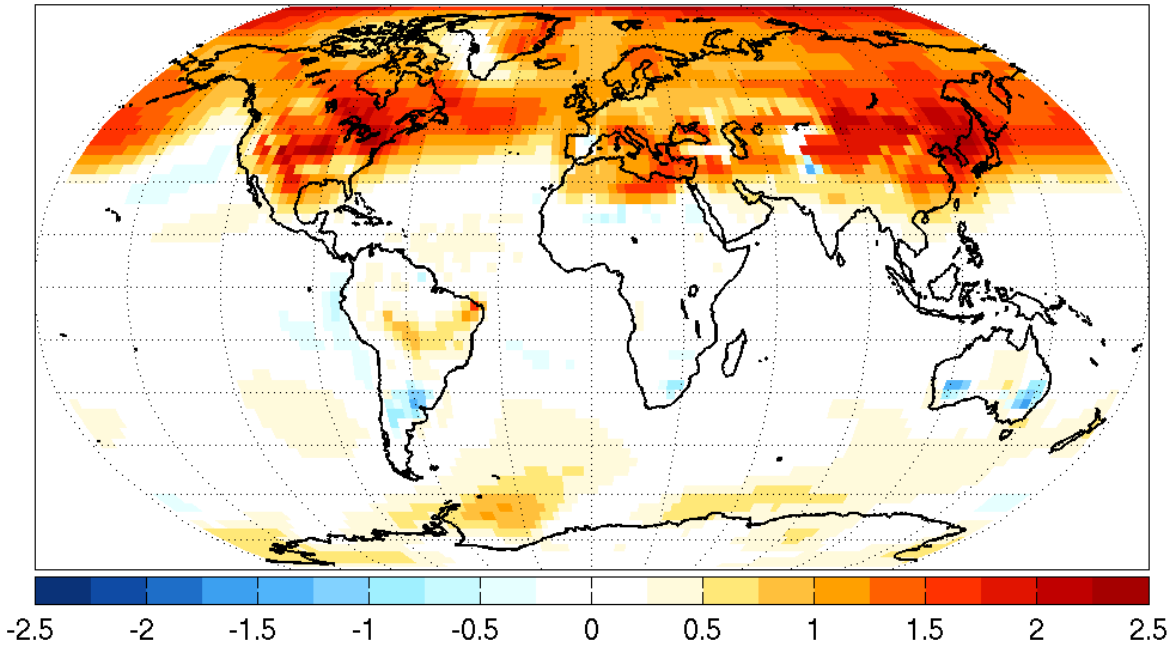

(a) ΔV-IO Temperature (Kelvin)

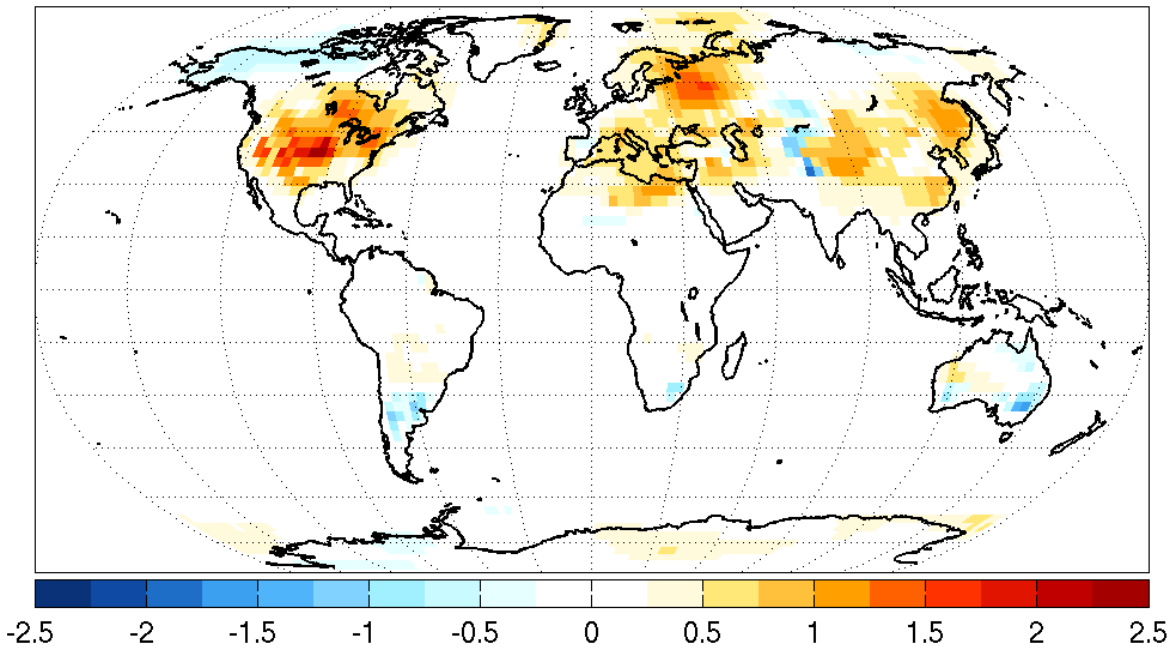

(b) ΔV-FO Temperature (Kelvin)

Figure 4.2. **Annual Mean ΔTemperature:** The anomaly in near surface temperature (ΔT) in Kelvin for a model experiment where trees are introduced on C3 grasslands and cultivated land with **(a)** an interactive ocean (ΔV-IO) and **(b)** a fixed ocean (ΔV-FO).

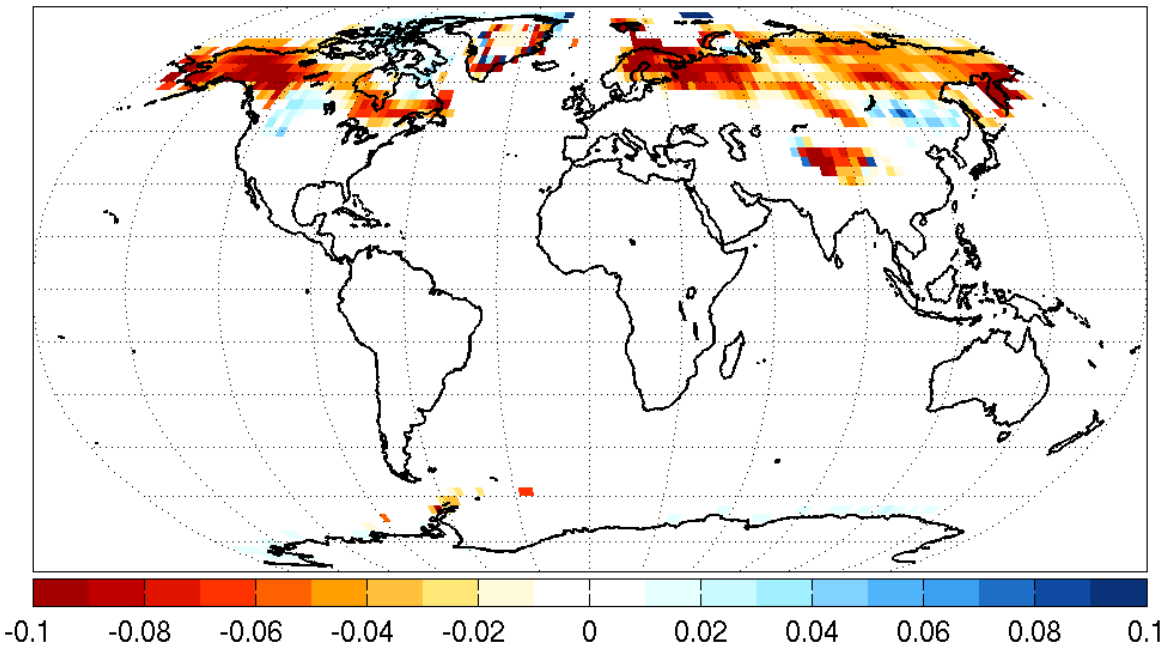

(a) ΔV-IO Snow Cover (Fraction)

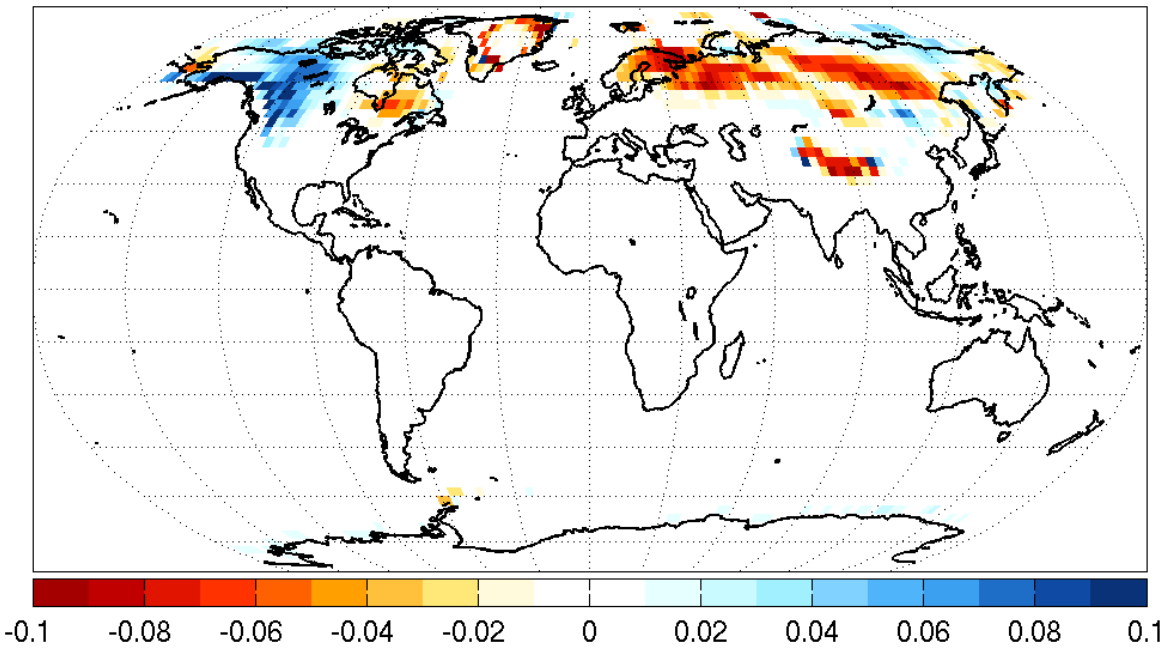

(b) ΔV-FO Snow Cover (Fraction)

Figure 4.3. **Annual Mean ΔSnow Cover (Fraction):** The same as Figure 4.2 for Δ fractional snow cover.

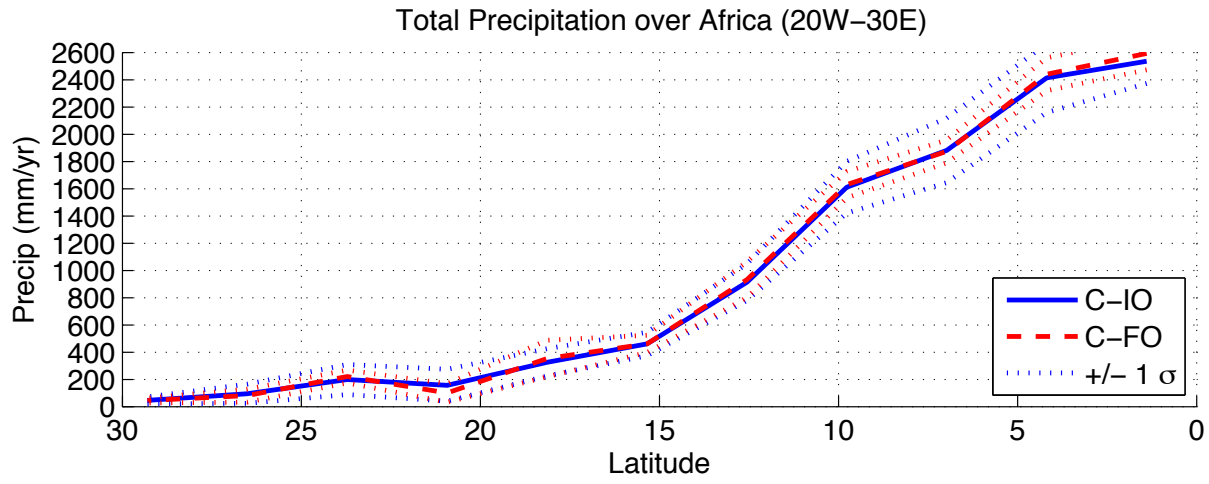

(a) Total Precipitation Transect over Africa

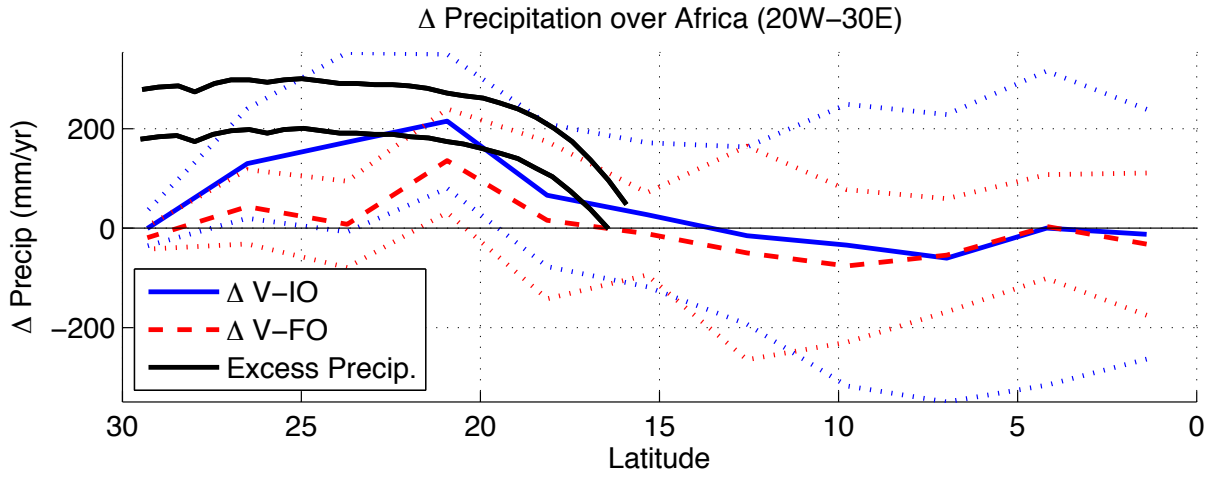

(b) Anomalous Precipitation Transect over Africa

Figure 4.4. **Precipitation over Africa (20°W to 30°E):** Zonal precipitation transects averaged over Africa (20°W to 30°E) for **(a)** total precipitation in mm/yr for C-IO (blue) and C-FO (red) as well as the +/- 1 σ error bars (dotted lines). **(b)** the Δprecipitation in mm/yr for ΔV-IO (blue) and ΔV-FO (red) as well as the +/- 1 σ error bars (dotted lines). Excess precipitation needed to maintain steppe vegetation observed to inhabit the region at 6Kya as in *Joussaume et al.* [1999].

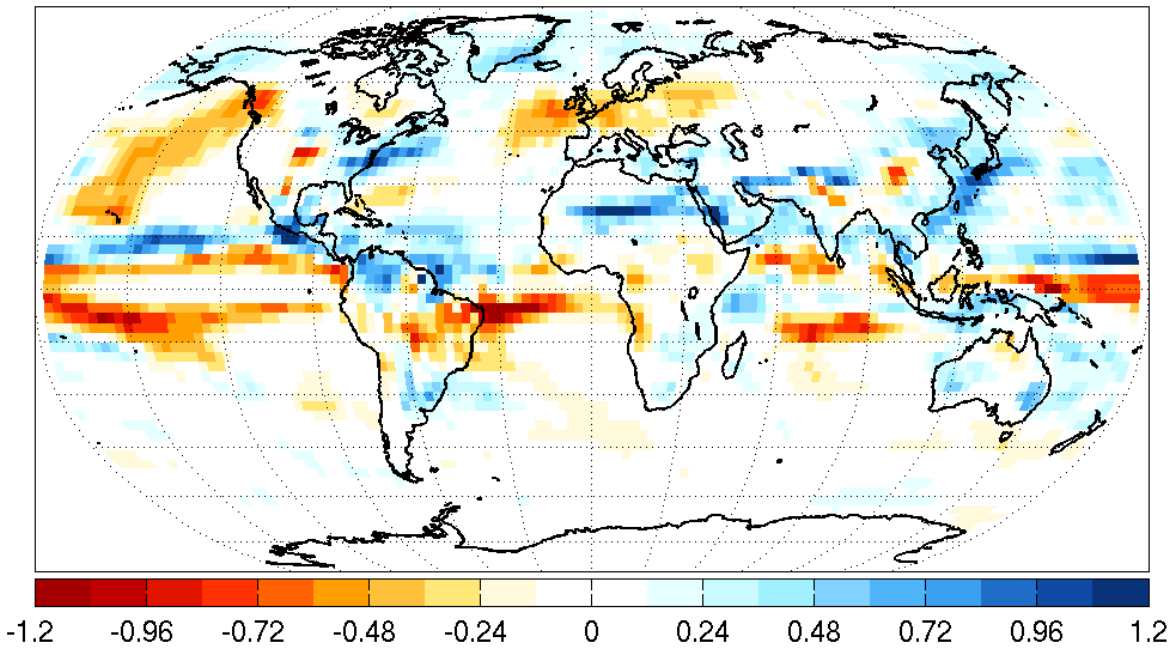

(a) ΔV-IO Precipitation (mm/day)

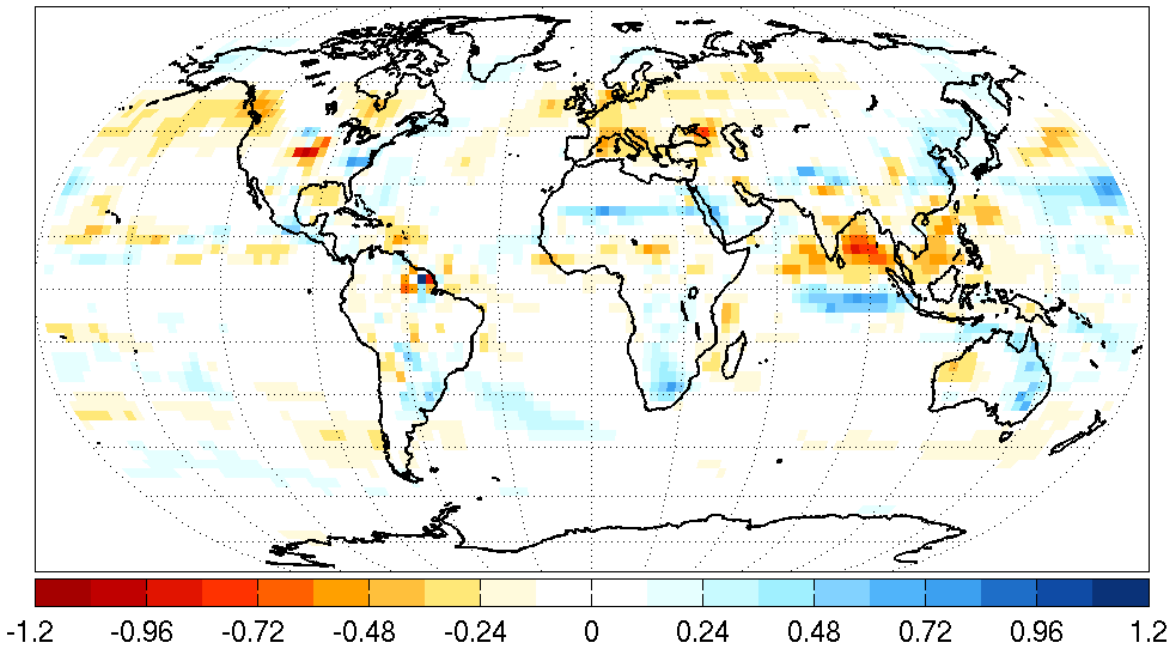

(b) ΔV-FO Precipitation (mm/day)

Figure 4.5. **Annual Mean ΔPrecipitation (mm/day):** The same as Figure 4.2 for Δ precipitation in mm/day.

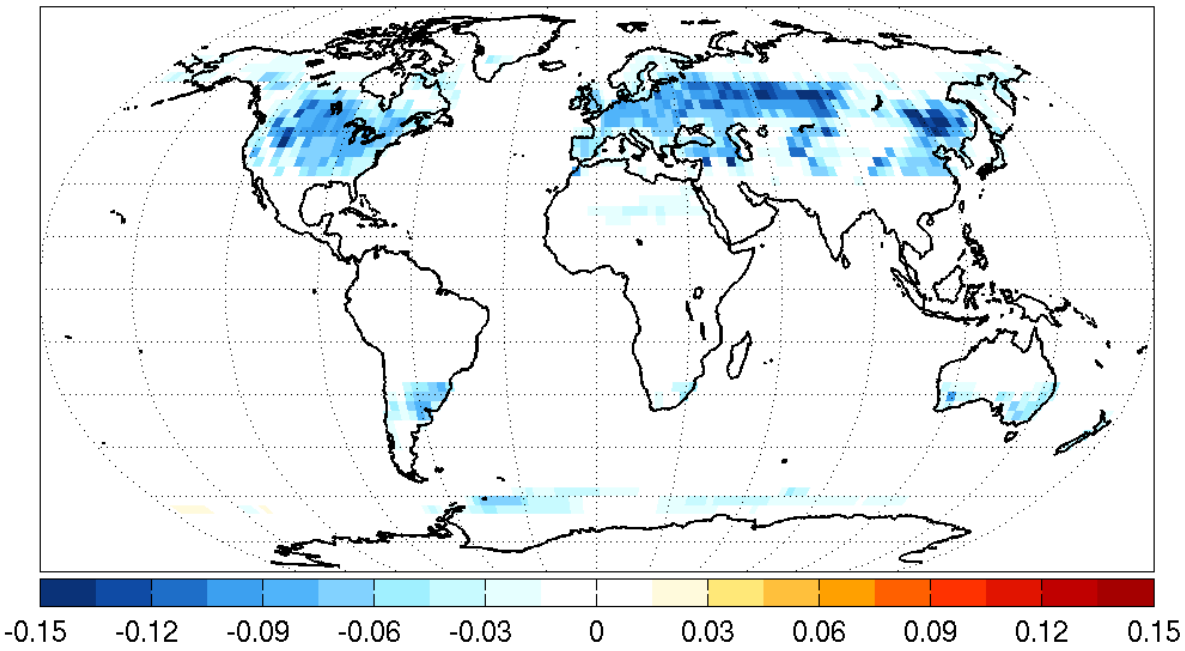

(a) ΔV-IO Albedo

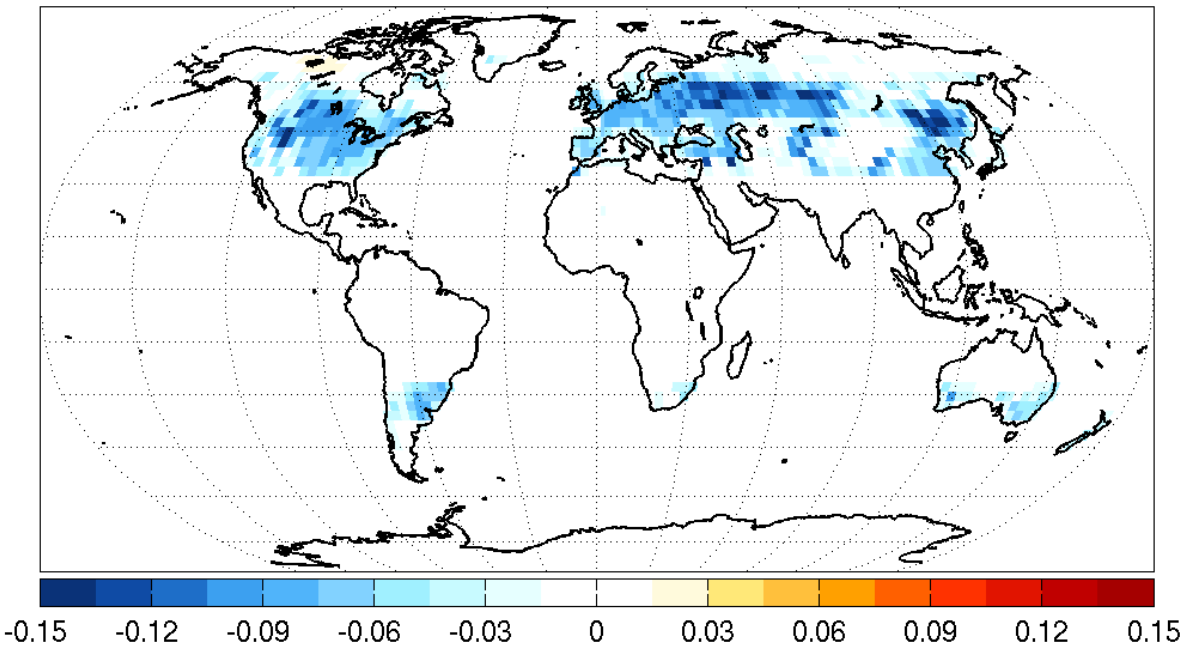

(b) ΔV-FO Albedo

Figure 4.6. **Annual Mean ΔAlbedo:** The same as Figure 4.2 for Δ surface albedo.

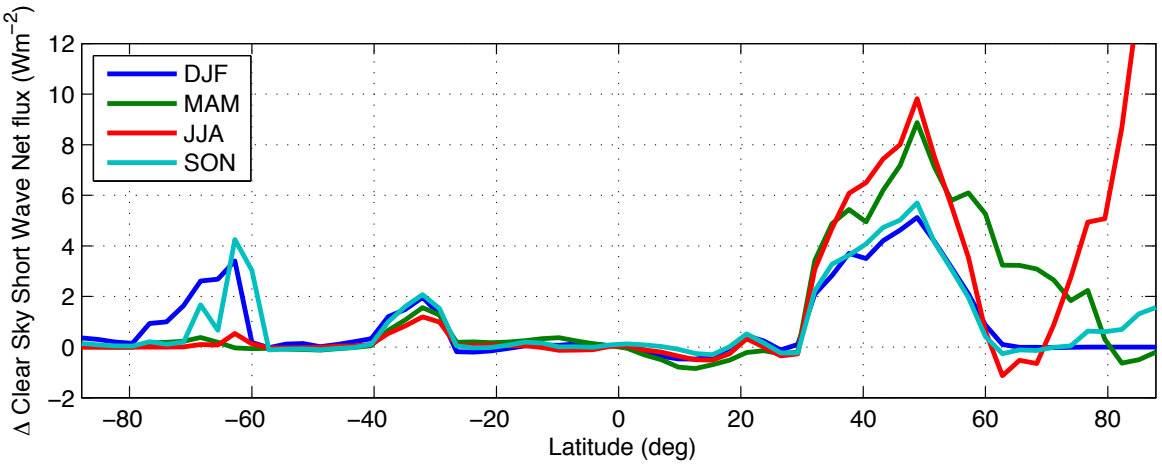

Figure 4.7. **Zonal ΔSW Absorbed:** A zonally averaged profile of Δ absorbed short wave radiation in Wm^{-2} for ΔV-IO due to the change in albedo seen in Figure 4.6a.

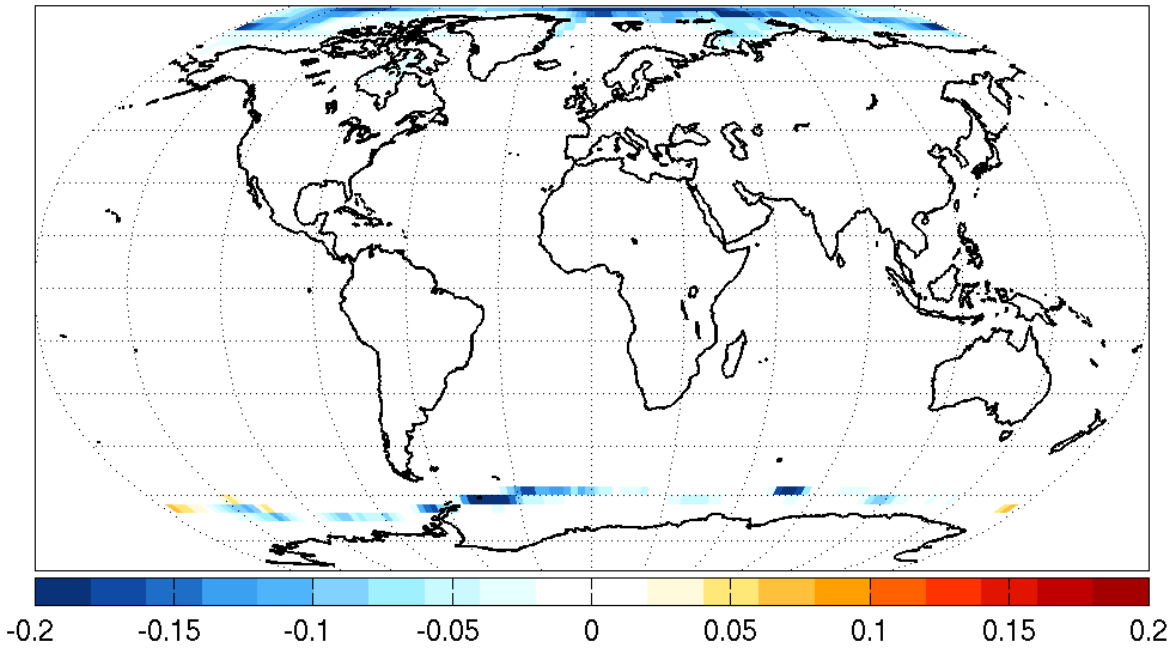

Figure 4.8. **ΔSea Ice Cover (Fraction):** The anomaly in sea ice cover in fraction for ΔV-IO. The ΔV-FO run has no change in sea ice due to the fixed ocean boundary conditions.

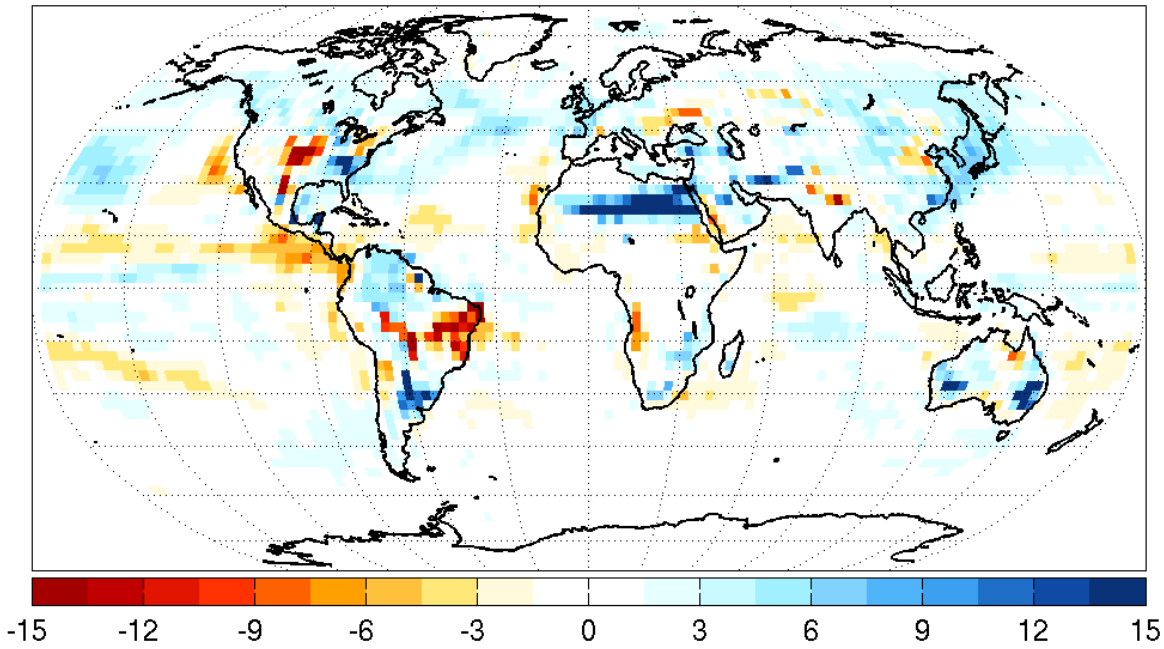

(a) ΔV-IO Total Latent Heat Flux (Wm^{-2})

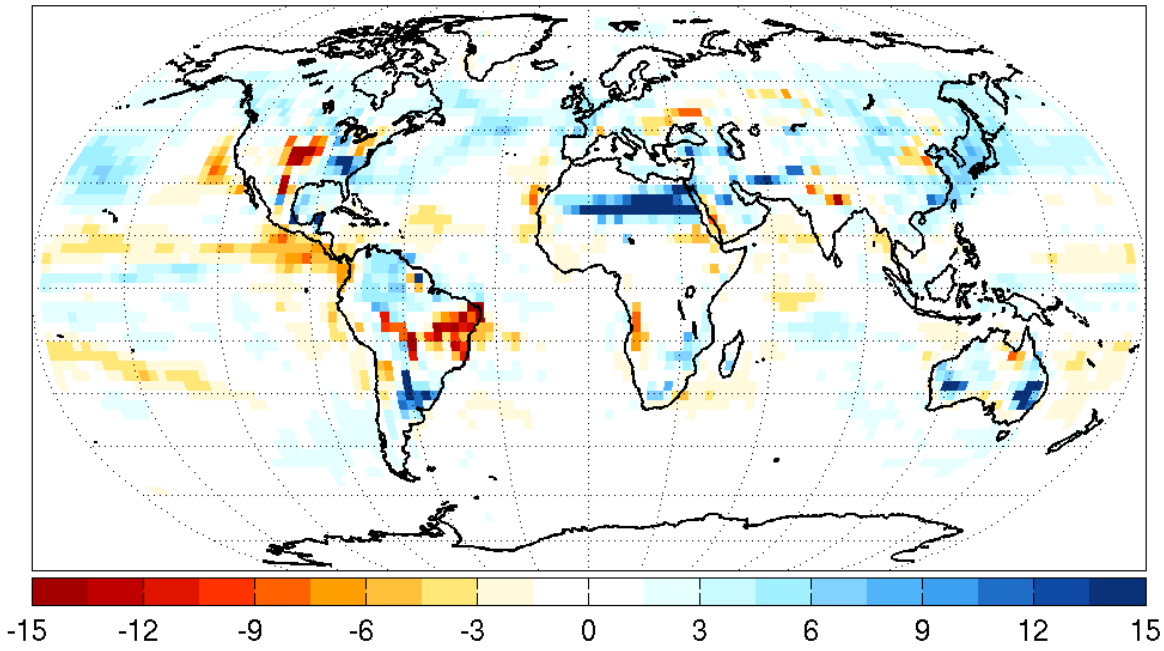

(b) ΔV-FO Total Latent Heat Flux (Wm^{-2})

Figure 4.9. **ΔLatent Heat Flux (Wm^{-2}):** The same as Figure 4.2 for Δtotal surface latent heat flux over both land and ocean in units of Wm^{-2}.

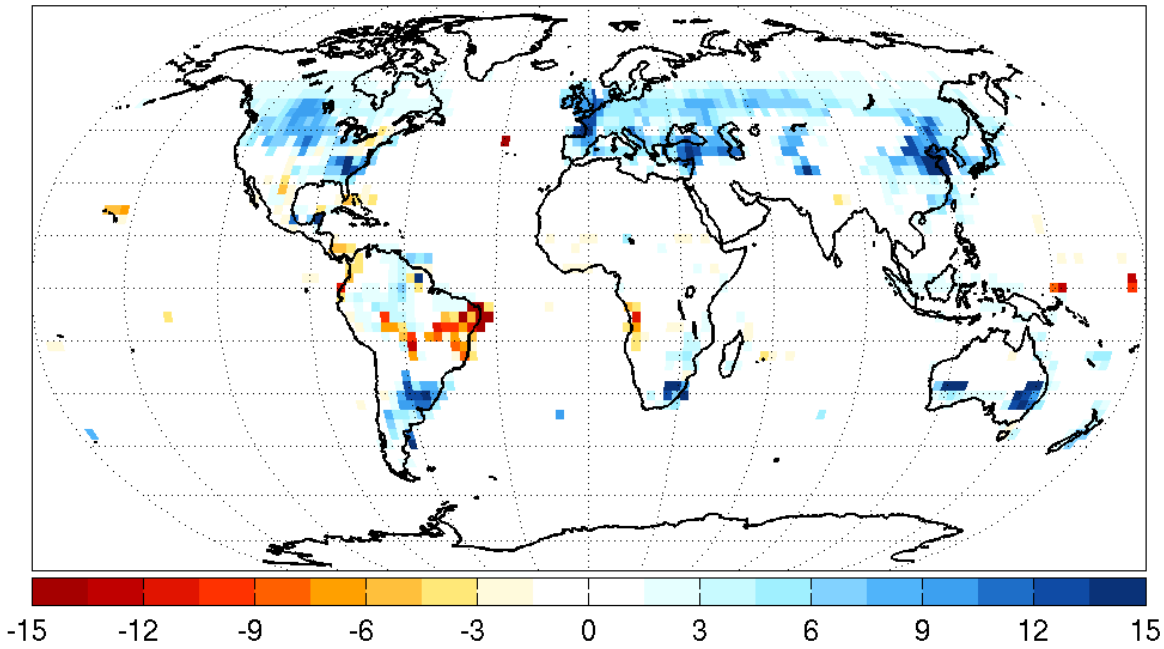

(a) ΔV-IO Transpirtion Flux (Wm^{-2})

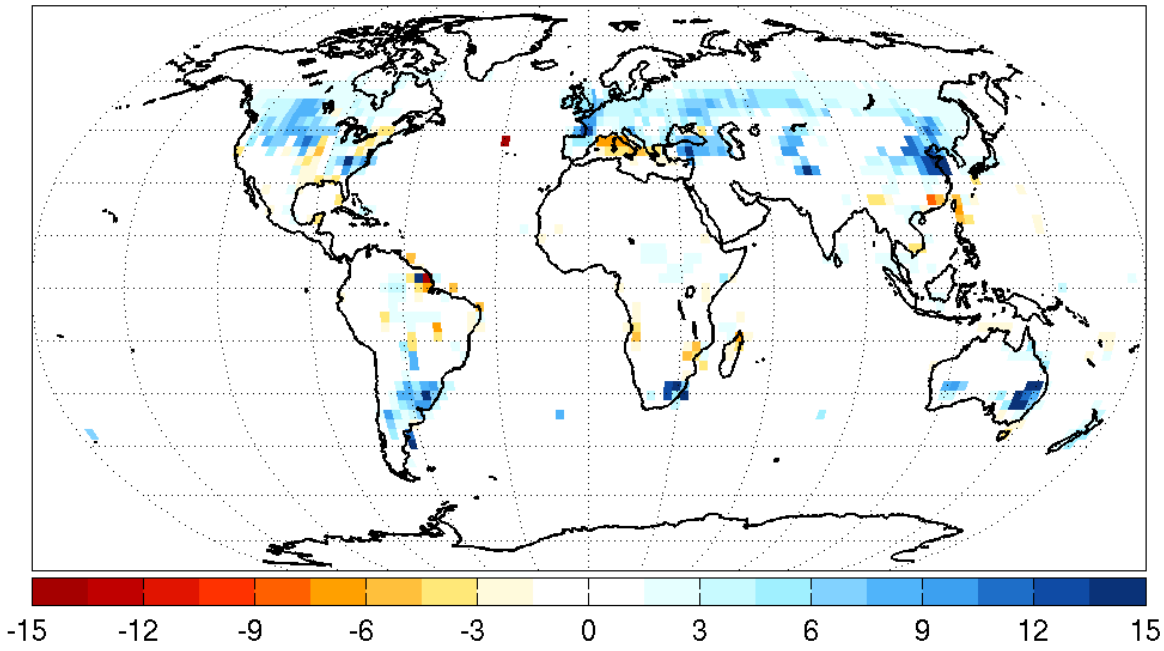

(b) ΔV-FO Transpiration Flux (Wm^{-2})

Figure 4.10. **ΔTranspiration Flux (Wm^{-2}):** The same as Figure 4.2 for Δ transpiration flux in units of Wm^{-2}.

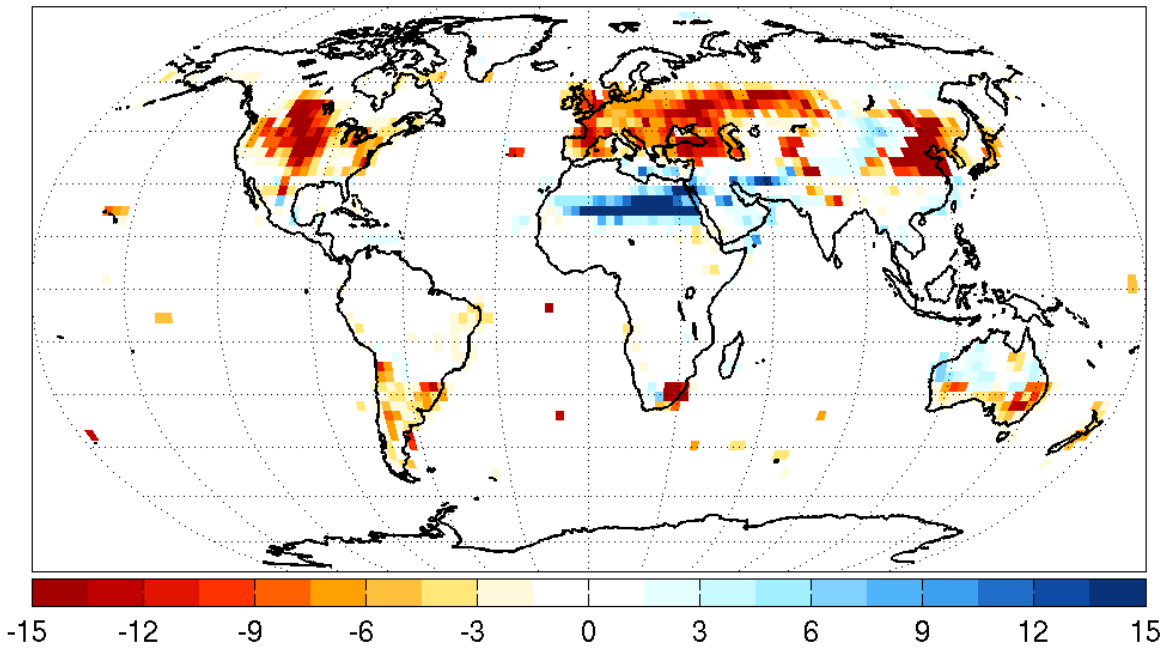

(a) ΔV-IO Ground Evaporation Flux (Wm^{-2})

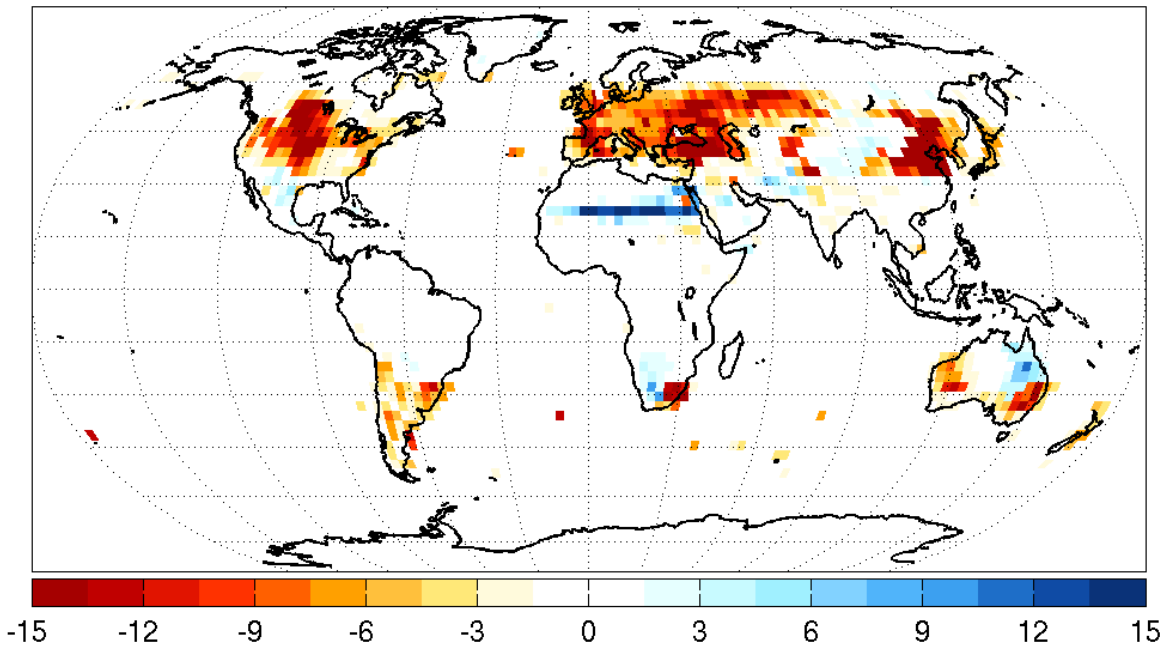

(b) ΔV-FO Ground Evaporation Flux (Wm^{-2})

Figure 4.11. **ΔGround Evaporation Flux (Wm^{-2}):** The same as Figure 4.2 for Δ ground evaporation flux in units of Wm^{-2}.

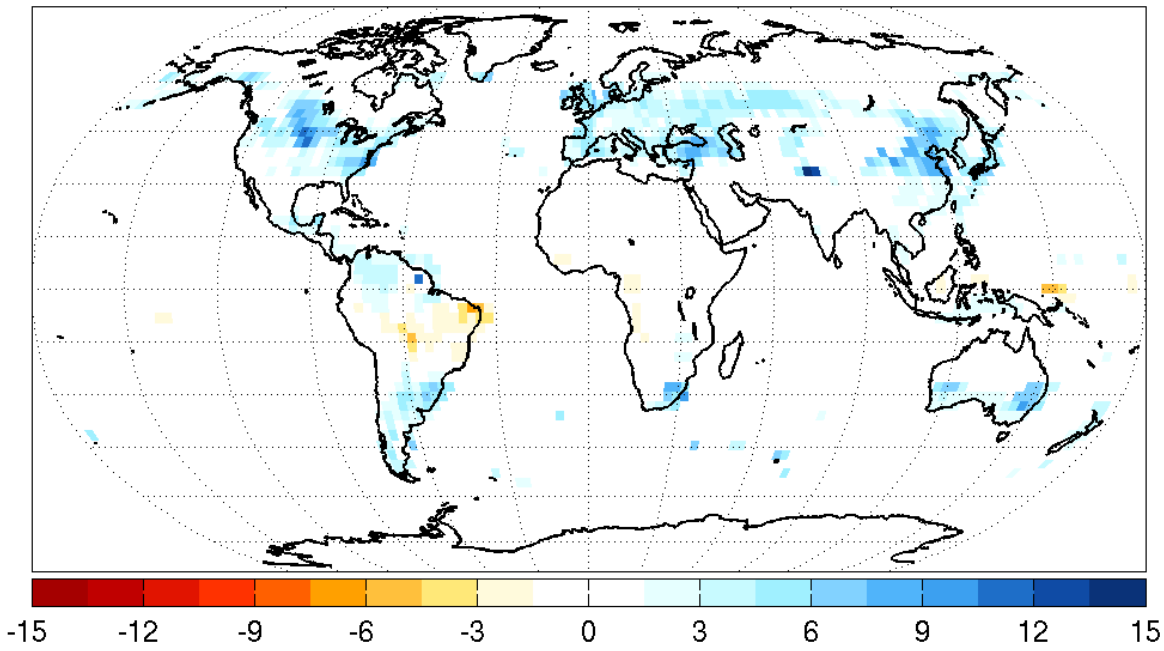

(a) ΔV-IO Canopy Evaporation Flux (Wm^{-2})

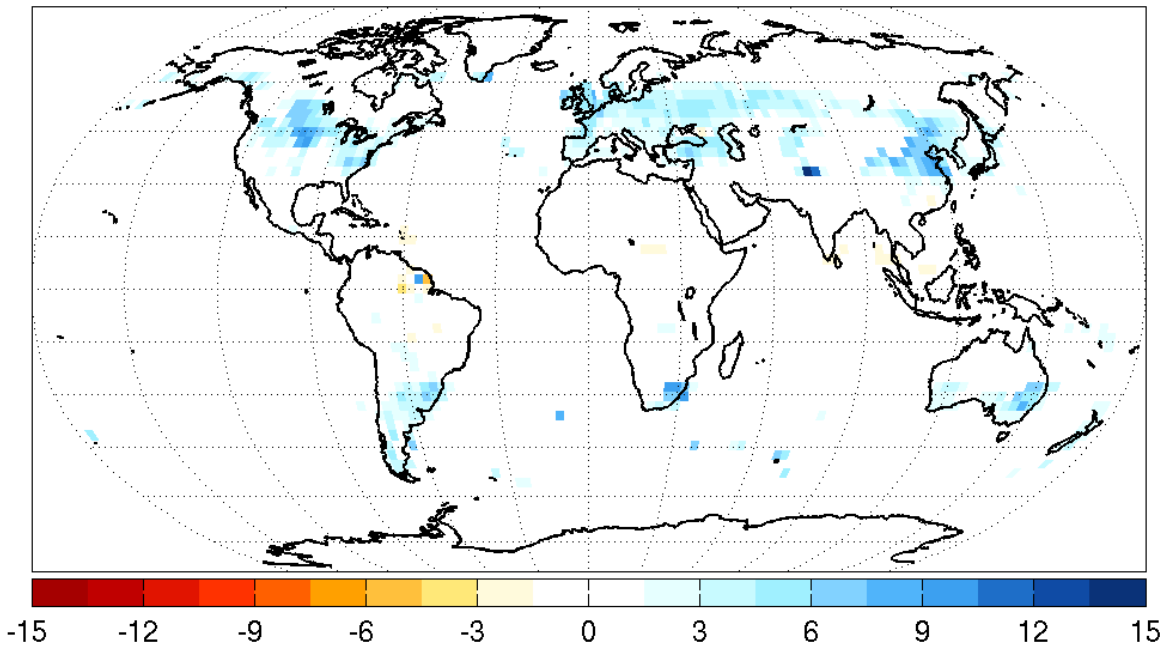

(b) ΔV-FO Canopy Evaporation Flux (Wm^{-2})

Figure 4.12. **ΔCanopy Evaporation Flux (Wm^{-2}):** The same as Figure 4.2 for Δ canopy evaporation flux in units of Wm^{-2}.

as leaf area index; LAI). The spatial maps of ΔLAI (Figure 4.15), new vegetation area (Figure 4.1), and Δground evaporation (Figure 4.11) match in some regions, such as Europe and the Mediterranean, but do not match well in others such as central North America. In a few regions, the ΔLAI actually decreases with the addition of trees, meaning that the trees in our experiment are not able to support as many leaves as the grasses in the control run. One small region of ΔLAI decrease is just south of the great lakes in the United States. The drop in LAI is not explained by water limitation as soil moisture in that region increases or stays constant (Figure 4.16).

Transpiration does not uniformly increase after the conversion from grass to trees. ΔLAI is not larger everywhere with the addition of trees. Observations of maximum canopy conductance over various plant types indicate that grasses and deciduous trees may not have substantially different conductance values when water and light are not limiting [*Kelliher et al.*, 1995]. Although counter-intuitive, the lack of a uniform increase in transpiration with the conversion from grass to trees is perhaps not unexpected.

In contrast to the northern hemisphere, the southern hemisphere cools (Figure 4.2, Table 4.2). Trees were also added in the southern hemisphere mid latitudes, but unlike the northern hemisphere, productivity and transpiration increase uniformly with the shift from grass to trees. In this case the increase in transpiration is not balanced by a decrease in ground evaporation leading to a net latent heat flux from the surface to the atmosphere (Figures 4.10, 4.11, 4.9). The area of converted land is far less in the southern hemisphere, and the local cooling from latent heat flux overpowers any warming associated with a decrease in albedo. Interestingly, the cooler and wetter conditions are associated with an increase in productivity (Figure 4.23)

4.5.3 Changes in General Circulation

The ITCZ shifts northward with the addition of trees as is evident in the map of Δprecipitation (Figure 4.5). The shift is global, and regionally quite large (i.e. the East Pacific). The location of the peak in the ITCZ is calculated following Equtation 4 from *Lintner et al.* [2004] as the precipitation maximum weighted latitude

$$ITCZ(t) = \frac{\int_{\phi_1}^{\phi_2} \lambda_{max}(\phi,t) ppt_{max}(\phi,t) d\phi}{\int_{\phi_1}^{\phi_2} ppt_{max}(\phi,t) d\phi} \tag{4.1}$$

where ppt_{max} represents the maximum precipitation between 15° north and south, λ_{max} represents the latitude of the occurrence of maximum precipitation, and ϕ represents longitude. The movement of the peak of the ITCZ is on the order of 1° in most locations and up to 6° in the East Pacific region. The global average climatological ITCZ location is plotted in Figure 4.17. Over Africa (20°W to 30°E), the peak ITCZ location reaches its maximum northward extent at 10 $^{\circ}N$ in the C-IO and about 11 $^{\circ}N$ in V-IO (Figure 4.18).

The main increase in precipitation associated with the addition of mid latitude trees

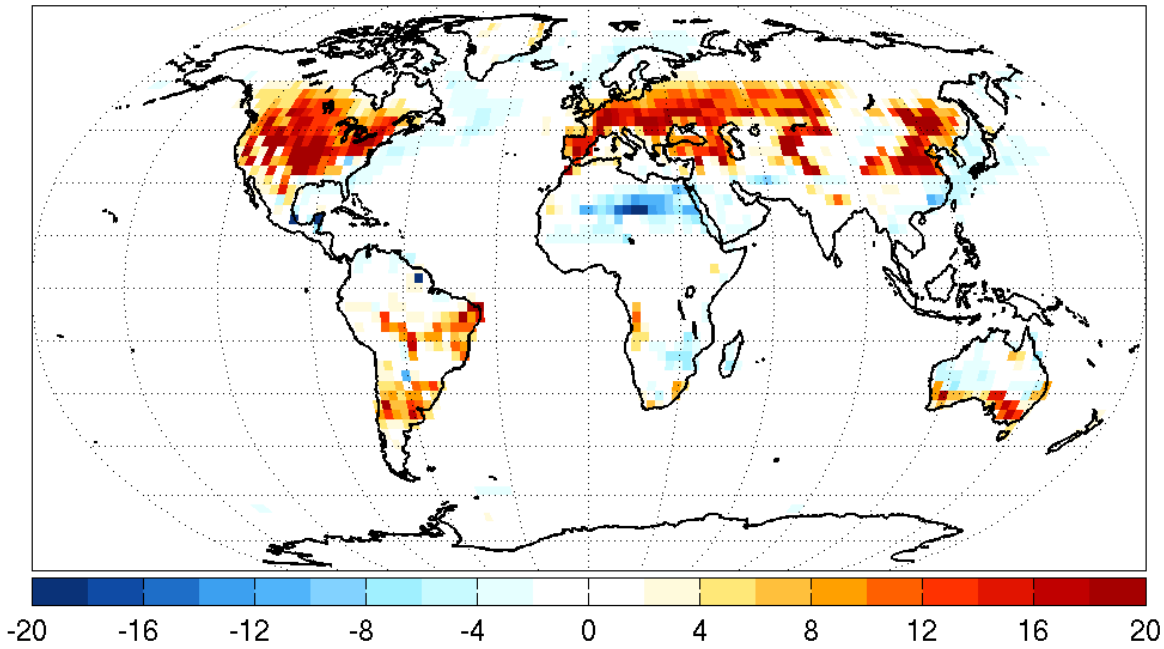

(a) ΔV-IO Sensible Heat Flux (Wm^{-2})

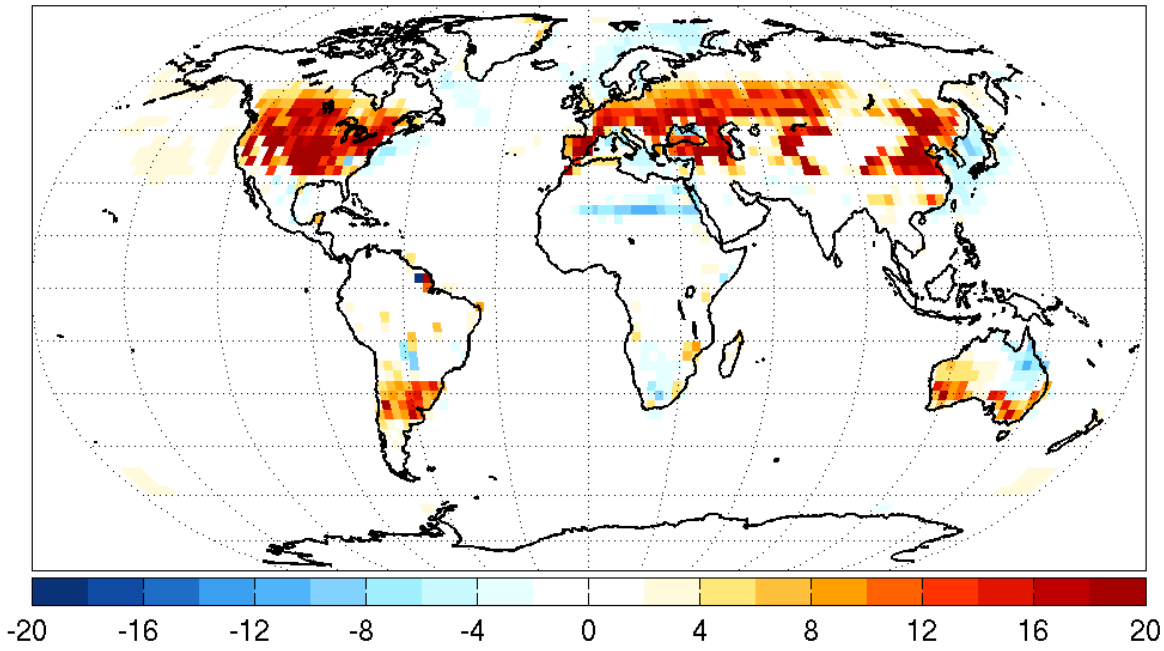

(b) ΔV-FO Sensible Heat Flux (Wm^{-2})

Figure 4.13. **ΔSensible Heat Fluxes (Wm^{-2}):** The same as Figure 4.2 for Δ sensible heat flux in units of Wm^{-2}.

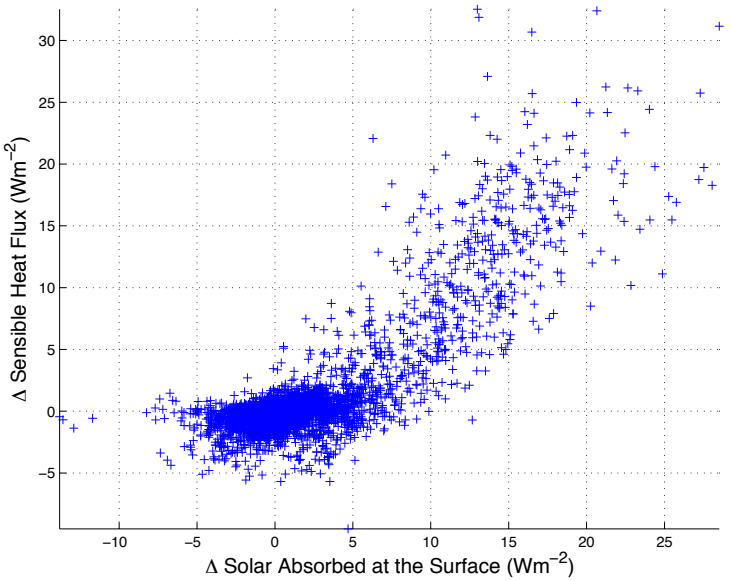

(a) ΔV-IO Absorbed Solar vs. Sensible Heat Flux

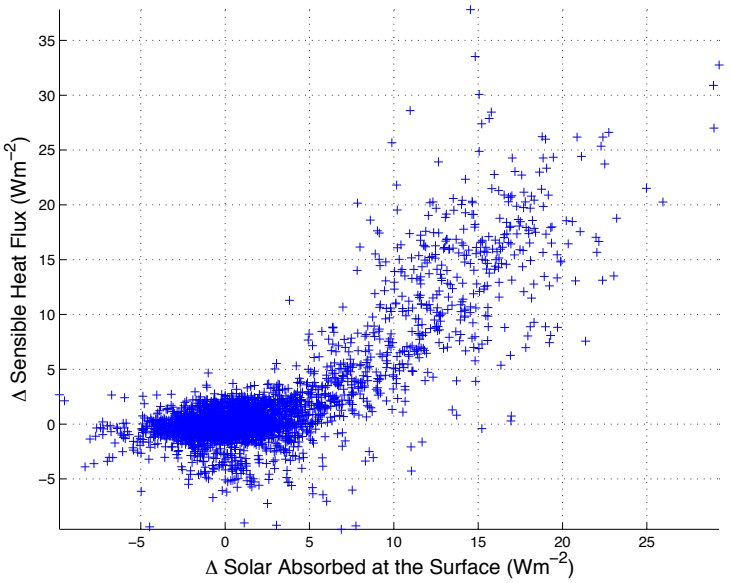

(b) ΔV-FO Absorbed Solar vs. Sensible Heat Flux

Figure 4.14. **ΔSensible Heat Flux vs. ΔAbsorbed Solar Radiation:** The anomaly in Δ absorbed solar radiation at the surface (due to the change in albedo) plotted against Δ sensible heat flux both in Wm^{-2} for **(a)** ΔV-IO and **(d)** ΔV-FO.

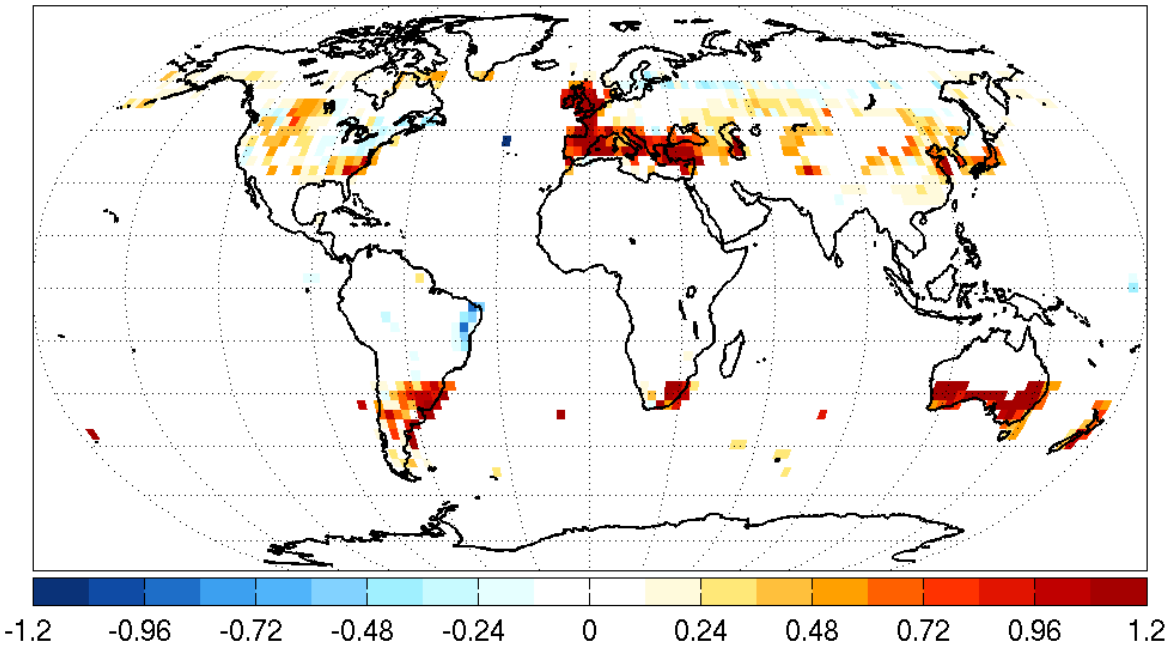

(a) ΔV-IO Leaf Area Index (m^2m^{-2})

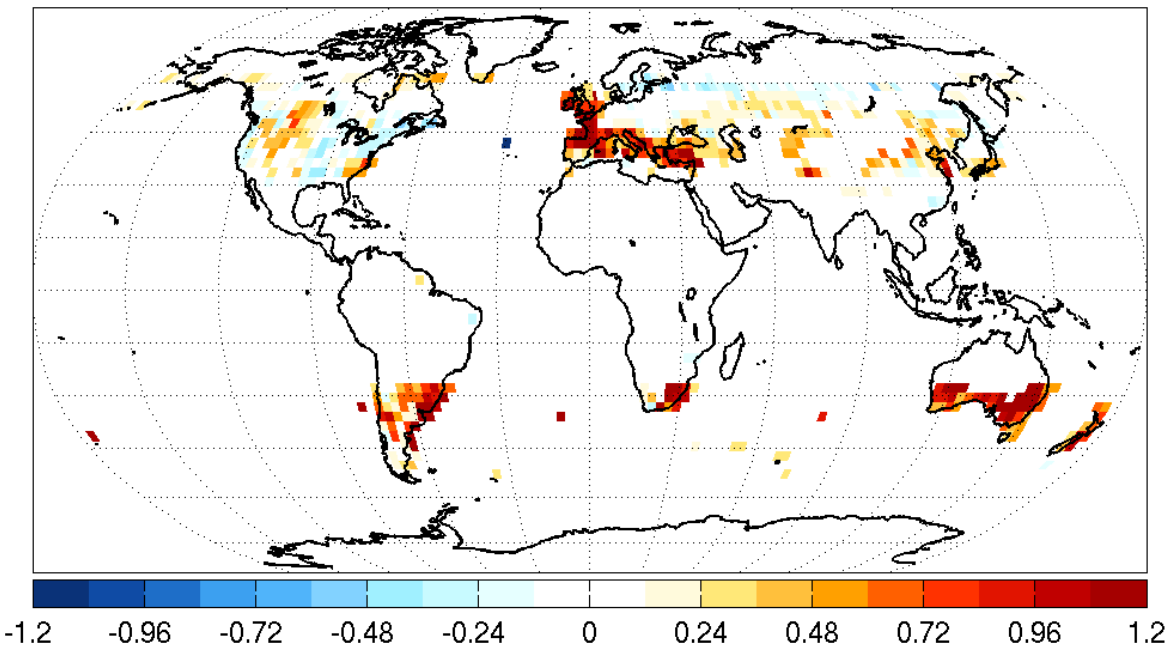

(b) ΔV-FO Leaf Area Index (m^2m^{-2})

Figure 4.15. **ΔLeaf Area Index (m^2m^{-2}):** The same as Figure 4.2 for Δ leaf area index in units of m^2m^{-2}.

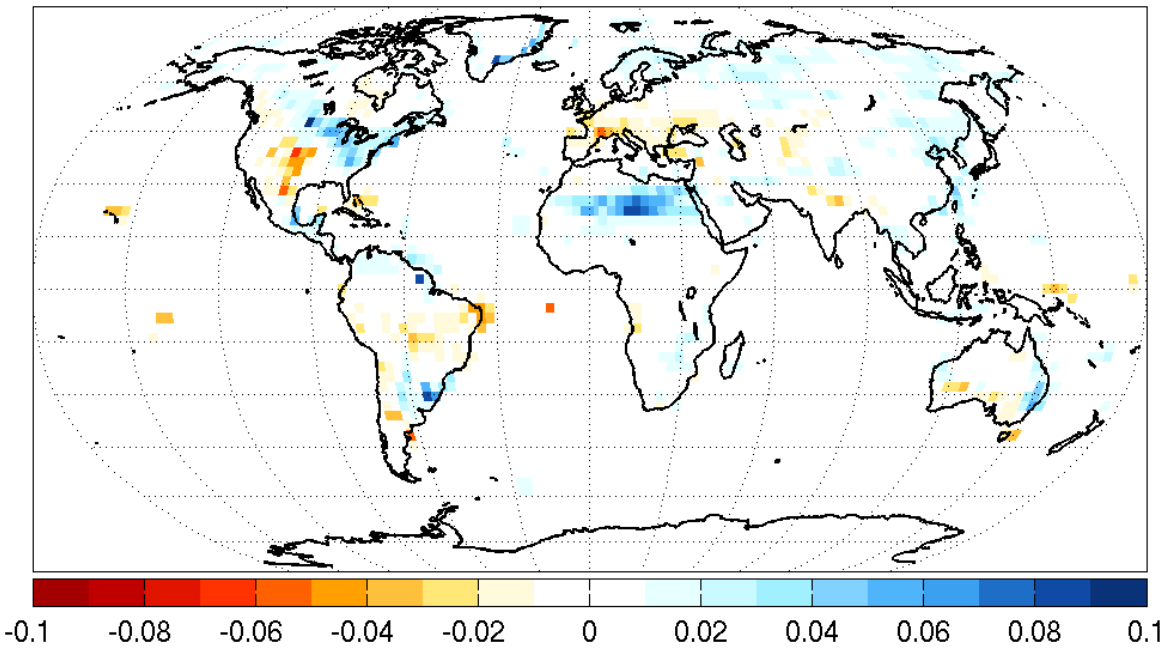

(a) ΔV-IO Volumetric Soil Moisture (m^3m^{-3})

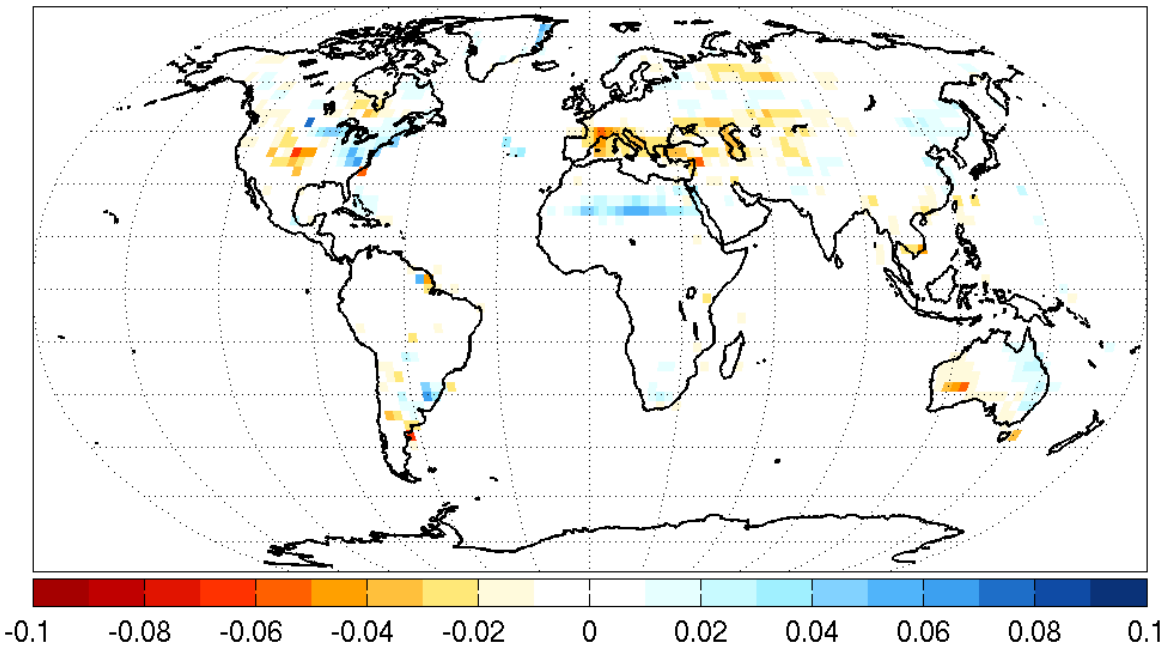

(b) ΔV-FO Volumetric Soil Moisture (m^3m^{-3})

Figure 4.16. **ΔVolumetric Soil Moisture (m^3m^{-3}):** The same as Figure 4.2 for Δ soil moisture averaged in the top 30 cm of soil in units of m^3m^{-3}.

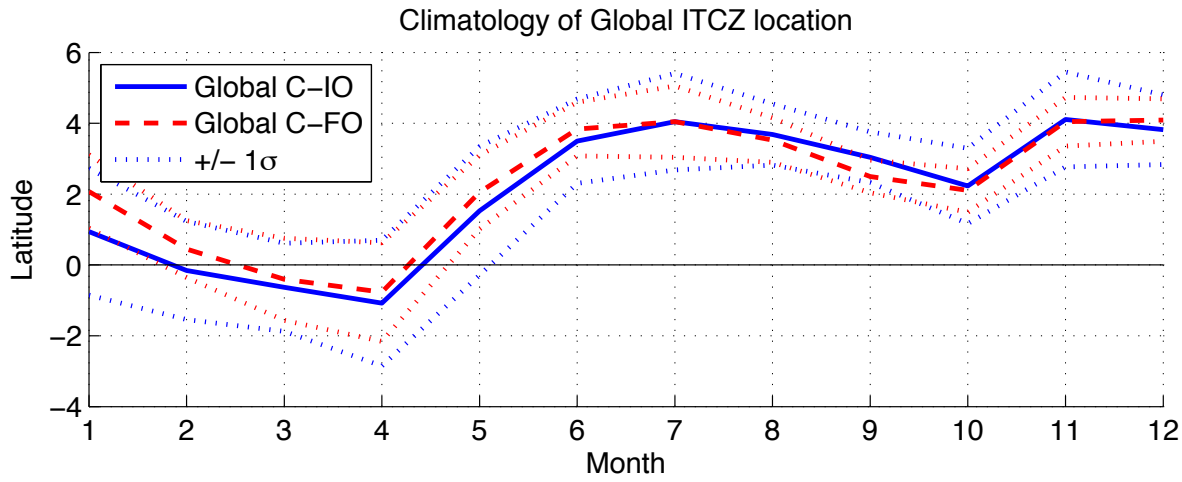

(a) Global ITCZ Location

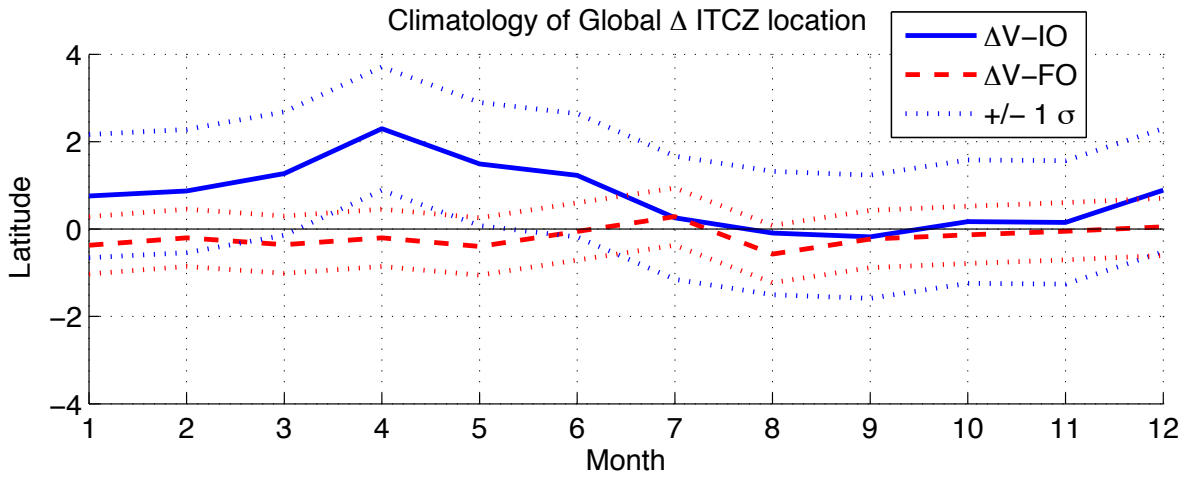

(b) Anomalous Global ITCZ Location

Figure 4.17. **Climatology of Global ITCZ location:** Climatology of the Globally averaged ITCZ as defined by Equation 4.1 is shown for **(a)** C-IO (blue) and C-FO (red) and **(b)** ΔV-IO (blue) and ΔV-FO (red). The +/- 1 σ error bars are shown as dotted lines.

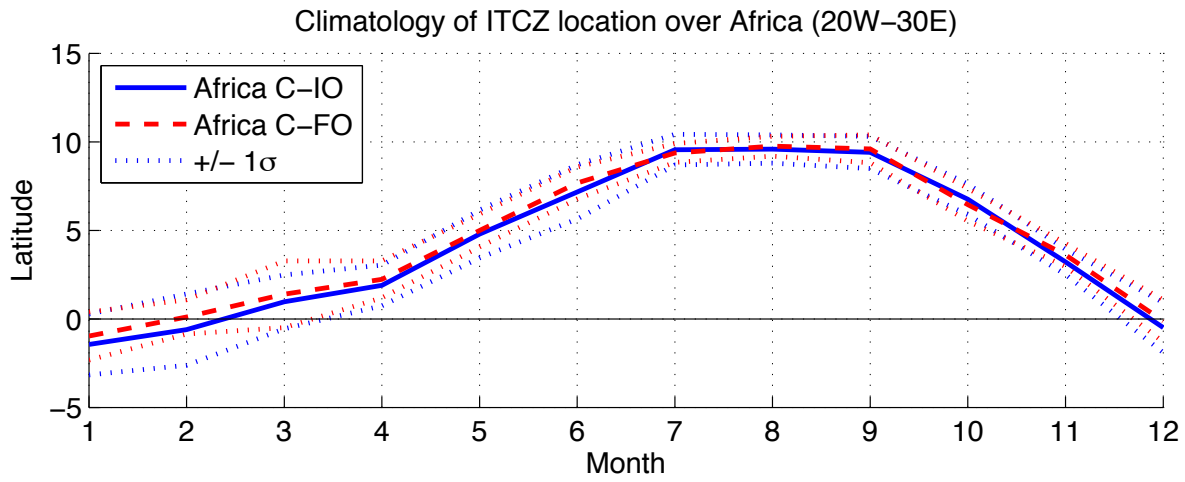

(a) ITCZ Location over Africa

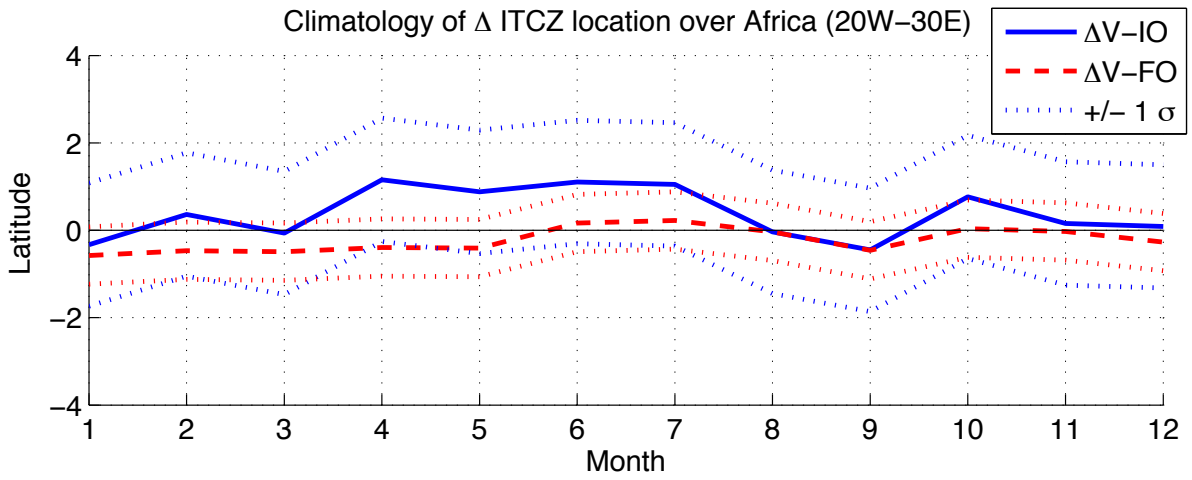

(b) Anomalous ITCZ Location over Africa

Figure 4.18. **ITCZ Location over Africa (20°W to 30°E):** Climatology of the ITCZ location over Africa (20°W to 30°E) as defined by Equation 4.1 is shown for **(a)** C-IO (blue) and C-FO (red) and **(b)** ΔV-IO (blue) and ΔV-FO (red). The +/- 1 σ error bars are shown as dotted lines.

occurs north of about 18 $^{\circ}N$ and cannot be explained by shifts on order of 1° from the peak ITCZ location of $\sim$10 $^{\circ}N$ (Figures 4.4, 4.18). To understand the changes in this northern region of Africa we need to look at the northern edge of the ITCZ rather than its central location. Following *Braconnot et al.* [2007b], we calculate the northern weighted ITCZ location, ITCZ_N, which calculates the precipitation weighted latitude north of the precipitation maximum. We use Equation 1 from *Braconnot et al.* [2007b]

$$ITCZ_N(lon) = \frac{\Sigma_{y=lat(prmax)}^{30\,\mathrm{deg}\,N} pr(y)lat(y)}{\Sigma_{y=lat(prmax)}^{30\,\mathrm{deg}\,N} pr(y)} \tag{4.2}$$

with the additional assumption that the precipitation maximum referred to occurs between 15° North and South (as is consistent with *Lintner et al.* [2004]). Using this northern location of the ITCZ, the climatological $ITCZ_N$ reaches 15° North in C-IO and 17° North in ΔV-IO (Figure 4.19). Taking into account the variance in $ITCZ_N$ (represented by the dotted lines in Figure 4.19) our results show that at times the $ITCZ_N$ reaches sufficiently far north as to push precipitation into the Sahara.

In addition to changes in the location of the ITCZ, we see changes in the strength of circulation associated with an increase in mid latitude vegetation. The anomaly in vertical velocity ($\Delta\omega$, Figure 4.20) shows downward anomalies in the core of the initial ITCZ location as well as upward anomalies in the location of the initial descending branch of the Hadley cell. This could be interpreted as a shift in the ITCZ (as it likely is over the eastern Pacific ocean) but could also indicate a decrease in the strength of the Hadley cell in the northern hemisphere. In fact, over Africa (20°W-30°E) the vertical velocity in the downwelling branch of the Hadley cell decreases in strength (Figure 4.21). This decrease in downwelling would likely be sufficient to allow for limited precipitation over the Sahara and Sahel region as shown by Figure 4.4. In the fixed ocean experiments, precipitation over Africa still increases (Figure 4.4) while the location of the $ITCZ_N$ does not change (Figure 4.18). Changes in vertical velocity are, however, consistent with the idea that decreases in the downwelling branch could allow for increases in precipitation (Figure 4.21).

As the ascending branch of the Hadley cell moves northwards towards the warmer and darker hemisphere and possibly also decelerates, precipitation reaches into the treeless Sahara region. Teasing apart the influence of the location of the ITCZ and the strength of circulation is difficult. In our experiments the primary forcing on climate is through the additional solar radiation absorbed by the surface due to the darkening associated with the expansion of trees in the mid latitudes. Previous studies have shown that large-scale changes in planetary albedo have the ability to modify general circulation. *Chiang and Bitz* [2005] show that glaciation in the Northern Hemisphere as in the Last Glacial Maximum causes the ITCZ to move southward—consistent with idea that the ITCZ moves towards the warmer hemisphere. Their hypothesis holds that the decrease in absorbed solar radiation in the Northern Hemisphere requires a greater transport of energy from South to North. A simplified mixed layer ocean has, by definition, fixed heat fluxes resulting in the atmosphere transporting all of the additional energy. In order to do so, the winter cell of the Hadley circulation moves towards the warmer hemisphere resulting in a shift of the ITCZ.

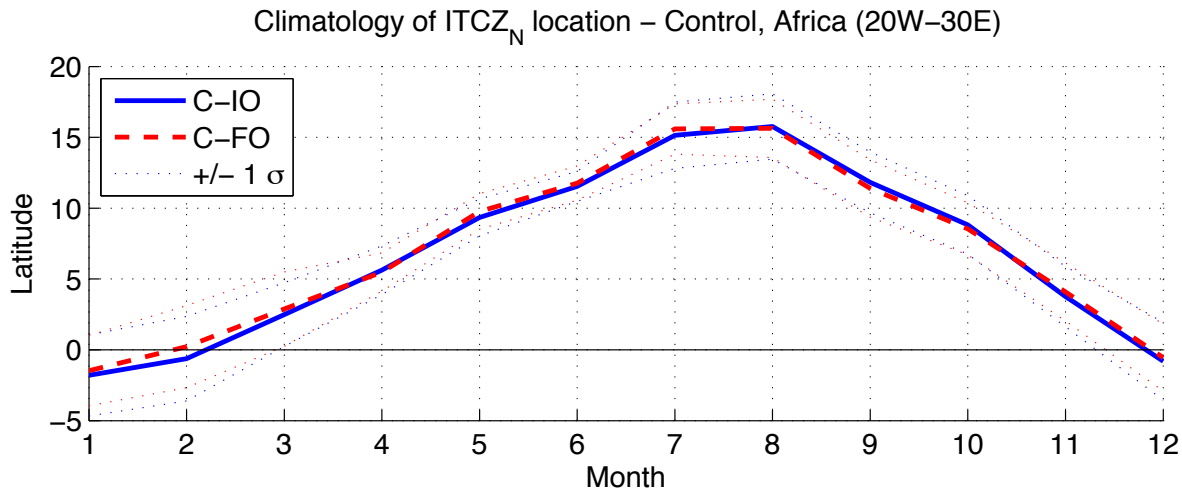

(a) ITCZ$_N$ Location over Africa

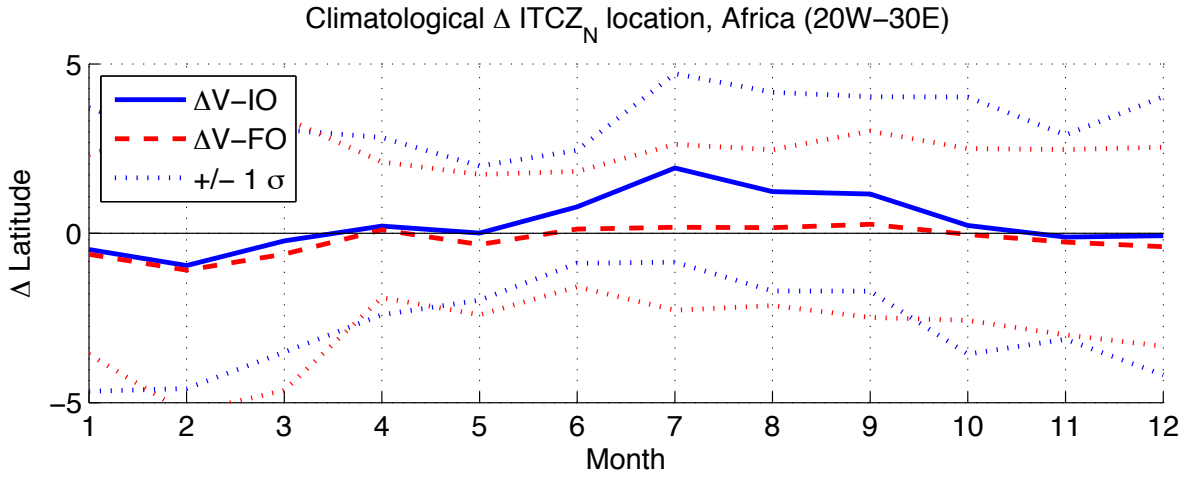

(b) Anomalous ITCZ$_N$ Location over Africa

Figure 4.19. **ITCZ$_N$ over Africa (20°W to 30°E):** Climatology of the northern weighted ITCZ location, $ITCZ_N$, over Africa (20°W to 30°E) as defined by Equation 4.2 is shown for **(a)** C-IO (blue) and C-FO (red) and **(b)** ΔV-IO (blue) and ΔV-FO (red). The +/- 1 σ error bars are shown as dotted lines.

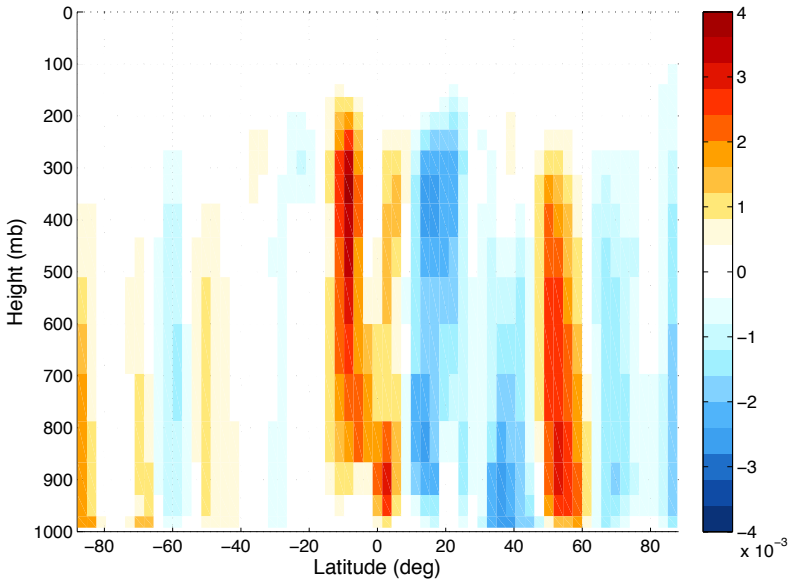

(a) ΔV-IO ω (m/s)

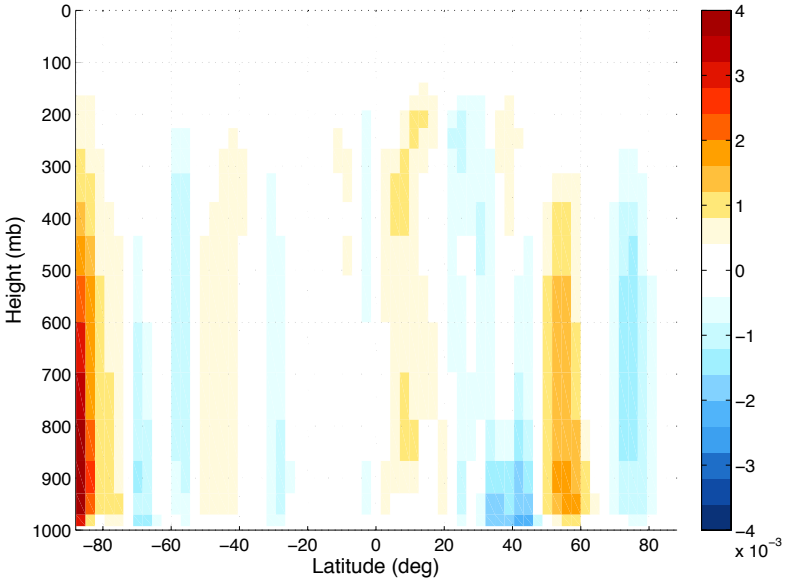

(b) ΔV-FO ω (m/s)

Figure 4.20. **ΔZonal Mean Vertical Velocity (m/s):** The anomaly in annual mean zonally averaged vertical velocity (ω) in units of m/s for **(a)** ΔV-IO and **(b)** ΔV-FO. $\Delta\omega$ is plotted with latitude on the x axis and pressure in mb on the y axis. Positive values indicate downward anomalies in vertical velocity and negative values represent upward anomalies in vertical velocity.

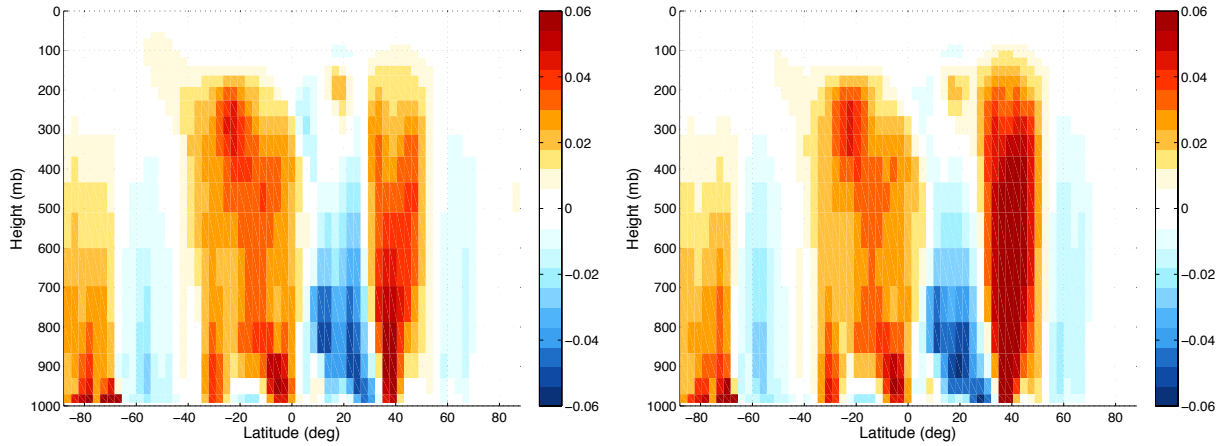

(a) C-IO Zonal Mean Vertical Velocity over Africa(m/s)

(b) V-FO Zonal Mean Vertical Velocity over Africa (m/s)

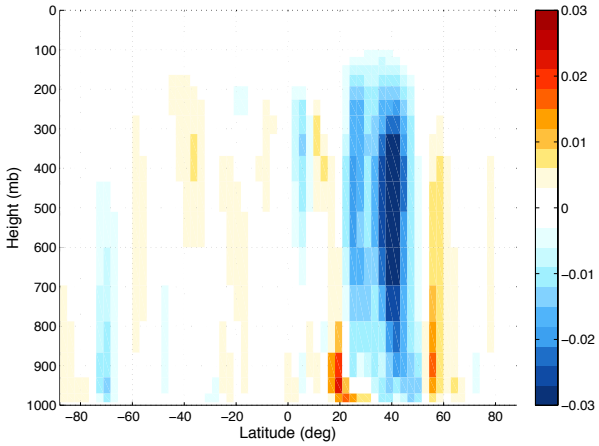

(c) ΔV-FO Zonal Mean Vertical Velocity over Africa (m/s)

Figure 4.21. **Zonally Averaged Vertical Velocity over Africa (20°W to 30°E):** The zonally averaged vertical velocity (ω) over Africa (20°W to 30°E) in units of m/s for **(a)** C-IO, **(b)** V-IO and **(c)** ΔV-IO. ω and $\Delta\omega$ are plotted with latitude on the x axis and pressure in mb on the y axis. Positive values indicate downward anomalies in vertical velocity and negative values represent upward anomalies in vertical velocity.

We suggest that the hypothesis of *Chiang and Bitz* [2005] holds in this experiment as well. We further propose that, in this context, the ITCZ is following the "center of energy" of the atmosphere-ocean system and that this center can be quantified by examining the energy budget of the two hemispheres (e.g. *Kang et al.* [2008]). We calculate the Thermal Ratio (TR) as the ratio between mean annual Northern and Southern Hemisphere temperature as

$$TR = \frac{\overline{T_{NH}}}{\overline{T_{SH}}} \tag{4.3}$$

where values above 1 indicate that the center of energy is in the Northern Hemisphere and values below 1 indicate that it is in the Southern Hemisphere. The climatology of the TR as well as the climatology of ΔTR are shown in Figure 4.22. The seasonal cycle of the TR indicates that the center of energy is in the Northern Hemisphere more than half of the year crossing northward in April and southward in late October. This is consistent with the placement of the ITCZ in the North more than half of the year (e.g. Figure 4.17). The ΔTR shows that with the addition of trees in the mid latitudes, the center of energy moves northward in all months in V-IO and most months in V-FO. This is consistent with our observation of the movement of the ITCZ northward (Figures 4.5, 4.17) and supports the hypothesis of *Chiang and Bitz* [2005].

4.5.4 Carbon Cycle Balance

The addition of trees in mid latitudes effects the local carbon balance by increasing productivity and, in response to widespread increases in temperature, increasing heterotrophic decomposition (Figures 4.23, 4.24). In addition to changes to the local carbon balance, the addition of mid latitude trees modifies the distribution of precipitation across the globe and thus influences remote carbon cycling as well. Over Africa, the increase in precipitation over the Sahara and upper Sahel regions does not result in an increase in productivity as no plants are assigned to grow there in the model. The water is instead released directly as ground evaporation, and no change in the carbon balance is observed (Figure 4.11). Over the South America, the ITCZ also shifts northward, decreasing precipitation over the Amazon forest causing a decrease in productivity (Figures 4.23, 4.5). The soil respiration also decreases, but total soil respiration rates are one order of magnitude smaller than carbon uptake rates by NPP so the net balance is a loss of carbon to the atmosphere. In our model experiments, extratropical changes in vegetation distribution are able to effect tropical carbon cycling in addition to global circulation.

4.6 Conclusions and Implications for 6Kya

An expansion of mid latitude forests creates a darker, warmer northern hemisphere. The increase in absorbed solar radiation associated with expanded tree cover is released from the

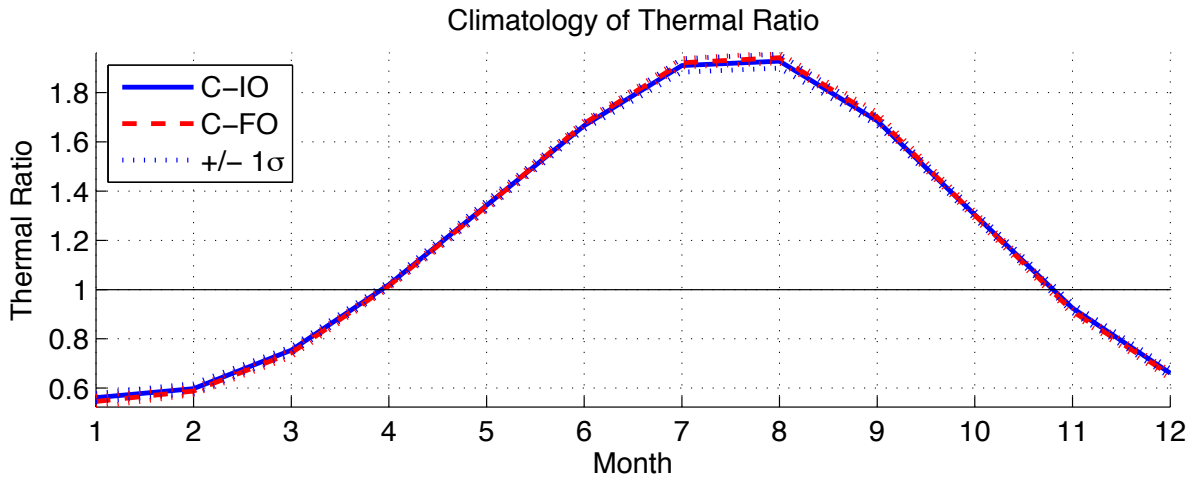

(a) Thermal Ratio

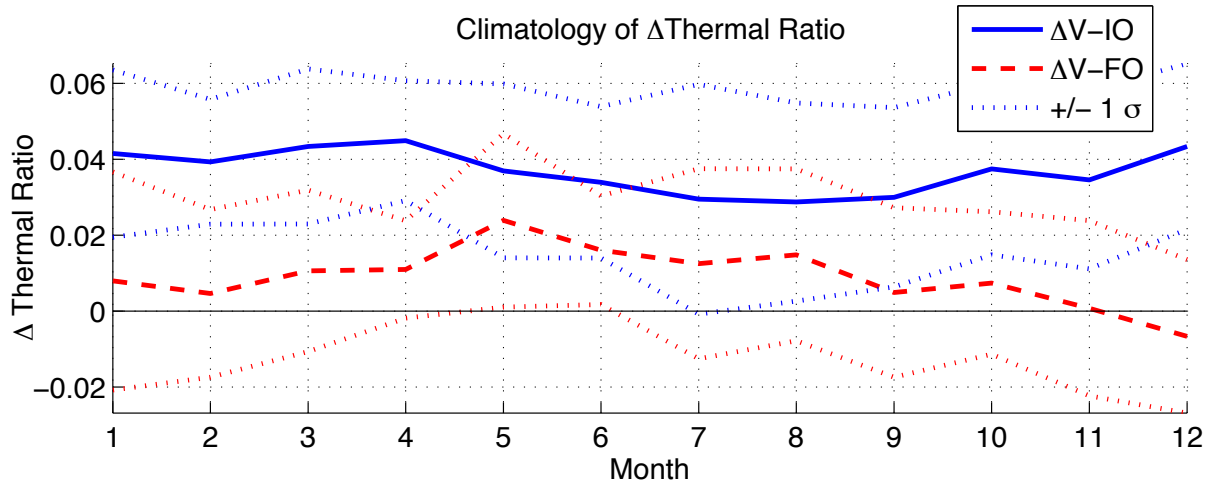

(b) ΔThermal Ratio

Figure 4.22. **Thermal Ratio:** Climatology of the Thermal Ratio, TR, as defined by Equation 4.3 is shown for **(a)** total TR and **(b)** ΔTR. The +/- 1 σ error bars are shown as dotted lines. The TR is calculated as the ratio between average Northern Hemisphere and Southern Hemisphere surface temperatures and represents the location of the center of energy relative to the equator.

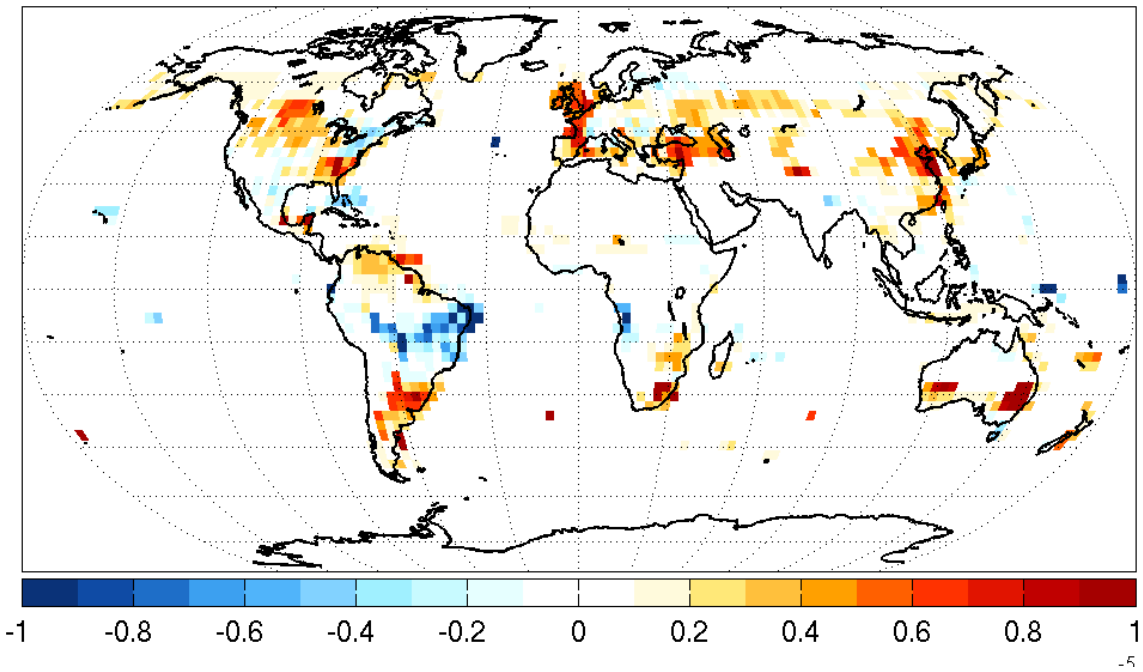

(a) ΔV-IO Net Primary Production ($gCm^{-2}s^{-1}$)

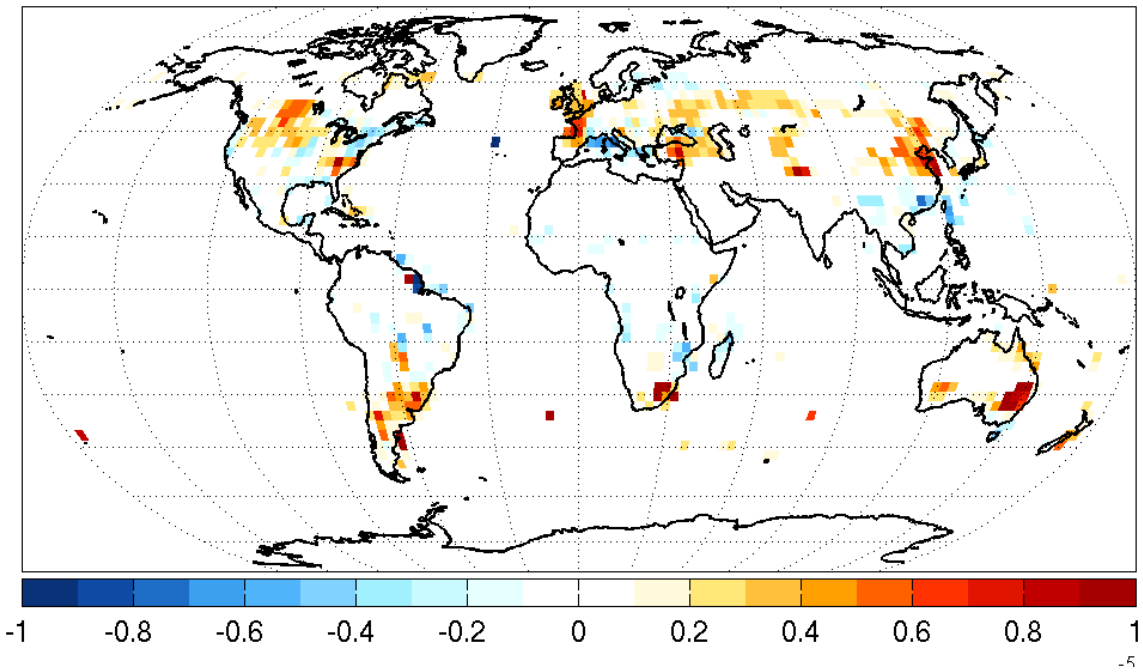

(b) ΔV-FO Net Primary Production ($gCm^{-2}s^{-1}$)

Figure 4.23. **ΔNet Primary Production ($gCm^{-2}s^{-1}$):** The same as Figure 4.2 for Δ net primary production in units of $gCm^{-2}s^{-1}$.

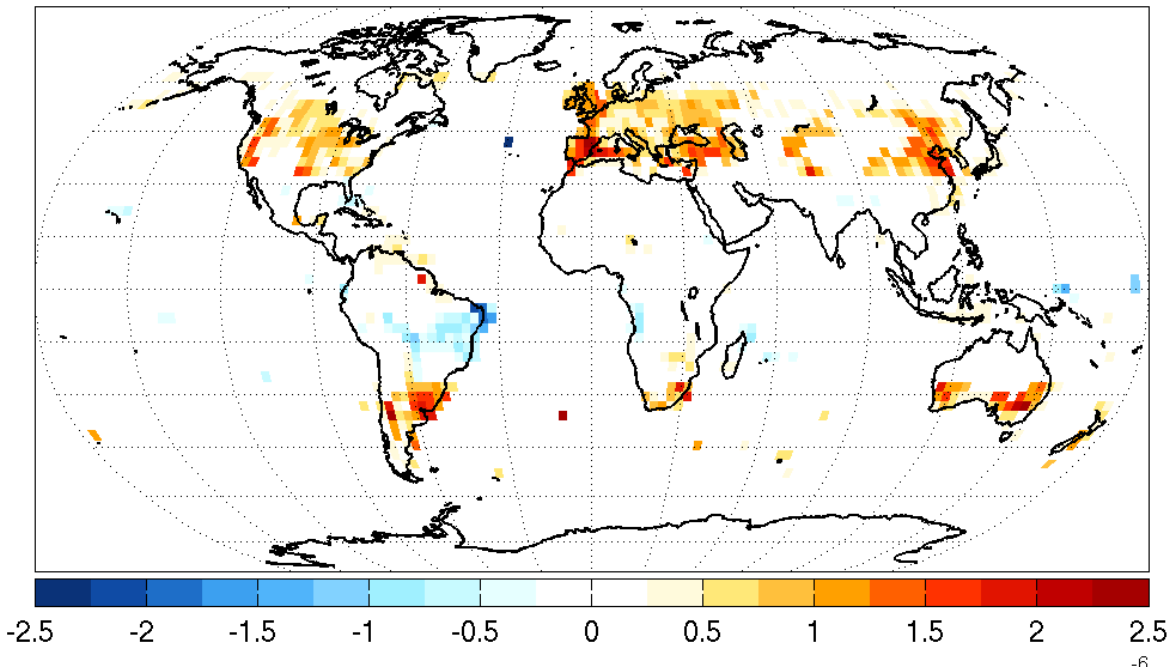

(a) ΔV-IO Soil Respiration ($gCm^{-2}s^{-1}$)

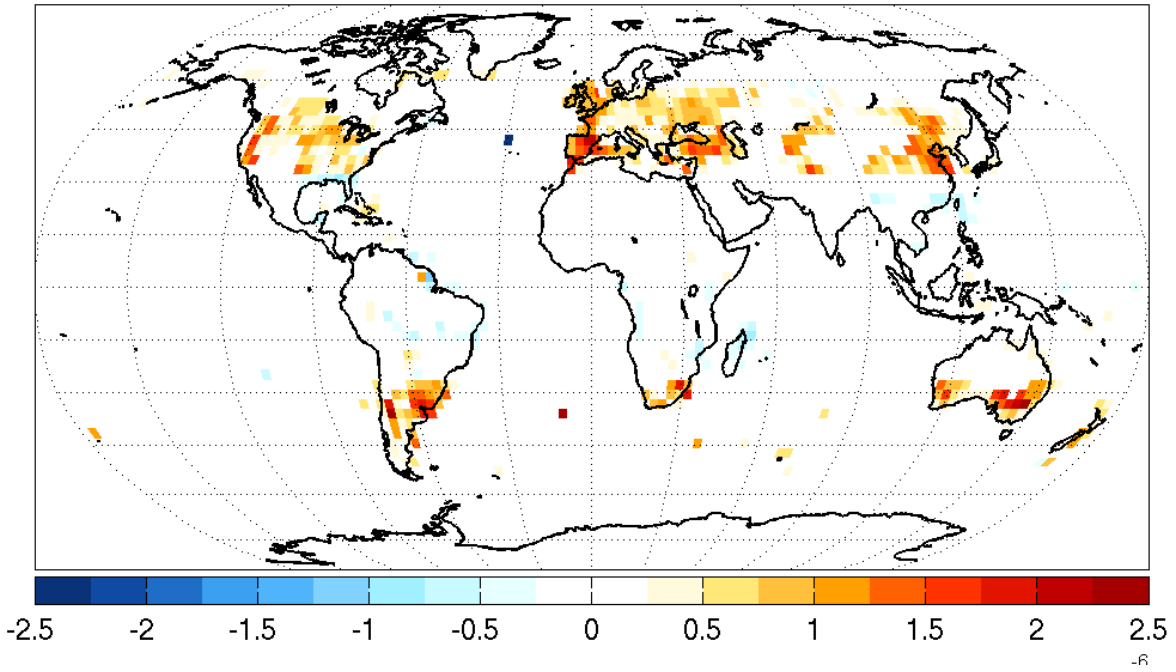

(b) ΔV-FO Soil Respiration ($gCm^{-2}s^{-1}$)

Figure 4.24. **ΔSoil Respiration ($gCm^{-2}s^{-1}$):** The same as Figure 4.2 for Δ soil respiration in units of $gCm^{-2}s^{-1}$.

surface as sensible heat flux as the latent heat fluxes are mostly balanced between increases in transpiration and decreases in ground evaporation. In response to the widespread warming, the Northern Hemisphere is required to transport more energy to the Southern Hemisphere to maintain energy balance. In order to transport this energy through the atmosphere, the winter cell of the Hadley circulation moves northward to increase southward transport, pushing the ITCZ North. Resulting changes in tropical precipitation decrease productivity in the Amazon and increase precipitation over Africa. Our results suggest that remote forcing of tropical precipitation by mid latitude vegetation increases precipitation rates over north Africa and decreases precipitation rates, and thus productivity, over the Amazon forest.

Our work suggests the following hypothesis: mid latitude changes in tree cover are partially responsible for the tropical shifts in precipitation observed in the Mid Holocene. The remote effects of mid latitude vegetation are unlikely to be the sole cause of changes in Mid Holocene vegetation, but they could help initiate the growth of local vegetation and force precipitation to be higher than local changes in vegetation and albedo can support. Mid latitude tree cover has changed substantially in the last 6000 years, particularly in Europe, and our work suggests that these changes in vegetation cover could force changes in circulation and tropical precipitation. The idea of mid latitude vegetation playing a role in Mid Holocene precipitation over Africa has not been suggested previously and although our work suggests that the mechanism is plausible, we have not directly tested this hypothesis. We plan to run simulations to test the hypothesis more directly in future work.

Chapter 5

Sensitivity of Climate to Changes in Arctic Vegetation

5.1 Abstract

Arctic climate is projected to change dramatically in the next 100 years and increases in temperature will likely lead to changes in the distribution and makeup of the Arctic biosphere. A largely deciduous ecosystem has been suggested as a possible landscape for future Arctic vegetation and is seen in paleo-records of warm times in the past. Here we use a global climate model with an interactive terrestrial biosphere to investigate the effects of adding deciduous trees on bare ground at high northern latitudes. We find that the top-of-atmosphere radiative imbalance from enhanced transpiration (associated with the expanded forest cover) is up to 1.5 times larger than the forcing due to albedo change from the forest. Furthermore, the greenhouse warming by additional water vapor melts sea ice and triggers a positive feedback through changes in ocean albedo and evaporation. Land surface albedo change is considered to be the dominant mechanism by which trees directly modify climate at high-latitudes, but our findings suggest an additional mechanism through transpiration of water vapor and feedbacks from the ocean and sea ice.

5.2 Introduction

The range of high-latitude trees is expected to expand poleward with warming and, in fact, the northern tree line is moving northward now [*Lloyd*, 2005]. Changes in vegetation

cover are recognized to modify climate and the energy budget of the Earth through changes in albedo in high latitudes and evapotranspiration (ET) in the tropics [*Bonan*, 2008; *Fischlin et al.*, 2007]. In snow-covered regions, the springtime growth of leaves enhances solar absorption because surface albedo is reduced from that of snow ($\sim$0.8) towards that of leaves ($\sim$0.1). Leaves also play a hydrologic role, transpiring water from the soil to the atmosphere. Variations in albedo and transpiration rates between different types of vegetation will induce a climate response that may depend on vegetation type. It has been suggested that broadleaf deciduous trees may invade warming tundra more effectively than boreal evergreen trees [*Edwards et al.*, 2005] and, due to the higher rates of transpiration and a higher albedo of deciduous broadleaf trees compared to needle-leaf evergreen trees [*Liu et al.*, 2005], we expect that the climate response may be different.

Previous studies on the climatic effects of changes in the distribution of Arctic vegetation have focused primarily on the range expansion or contraction of evergreen needle-leaf trees [*Bonan et al.*, 1992; *Foley et al.*, 1994; *Levis et al.*, 1999; *Snyder et al.*, 2004; *Cook et al.*, 2008]. The dark color and low ET of evergreen needle-leaf trees leads to a dramatic change in albedo, and thus short-wave forcing, with the addition or removal of trees but little change in long-wave forcing [*Bonan et al.*, 1992; *Foley et al.*, 1994]. Deciduous broad-leaf trees in the Arctic have twice the albedo and 50-80% greater ET rates when leafed-out than their evergreen needle-leaf counterparts [*Chapin et al.*, 2000]. It has been suggested that a vegetation change from evergreen to deciduous (such as after a disturbance) will produce a surface cooling due to the increase in albedo and latent cooling [*Chapin et al.*, 2000; *Liu et al.*, 2005]. *Eugster et al.* [2000] acknowledge that ecosystem changes that increase ET could also increase atmospheric moisture content but they consider this important only as a consequence for cloudiness (with increased moisture leading to an increase in cloud cover) and leave the total effect on the energy budget unresolved. *McGuire et al.* [2006] assume that changes in atmospheric water vapor due to imports from lower latitudes to be important for the climate of the Arctic but do not directly consider changes in atmospheric moisture related to changes in vegetation. In fact, they explicitly state that the only three ways in which climate is coupled to vegetation in the Arctic are albedo, energy partitioning at the surface, and the emission of greenhouse gases.

If tree expansion with climate warming occurs by deciduous broad-leaf trees as is suggested by some studies of future warming [*Rupp et al.*, 2000] and observations of past vegetation [*Edwards et al.*, 2005; *Peros et al.*, 2008] we might expect both short-wave and long-wave effects to be significant. The vegetation change we consider here is not the shift within the boreal forest from evergreen to deciduous, but an expansion of deciduous forest into previously unvegetated areas.

It is difficult to determine the timing of species invasion either from observations or modeling. Qualitative statements based on observations are made about rapid changes [*Edwards et al.*, 2005; *Chapin and Starfield*, 1997], and model estimates have been made for the rate of vegetation changes under future climate scenarios [*Danby and Hik*, 2007; *Rupp et al.*, 2000], but we have been unable to find an estimate of the potential rate of expansion of deciduous forest as we are considering in this Chapter. Based on observations and modeling work that has been done we suggest that it is not unreasonable to assume

that the expansion of deciduous trees could happen regionally on time scales shorter than the time for the climate to reach a new equilibrium ($\sim 10^3$ years).

This study is intended to identify which processes must be considered when evaluating the effects of vegetation changes on climate in the Arctic. We aim to constrain the relative effects of changes in short-wave (albedo) and long-wave (atmospheric water vapor from ET) forcing as a result of the expansion of deciduous broad-leaf trees at high northern latitudes.

5.3 Results

5.3.1 Climate Response to Expansion of Deciduous Forest

We performed four equilibrium simulations using a coupled atmosphere-land-carbon cycle global model, using two representations of vegetation cover (present day land cover and expanded vegetation with deciduous trees on bare ground north of $60°N$ (Figure 5.1)) and two ocean representations (interactive ocean (IO) and fixed ocean (FO) see methods section).

Anomalies, represented by $\Delta\phi$, are reported as the difference in climate variable ϕ simulated by the experiments with expanded forest cover and present day vegetation distribution with the same ocean module (either ΔV-IO or ΔV-FO). The vegetation interacts with climate through changing stomatal conductance, leaf area, and mass and hence albedo and transpiration. The ΔV-FO anomalies are an approximation of the response to direct forcing from vegetation expansion as any feedbacks associated with changes in ocean temperature or sea ice-cover are damped. The ΔV-IO anomalies can be considered as the whole earth system response including the response both to direct forcing and any associated feedbacks. The difference between the two anomalies, $\delta\Delta\phi = \Delta\phi$ (ΔV-IO) - $\Delta\phi$ (ΔV-FO), represents the additional feedback (from both land and ocean) experienced when the ocean and sea ice are allowed to adjust.

The expansion of trees at high northern latitudes leads to an annual mean near-surface atmosphere warming (ΔT) of 1 and 0.2 K over the Arctic (all area north of $60°N$) for ΔV-IO and ΔV-FO, respectively. The spatial pattern of ΔT is widespread in both the annual mean (Figure 5.2a and 5.2c) and throughout the year (Table 5.1). The phasing of peak ΔT is shifted to spring (in both FO and IO) in contrast to winter polar amplification associated with greenhouse gas forcing [*Christensen et al.*, 2007]. The annual mean ΔT comes about as a result of land and ocean feedbacks to the initial forcing from northern expansion of Arctic vegetation but does not have an identical spatial pattern (Figure 5.1, Figure 5.2a).

Feedbacks over both land and ocean (in IO runs) amplify the warming forced directly by changes in vegetation. Over the ocean, warming leads to a reduction in sea-ice area (13% in July, 26% in September) which, in turn, decreases ocean albedo by 8% (blue dashed line with "+", Figure 5.3a) and increases the evaporative flux by 21% in July (blue dashed line with "+", Figure 5.3b). Sea surface temperatures and ice area are held constant in the V-FO

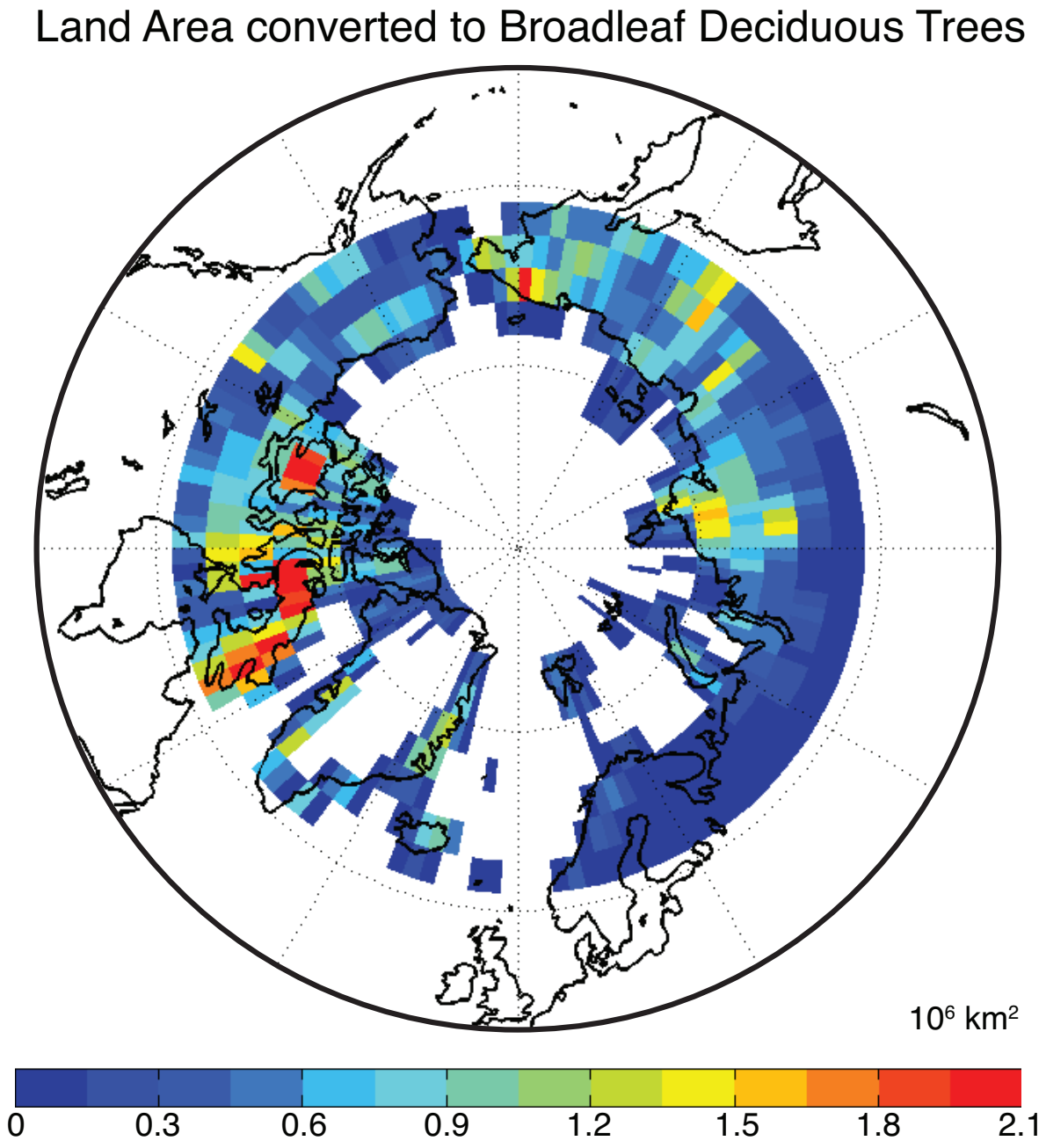

Figure 5.1. **Map of Vegetation Change:** Map showing the land area converted to broadleaf deciduous trees in V-FO and V-IO in units of 10^4 km^2. The converted area totals 3,000,000 km^2.

Month	Variable Name	Units	Fixed Ocean						Interactive Ocean					
			Land			Ocean			Land			Ocean		
April			C-FO	ΔV-FO	p	C-FO	ΔV-FO	p	C-IO	ΔV-IO	p	C-IO	ΔV-IO	p
	Surf. Air Temp.	K	265.04	**0.98**	**0.0070**	260.76	0.28	0.5043	265.56	**1.48**	**0.0038**	261.46	**1.46**	**0.0044**
	Water Vapor	kgm-2	6.09	0.03	0.9000	5.54	0.20	0.2890	6.21	0.32	0.1633	5.69	**0.39**	**0.0438**
	Low Cloud	fraction	0.58	-0.03	0.4483	0.63	-0.02	0.6728	0.58	-0.05	0.3287	0.64	-0.02	0.5771
	Albedo	albedo	0.51	**-0.07**	**0.0013**	0.60	-0.004	0.7917	0.50	-0.08	0.2556	0.59	-0.01	0.8429
	Latent Heat	Wm-2	10.07	**1.39**	**0.0305**	17.00	**-2.59**	**0.0000**	10.19	**1.52**	**0.0202**	16.28	0.65	0.1430
	Sensible Heat	Wm-2	12.15	1.30	0.0570	15.08	**-3.29**	**0.0000**	11.75	0.81	0.2229	14.60	**-1.86**	**0.0033**
	Ice Fraction	fraction	na	na	na	0.70	0.00	1.0000	na	na	na	0.70	-0.01	0.8755
	Precipitation	10-8m s-1	1.37	-0.03	1.0000	1.08	0.03	1.0000	1.38	-0.03	1.0000	1.16	0.00	1.0000
	Eff. Water Import	kg s-1	na	na	na	304.37	**-20.25**	**0.0000**	na	na	na	300.69	0.09	0.9736
	Transpiration	Wm-2	0.95	0.16	0.4582	na	na	na	1.12	0.20	0.4184	na	na	na
July														
	Surf. Air Temp.	K	284.88	0.51	0.2236	277.49	0.09	0.8375	284.98	**1.09**	**0.0455**	277.63	0.82	0.1794
	Water Vapor	kgm-2	19.35	0.38	0.1316	17.21	0.20	0.2850	19.38	**0.89**	**0.0047**	17.53	**0.50**	**0.0289**
	Low Cloud	fraction	0.49	-0.02	0.5910	0.75	-0.01	0.7834	0.48	-0.02	0.6227	0.75	-0.02	0.7138
	Albedo	albedo	0.24	-0.01	0.4898	0.23	0.00	0.9501	0.24	-0.01	0.8149	0.23	-0.02	0.6458
	Latent Heat	Wm-2	43.34	**4.16**	**0.0000**	12.49	**-1.10**	**0.0051**	44.20	**5.29**	**0.0000**	12.92	**2.66**	**0.0000**
	Sensible Heat	Wm-2	19.98	1.00	0.2169	4.34	-0.23	0.6746	20.13	0.52	0.4956	4.17	1.19	0.0558
	Ice Fraction	fraction	na	na	na	0.36	0.00	1.0000	na	na	na	0.36	-0.05	0.4100
	Precipitation	10-8m s-1	2.53	0.03	1.0000	1.17	-0.05	1.0000	2.46	0.13	0.9999	1.22	-0.01	1.0000
	Eff. Water Import	kg s-1	na	na	na	321.72	1.07	0.6725	na	na	na	313.68	**-8.38**	**0.0030**
	Transpiration	Wm-2	17.16	**4.61**	**0.0000**	na	na	na	17.65	**5.55**	**0.0000**	na	na	na

Table 5.1. **Change in Climate Model Variables with the Northward Expansion of Trees:** Variables of interest are shown from the four global climate model runs. Values are reported as the mean of the control run (C-FO and C-IO), the anomaly (ΔV-FO or ΔV-IO), and p-value of significance for spatial averages over either land (1.3 x $10^8 km^2$) or ocean (3.4 x $10^8 km^2$) area north of $60°N$. p-values of 0.05 or less indicate significance of at least 95% confidence and are shown in bold. The exception is effective water import (see Section 5.5.2) which is an estimate of the monthly average of atmospheric water vapor imported northward over the $60°N$ latitude line.

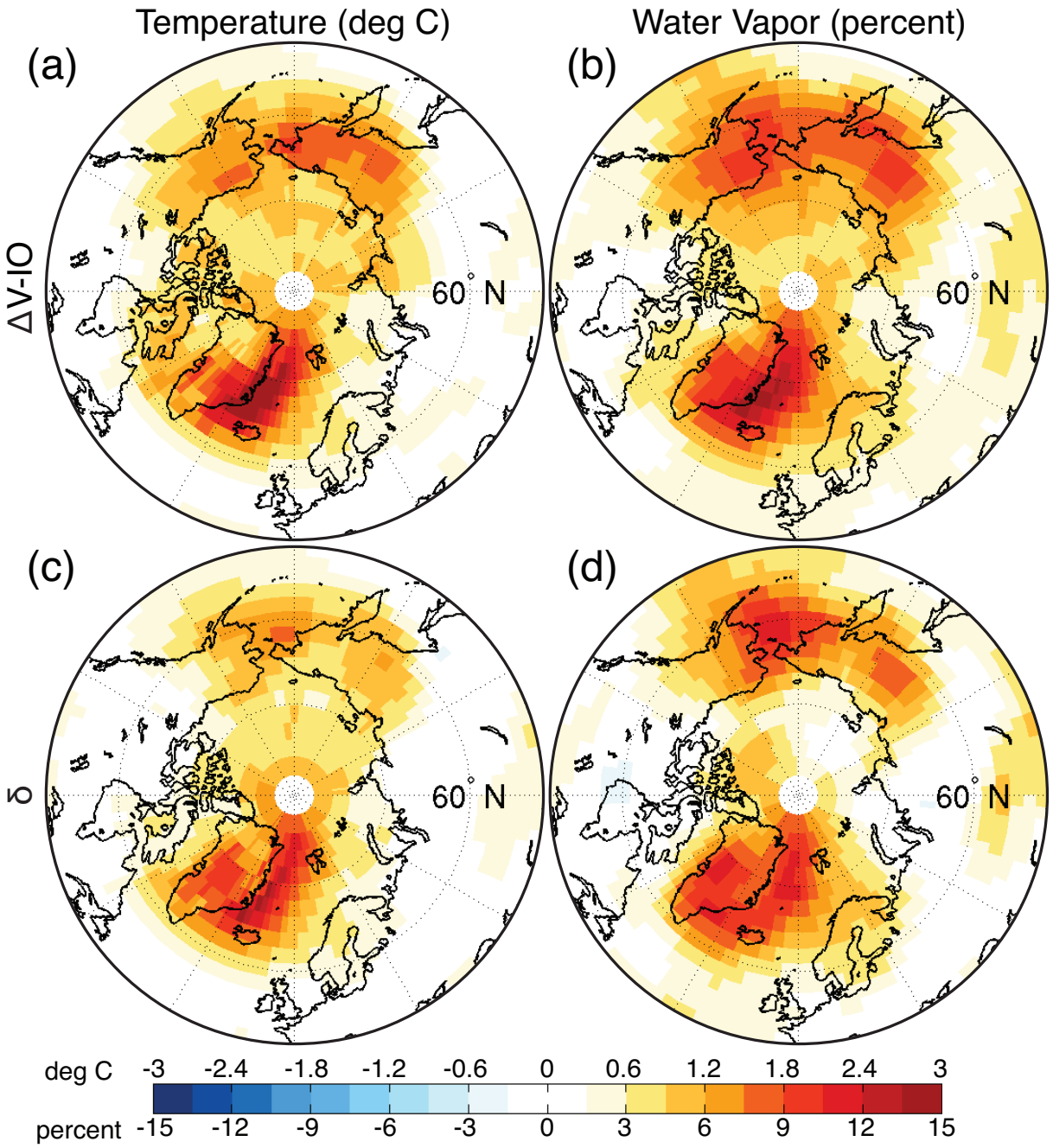

Figure 5.2. **Maps of Temperature and Water Vapor: (a)** The anomaly (ΔV-IO) in near surface atmospheric temperature in degrees Celsius (deg C) between a model experiment where trees are introduced on bare ground north of $60°N$ and a corresponding control run with no added trees. **(b)** The same as (a) for column water vapor in percent. **(c)** The difference δ (ΔV-IO-ΔV-FO) in near surface atmospheric temperature in deg C between two anomalies where trees are introduced on bare ground north of $60°N$, one with one with an interactive ocean model (V-IO) and the other with fixed ocean and sea ice (V-FO). **(d)** The same as (c) for column water vapor in percent.

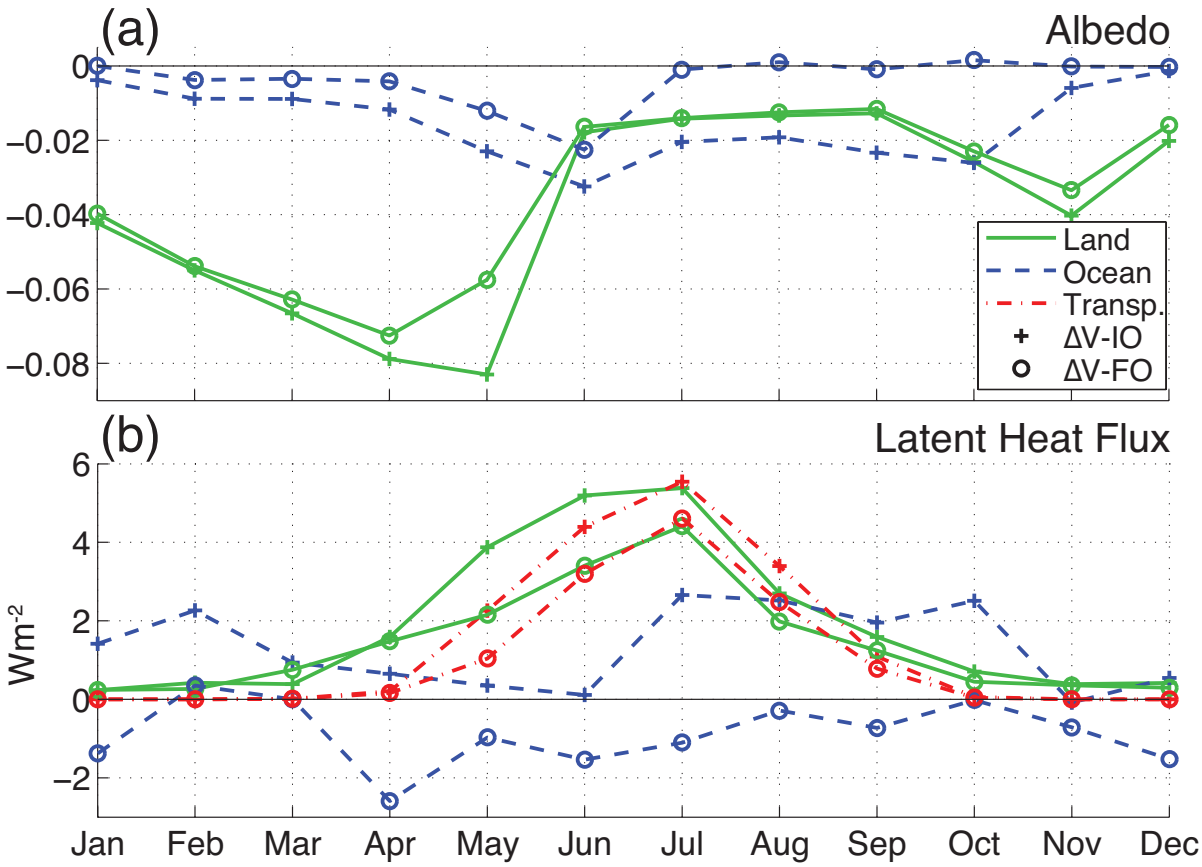

Figure 5.3. **Climatological Change in Albedo and Latent Heat Flux: (a)** Albedo anomalies averaged over land area north of $60°N$ (green solid line), ocean area north of $60°N$ (blue dashed line). Plus signs represent results from the interactive ocean model (ΔV-IO) and open circles represent results from the fixed ocean model (ΔV-FO). **(b)** Same as for (a) for latent heat flux anomalies and transpiration averaged over land area north of $60°N$ (red dashed-dot line).

case, but Δalbedo over the ocean is non-zero as snow and cloud cover are allowed to change (blue dashed line with "o", Figure 5.3a).

Low cloud cover anomalies are negative over both land and ocean (by up to 8% in ΔV-IO), but the change is not significant. The decrease in low cloud is due to an increase in stability from warming aloft. This is counter to the assertion of *Eugster et al.* [2000] who state (but do not test) that increases in ET from adding deciduous vegetation should increase cloudiness.

The expansion of trees in the Arctic has two direct implications for climate. First, there is a decrease in surface albedo over land in the springtime (green solid line in Figure 5.3a) as relatively dark stems and leaves cover bright snow. Leaf-out occurs across the Arctic in June, but stem area and a small residual leaf area are maintained throughout the year and mask snow area causing the largest albedo change when the sun comes out in April and May. Second, there is enhanced ET in the summer (red dashed-dot line in Figure 5.3b) leading

to an increase in atmospheric water vapor and consequently the greenhouse effect. The increase in ET also cools at the surface, but the latent cooling is too small to overcome the greenhouse warming from the increase in water vapor and direct heating from the increase in absorbed solar radiation leading to a net warming. Almost all ΔET over land comes from transpiration (compare green solid line and red dashed-dot line in Figure 5.2b) but with the increase in ET there is a slight compensating decrease in soil evaporation.

The addition of trees causes both a decrease in albedo and an increase in water flux from transpiration. Warmer air holds more water vapor than colder air thus we expect water vapor in the atmosphere will increase, somehow, in response to increases in temperature. It is very difficult, if not impossible, to isolate the initial effect of the water vapor directly released from enhanced transpiration (the "trigger") from the water vapor resulting from a subsequent increase in temperature (the "response"), as the distribution of both ΔT and $\delta\Delta$T co-varies with column water vapor increase (Figure 5.2).

Precipitation minus evaporation (P-E) is generally positive in the Arctic, i.e. there is a net import of water vapor from lower latitudes. The effective water vapor import anomalies, calculated by closing the water budget (see Section 5.5.2), shows a decrease in net import from lower latitudes in July for ΔV-IO and April ΔV-FO. The July reduction in import of water occurs when ΔT is the largest and corresponds with the summer growing season confirming that the increase in column water vapor comes from within Arctic inputs of water to the atmosphere.

5.3.2 Direct Comparison of Forcing Mechanisms

To explicitly separate the effects of albedo and changes in water vapor on the net radiative imbalance (ΔF) at the top of the atmosphere, we performed a sensitivity analysis using a one dimensional offline version of the radiation calculations from our atmospheric model (see Section 5.5.3). As with the full global model experiments, the FO conditions are used to estimate the direct effect of adding trees (as the response of the system is damped by the fixed ocean) and the $\delta\Delta$F (ΔV-IO minus ΔV-FO) is used to estimate feedbacks. Adding trees to the bare ground in the Arctic causes a direct increase in ΔF over land of 0.96 Wm^{-2} due to the decrease in albedo and of 0.95 Wm^{-2} due to increased water vapor from transpiration (shaded area of first two columns in Figure 5.4). The net radiative imbalance is amplified when the ocean is allowed to respond ($\delta\Delta$F, non-shaded area in columns in Figure 5.4) due to an increase in terrestrial productivity and a consequent (a) darkening of the land surface by additional leaves (0.23 Wm^{-2}), (b) additional increase in water vapor from ET (0.44 Wm^{-2}), and (c) indirect feedbacks from the increase in sea surface temperature and melting of sea ice (0.44 Wm^{-2} from ocean albedo and 0.94 Wm^{-2} from evaporation changes). With the full response of both atmosphere and ocean, the ΔF over land due to anomalous water vapor from ET is substantial and of the same magnitude as the direct ΔF due to albedo change.

Our hypothesis is as follows (Figure 5.5): expansion of deciduous forest causes a darkening of the surface due to the masking of bright snow by relatively dark stems and leaves and a

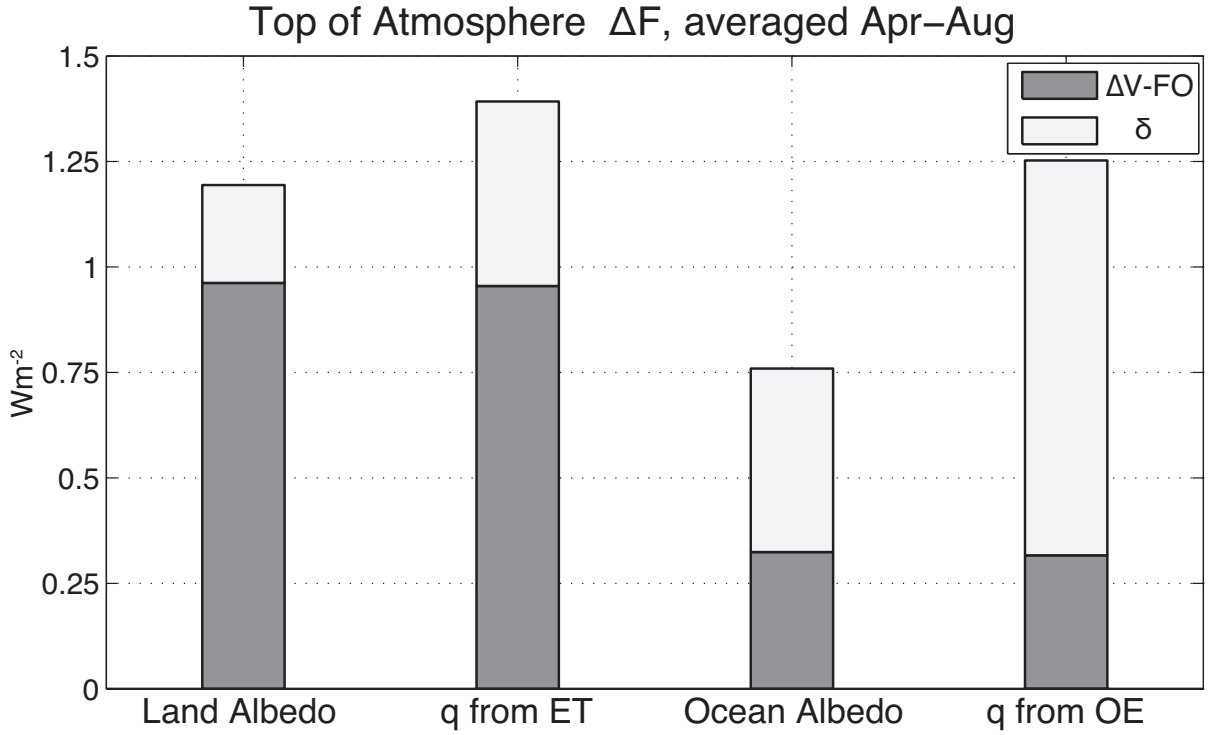

Figure 5.4. **Radiative Imbalance Due to Vegetation** The top-of-atmosphere net radiative imbalance (ΔF) caused by adding trees. Terms shown (from left to right) are ΔF due to changes in land albedo, water vapor changes from evapotranspiration (ET), ocean albedo, water vapor changes from ocean evaporation (OE). The total value of each column shows the full ΔF from ΔV-IO. The dark color shows the direct response of ΔV-FO and the light color shows the additional feedback δ (ΔV-IO-ΔV-FO) when the ocean and sea ice are allowed to respond.

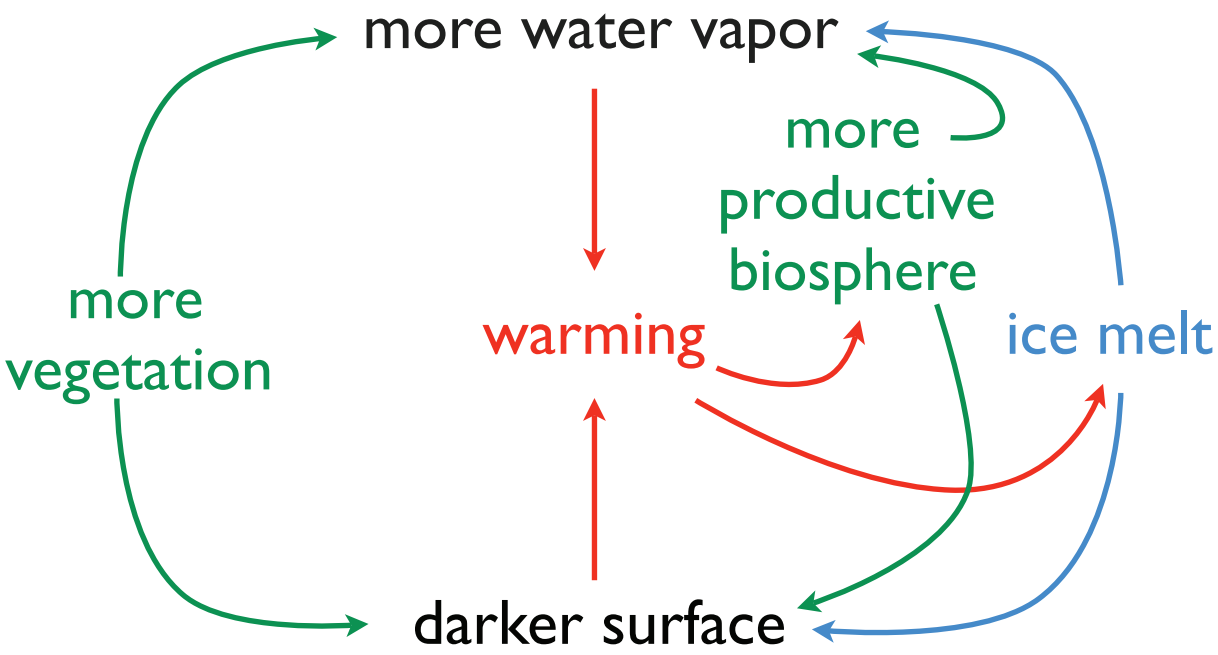

Figure 5.5. **Hypothesized Feedback Loop** Diagram representing the response and feedback of vegetation and sea-ice processes on climate at high northern latitudes.

concomitant increase in transpiration by the new leaves. These initial forcings, the lowering of albedo and increase in column water vapor, cause an increase in surface temperature over land. Water transpired by plants is efficiently mixed throughout the Arctic leading to surface warming over the ocean. Warming over the ocean, in turn, leads to the melting of sea ice (in ΔV-IO) resulting in a darker ocean surface as well as an increase in evaporation from the warmer ocean and newly ice-free water. This feedback chain warms the land surface further leading to greater productivity, lower albedo, and greater transpiration. The total temperature change seen in ΔV-IO includes both the initial forcing and all consecutive feedbacks listed here.

5.4 Discussion and Summary

We find that expansion of deciduous trees in the Arctic modifies both the short-wave and long-wave energy budgets, and initiates additional positive feedbacks associated with decreased sea-ice albedo and enhanced water vapor from evaporation from the Arctic Ocean. In particular, our analysis of the radiative energy imbalance due to the radiative forcing effects of water vapor is of the same order of magnitude as short-wave forcing from albedo changes. Thus, this study does not support the conventional wisdom (e.g. *Fischlin et al.* [2007]; *Chapin et al.* [2000]) that land albedo is the dominant means by which terrestrial vegetation interacts with climate at high-northern latitudes.

The temperature increase obtained in this experiment ($\sim$1 degree across the Arctic) is

modest in the global context but suggests that changing land cover in the Arctic could amplify an ongoing warming. The total ΔF over land due to water vapor from increased transpiration alone (1.4 Wm^{-2}), while regional, falls in between the estimated regional forcing (north of $60°N$) from CO_2 of an increase from 291ppm to 370ppm (1.1 Wm^{-2}) and from 291ppm to 437ppm (1.85 Wm^{-2}) [*Hansen et al.*, 2005].

The expansion of deciduous woodlands has been observed in past times of warming [*Edwards et al.*, 2005; *Peros et al.*, 2008], and is predicted by some studies of future warming [*Rupp et al.*, 2000]. Our study shows that the expansion of deciduous forest has a positive feedback on regional climate change. We suggest that an increase in deciduous woodland coverage might accelerate further expansion as warming provides more favorable growing conditions for deciduous trees at high northern latitudes. We find a number of aspects of hydrology counter to stated (but untested) assumptions about the climatic role of deciduous vegetation from ecological literature (e.g. an expected increase in cloud cover [*Eugster et al.*, 2000] or the role of ET [*Liu et al.*, 2005; *Chapin et al.*, 2000]). This study does not investigate the timescale associated with expansion and therefore we cannot say if this is a mechanism that might lead to abrupt change. However, it suggests that vegetation changes create a positive feedback through albedo and transpiration and produce a strong warming if they act in combination with sea-ice processes. The long-wave effects from changes in atmospheric moisture are not generally considered in studies of high latitude vegetation change, but we find the radiative forcing from water vapor to be the same magnitude as the direct short-wave forcing from albedo, indicating that the energy budget of the entire column should be considered and not just the balance of surface fluxes.

5.5 Methods

5.5.1 Climate Response to Expansion of Deciduous Forest

To investigate the role of vegetation changes at high latitudes, we use the National Center for Atmospheric Research (NCAR) Community Atmosphere and Land models with an interactive carbon cycle (CAM 3.0-CLM 3.5-CASA') [*Collins et al.*, 2006; *Doney et al.*, 2006; *Kiehl et al.*, 2006]. Bare ground (non-glacier, non-lake, non-vegetated land) north of $60°N$ is converted to broad-leaf deciduous trees and all previously designated vegetation is left unmodified, as are glaciers and lakes. The converted area totals 3,000,000 km^2 (1.75 times the size of Alaska). The primary regions converted to deciduous forest vegetation are the Canadian Archipelago and the Taymyr Peninsula and Chukotka in Russia (Figure 5.1). This particular conversion (from bare ground to forest) is used to make the simplest comparison possible by looking only at one vegetation transition. The exact distribution of vegetation used in these simulations may not reflect the regional patterns expected with warming, but the analysis is primarily focused on identifying the processes which control vegetation-climate interactions at these latitudes and not on the regional pattern of response.

The model control (C, standard land cover) and experiment (V, modified land cover) are each run with two representations of the ocean: an interactive slab ocean model (IO) with thermodynamic sea-ice [*Oleson et al.*, 2008], and a fixed ocean (FO) wherein sea surface temperature and sea-ice are set to the monthly-mean conditions in the C-IO control run. The four model runs are integrated for 30 years, and the results presented are averages of the last 20 years. The spin-up time of 10 years is sufficient to bring climate variables into equilibrium. Values in Table 5.1 are reported as the mean for one month (April and July) over either the land or ocean area north of $60°N$ except for water import, which is reported as the flux across the $60°N$ latitude line. Significance is calculated using an estimated 10 degrees of freedom for each 20-year period and reported as p-values where a p-value of 0.05 indicates that we reject the null hypothesis that the anomaly is zero with 95% confidence (shown in bold).

5.5.2 Water Budget of the Arctic

The Arctic north of $60°N$ can be considered an isolated system in the model in which all terms in the water budget can be explicitly identified. Inputs to atmospheric water vapor in the Arctic include fluxes from the land surface (transpiration, canopy evaporation, ground evaporation) fluxes from the ocean (evaporation) and imports of water via advection across the $60°N$ latitude line. The only export from the atmosphere is precipitation.

Due to the mass fixer in the non-conservative semi-lagrangian transport scheme we cannot calculate the actual model transport of water vapor [*Rasch and Williamson*, 1990]. We are able to estimate model transport but using this estimate we cannot close the water budget, even on annual time scales, indicating that the estimated transport is far from the actual transport experienced in the model. As the true model transport is unknown and the turnover time of water in the Arctic is assumed to be of order 10 days, we infer an effective transport for each month as the residual of P-E (including transpiration, canopy evaporation, ground evaporation and ocean evaporation). This effective import is used in Table 5.1.

5.5.3 Direct Comparison of Forcing Mechanisms

We calculate top-of-atmosphere energy imbalance (ΔF) for each forcing term using an offline version of the CAM 3.0 radiation calculations that we modified to run as a single column. The mean state of all variables in the offline radiation model are set to the mean of the C-IO control run, and the aerosols are prohibited from taking up water. For each experiment either surface albedo or specific humidity are modified while all other variables are held fixed.

Water vapor is partitioned into pools based on the relative contribution of each source term over the entire area north of $60°N$ compared to the only sink (precipitation). At steady state, the sum of all sources (ET, ocean evaporation (OE) and import) is equal to

precipitation (P), therefore we can show the relative contribution of each term as the ratio between the source and P. The estimate of water vapor q from one source (in this case ET) is calculated as:

$$q^{ET} = \left(\frac{ET}{P}\right) \cdot q^{total} \tag{5.1}$$

where q^{total} is the specific humidity (mass of water vapor), ET is evapo-transpiration and P is precipitation. The sensitivity of the radiative forcing in the 1D offline radiation model to each input of water vapor is then estimated by comparing the forcing in both short wave and long wave from q and $q + \Delta q$ where Δq is calculated as

$$\Delta q^{ET} = \left(\frac{ET}{P}\right)_{EXP} \cdot q^{total}_{EXP} - \left(\frac{ET}{P}\right)_{CON} \cdot q^{total}_{CON} \tag{5.2}$$

and EXP and CON denote values from the experiment and control calculations respectively. Offline radiation calculations were performed for the average monthly radiation conditions at 8 daily time steps and results shown are averaged over all times steps for the specified months. ΔF for $Delta$V-FO is calculated as the difference in the radiative fluxes from a run with albedo or specific humidity equal to the mean of V-FO and a run with albedo or specific humidity equal to the mean of C-FO while all other variables in the radiation calculation are held fixed as C-IO. ΔF is reported as an average over the entire Arctic region (north of $60°N$) for changes in water vapor and as an average over either Arctic Land or Ocean area for changes in Albedo.

Bibliography

Arrhenius, S., Uber die Reaktionsgeschwindigkeit bei der Inversion von Rohrzucker durch Sauren, *Zeitschrift für Physik Chemie*, *4*, 226–248, 1889.

Atkin, O., E. Edwards, and B. Loveys, Response of root respiration to changes in temperature and its relevance to global warming, *New Phytologist*, *147*(1), 141–154, 2000.

Aubinet, M., et al., Estimates of the annual net carbon and water exchange of forests: The EUROFLUX methodology, *Advances In Ecological Research, Vol 30*, *30*, 113–175, 2000.

Baldocchi, D., B. Hicks, and T. Meyers, Measuring Biosphere-Atmosphere Exchanges of Biologically Related Gases wiht Micrometorological Methods, *Ecology*, *69*(5), 1331–1340, 1988.

Baldocchi, D., et al., FLUXNET: A new tool to study the temporal and spatial variability of ecosystem-scale carbon dioxide, water vapor, and energy flux densities, *Bulletin of the American Meteorological Society*, *82*(11), 2415–2434, 2001.

Ball, J., I. Woodrow, and J. Berry, *Progress in photosynthesis research*, vol. 4, chap. A model predicting stomatal conductance and its contribution to the control of photosynthesis under different environmental conditions, pp. 221–224, Martinus Nijhoff, Dordrecht, The Netherlands, 1987.

Bonan, G., *Ecological Climatology: Concepts and Applications*, Cambridge Univ Pr, 2002.

Bonan, G. B., Forests and climate change: Forcings, feedbacks, and the climate benefits of forests, *Science*, *320*(5882), 1444–1449, doi:DOI10.1126/science.1155121, 2008.

Bonan, G. B., and S. Levis, Quantifying carbon-nitrogen feedbacks in the Community Land Model (CLM4), *Geophysical Research Letters*, *37*, doi:DOI10.1029/2010GL042430, 2010.

Bonan, G. B., D. Pollard, and S. L. Thompson, Effects Of Boreal Forest Vegetation On Global Climate, *Nature*, *359*(6397), 716–718, 1992.

Bonfils, C., N. de Noblet-Ducoure, P. Braconnot, and S. Joussaume, Hot desert albedo and climate change: Mid-Holocene monsoon in North Africa, *Journal of Climate*, *14*(17), 3724–3737, 2001.

Braconnot, P., S. Joussaume, and K. Taylor, Paleoclimate Modeling Intercomparison Project (PMIP), in *Proceedings of the Third PMIP Workshop. WCRP-111, WMO/TD-1007*, p. 271, Canada, 2000.

Braconnot, P., et al., Results of PMIP2 coupled simulations of the Mid-Holocene and Last Glacial Maximum - Part 1: experiments and large-scale features, *Climate of the Past*, *3*(2), 261–277, 2007a.

Braconnot, P., et al., Results of PMIP2 coupled simulations of the Mid-Holocene and Last Glacial Maximum - Part 2: feedbacks with emphasis on the location of the ITCZ and mid- and high latitudes heat budget, *Climate of the Past*, *3*(2), 279–296, 2007b.

Chapin, F., and A. Starfield, Time lags and novel ecosystems in response to transient climatic change in arctic Alaska, *Climatic Change*, *35*(4), 449–461, 1997.

Chapin, F., et al., Arctic and boreal ecosystems of western North America as components of the climate system, *Global Change Biology*, *6*(Suppl. 1), 211–223, 2000.

Charney, J., P. H. Stone, and W. J. Quirk, Drought in Sahara - Biogeophysical Feedback Mechanism, *Science*, *187*(4175), 434–435, 1975.

Charney, J. G., Dynamics of Deserts and Drought in Sahel, *Quarterly Journal of the Royal Meteorological Society*, *101*(428), 193–202, 1975.

Chiang, J., and C. Bitz, Influence of high latitude ice cover on the marine Intertropical Convergence Zone, *Climate Dynamics*, *25*(5), 477–496, doi:DOI10.1007/s00382-005-0040-5, 2005.

Christensen, J., et al., *in Climate Change 2007: The Scientific Basis, Contribution of Working Group I to the Fourth Assessment Report of the Intergovernmental Panel on Climate Change*, chap. 11, Regional Climate Projections, pp. 847–940, Cambridge University Press, Cambridge, United Kingdom, New York, NY, USA, 2007.

Claussen, M., and V. Gayler, The greening of the Sahara during the mid-Holocene: results of an interactive atmosphere-biome model, *Global Ecology and Biogeography Letters*, *6*(5), 369–377, 1997.

Claussen, M., C. Kubatzki, V. Brovkin, A. Ganopolski, P. Hoelzmann, and H. Pachur, Simulation of an abrupt change in Saharan vegetation in the mid-Holocene, *Geophysical Research Letters*, *26*(14), 2037–2040, 1999.

Collatz, G. J., J. T. Ball, C. Grivet, and J. A. Berry, Physiological and Environmental-Regulation of Stomatal Conductance, Photosynthesis and Transpiration - a Model That Includes a Laminar Boundary-Layer, *Agricultural and Forest Meteorology*, *54*(2-4), 107–136, 1991.

Collatz, G. J., M. Ribas-Carbo, and J. A. Berry, Coupled Photosynthesis-Stomatal Conductance Model for Leaves of C4 Plants, *Australian Journal of Plant Physiology*, *19*(5), 519–538, 1992.

Collins, W., et al., The formulation and atmospheric simulation of the Community Atmosphere Model version 3 (CAM3), *Journal of Climate*, *19*(11), 2144–2161, 2006.

Cook, B. I., G. B. Bonan, S. Levis, and H. E. Epstein, The thermoinsulation effect of snow cover within a climate model, *Climate Dynamics*, *31*(1), 107–124, doi:DOI10.1007/s00382-007-0341-y, 2008.

Cook, E. R., J. Esper, and R. D. D'Arrigo, Extra-tropical Northern Hemisphere land temperature variability over the past 1000 years, *Quaternary Science Reviews*, *23*(20-22), 2063–2074, 2004.

Cox, P. M., R. A. Betts, C. D. Jones, S. A. Spall, and I. J. Totterdell, Acceleration of global warming due to carbon-cycle feedbacks in a coupled climate model (vol 408, pg 184, 2000), *Nature*, *408*(6813), 750–750, 2000.

Danby, R. K., and D. S. Hik, Variability, contingency and rapid change in recent subarctic alpine tree line dynamics, *Journal of Ecology*, *95*(2), 352–363, doi:DOI10.1111/j.1365-2745.2006.01200.x, 2007.

D'Arrigo, R., B. Buckley, S. Kaplan, and J. Woollett, Interannual to multidecadal modes of Labrador climate variability inferred from tree rings, *Climate Dynamics*, *20*(2-3), 219–228, doi:DOI10.1007/s00382-002-0275-3, 2003.

Davidson, E., and I. Janssens, Temperature sensitivity of soil carbon decomposition and feedbacks to climate change, *Nature*, *440*(7081), 165–173, 2006.

Dickinson, R. E., M. Shaikh, R. Bryant, and L. Graumlich, Interactive canopies for a climate model, *Journal of Climate*, *11*(11), 2823–2836, 1998.

Doney, S. C., K. Lindsay, I. Fung, and J. John, Natural variability in a stable, 1000-yr global coupled climate-carbon cycle simulation, *Journal of Climate*, *19*(13), 3033–3054, 2006.

Dubayah, R., and J. Drake, Lidar remote sensing for forestry, *Journal of Forestry*, *98*(6), 44–46, 2000.

Edwards, M., L. Brubaker, A. Lozhkin, and P. Anderson, Structurally novel biomes: A response to past warming in Beringia, *Ecology*, *86*(7), 1696–1703, 2005.

Eugster, W., et al., Land-atmosphere energy exchange in Arctic tundra and boreal forest: available data and feedbacks to climate, *Global Change Biology*, *6*(1), 84–115, doi:10.1046/j.1365-2486.2000.06015.x, 2000.

Falge, E., et al., Gap filling strategies for defensible annual sums of net ecosystem exchange, *Agricultural and Forest Meteorology*, *107*(1), 43–69, 2001.

Falge, E., et al., Seasonality of ecosystem respiration and gross primary production as derived from FLUXNET measurements, doi:PIIS0168-1923(02)00102-8, 2002.

Farquhar, G., S. von Caemmerer, and J. Berry, A Biochemical-Model of Photosynthetic CO2 Assimilation in Leaves of C-3 Species, *Planta*, *149*(1), 78–90, 1980.

Fischlin, A., G. Midgley, J. Price, M. Parry, O. Canziani, J. Palutikof, P. van der Linden, and C. Hanson, *in Climate Change 2007: Impacts, Adaptation and Vulnerability. Contribution of Working Group II to the Fourth Assessment Report of the Intergovernmental Panel on Climate Change*, chap. 4, Ecosystems, their properties, goods and services, pp. 211–272, Cambridge University Press, 2007.

Foley, J. A., J. Kutzbach, M. T. Coe, and S. Levis, Feedbacks Between Climate And Boreal Forests During The Holocene Epoch, *Nature*, *371*(6492), 52–54, 1994.

Friedlingstein, P., J. L. Dufresne, P. M. Cox, and P. Rayner, How positive is the feedback between climate change and the carbon cycle?, *Tellus Series B-Chemical and Physical Meteorology*, *55*(2), 692–700, 2003.

Friedlingstein, P., et al., Climate-carbon cycle feedback analysis: Results from the (CMIP)-M-4 model intercomparison, *Journal of Climate*, *19*(14), 3337–3353, 2006.

Goulden, M., et al., Sensitivity of boreal forest carbon balance to soil thaw, *Science*, *279*(5348), 214–217, 1998.

Hansen, J., et al., Efficacy of climate forcings, *J. Geophys. Res*, *110*, D18,104, doi:10.1029/2005JD005776, 2005.

Hibbard, K., B. Law, M. Reichstein, and J. Sulzman, An analysis of soil respiration across northern hemisphere temperate ecosystems, *Biogeochemistry*, *73*(1), 29–70, doi:10.1007/s10533-004-2946-0, 2005.

Holland, E., J. Neff, A. Townsend, and B. McKeown, Uncertainties in the temperature sensitivity of decomposition in tropical and subtropical ecosystems: Implications for models, *Global Biogeochemical Cycles*, *14*(4), 1137–1151, 2000.

Janssens, I., and K. Pilegaard, Large seasonal changes in Q(10) of soil respiration in a beech forest, *Global Change Biology*, *9*(6), 911–918, 2003.

Jolly, D., et al., Biome reconstruction from pollen and plant macrofossil data for Africa and the Arabian peninsula at 0 and 6000 years, *Journal of Biogeography*, *25*(6), 1007–1027, 1998.

Joussaume, S., K. Taylor, and C. Saclay, Status of the paleoclimate modeling intercomparison project, in *Proceedings of the First International AMIP Scientific Conference: Monterey, California, USA, 15-19 May 1995*, p. 425, World Meteorological Organization, 1995.

Joussaume, S., et al., Monsoon changes for 6000 years ago: Results of 18 simulations from the Paleoclimate Modeling Intercomparison Project (PMIP), *Geophysical Research Letters*, *26*(7), 859–862, 1999.

Jung, M., M. Reichstein, and A. Bondeau, Towards global empirical upscaling of FLUXNET eddy covariance observations: validation of a model tree ensemble approach using a biosphere model, *Biogeosciences*, *6*(10), 2001–2013, 2009.

Kanamitsu, M., W. Ebisuzaki, J. Woollen, S. Yang, J. Hnilo, M. Fiorino, and G. Potter, NCEP-DOE AMIP-II reanalysis (R-2), *Bulletin of the American Meteorological Society*, *83*(11), 1631–1643, doi:DOI10.1175/BAMS-83-11-1631, 2002.

Kang, S. M., I. M. Held, D. M. W. Frierson, and M. Zhao, The response of the ITCZ to extratropical thermal forcing: Idealized slab-ocean experiments with a GCM, *Journal of Climate*, *21*(14), 3521–3532, doi:DOI10.1175/2007JCLI2146.1, 2008.

Kelliher, F., R. Leuning, M. R. Raupach, and E. D. Schulze, Maximum Conductances for Evaporation from Global Vegatation Types, *Agricultural and Forest Meteorology*, *73*(1-2), 1–16, 1995.

Kiehl, J., C. Shields, J. Hack, and W. Collins, The climate sensitivity of the Community Climate System Model version 3 (CCSM3), *Journal of Climate*, *19*(11), 2584–2596, 2006.

Langbein, W., Hydroclimate, in *The Encyclopedia of Atmospheric Sciences and Astrogeology,*, edited by R. Fairbridge, pp. 447–451, Reinhold, New York, 1967.

Levis, S., J. Foley, and D. Pollard, Potential high-latitude vegetation feedbacks on CO2-induced climate change, *Geophysical Research Letters*, *26*(6), 747–750, 1999.

Levis, S., G. B. Bonan, and C. Bonfils, Soil feedback drives the mid-Holocene North African monsoon northward in fully coupled CCSM2 simulations with a dynamic vegetation model, *Climate Dynamics*, *23*(7-8), 791–802, 2004.

Lintner, B., A. Gilliland, and I. Fung, Mechanisms of convection-induced modulation of passive tracer interhemispheric transport interannual variability, *Journal of Geophysical Research-Atmospheres*, *109*(D13), doi:DOI10.1029/2003JD004306, 2004.

Liu, H., J. Randerson, J. Lindfors, and F. Chapin, Changes in the surface energy budget after fire in boreal ecosystems of interior Alaska: An annual perspective, *Journal of Geophysical Research-Atmospheres*, *110*, doi:ARTND13101, 2005.

Lloyd, A., Ecological histories from Alaskan tree lines provide insight into future change, *Ecology*, *86*(7), 1687–1695, 2005.

Lloyd, J., and J. Taylor, On the Temperature-Dependence of Soil Respiration, *Functional Ecology*, *8*(3), 315–323, 1994.

Lorenz, E., Empirical orthogonal functions and statistical weather prediction, , Massachusetts Institute of Technology Department of Meteorology, Cambridge, Massachusetts, 1956.

McGuire, A. D., I. Chapin, F. S., J. E. Walsh, and C. Wirth, Integrated regional changes in arctic climate feedbacks: Implications for the global climate system, *Annual Review of Environment and Resources*, *31*, 61–91, doi:DOI10.1146/annurev.energy.31.020105.100253, 2006.

Monteith, J., Solar-Radiation and Productivity in Tropical Ecosystems, *Journal of Applied Ecology*, *9*(3), 747–766, 1972.

Monteith, J., Climate and Efficiency of Crop Production in Britan, *Philosophical Transactions of the Royal Society of London Series B-Biological Sciences*, *281*(980), 277–294, 1977.

Moss, R. H., et al., The next generation of scenarios for climate change research and assessment, *Nature*, *463*(7282), 747–756, doi:DOI10.1038/nature08823, 2010.

Nemani, R. R., C. D. Keeling, H. Hashimoto, W. M. Jolly, S. C. Piper, C. J. Tucker, R. B. Myneni, and S. W. Running, Climate-driven increases in global terrestrial net primary production from 1982 to 1999, *Science*, *300*(5625), 1560–1563, 2003.

North, G., T. Bell, R. Cahalan, and F. Moeng, Sampling errors in the estimation of empirical orthogonal functions, *Mon. Wea. Rev*, *110*(5), 699–706, 1982.

Oleson, K. W., et al., Improvements to the Community Land Model and their impact on the hydrological cycle, *Journal of Geophysical Research-Biogeosciences*, *113*(G01021), doi: ARTNG01021, 2008.

Oyama, M. D., and C. A. Nobre, A new climate-vegetation equilibrium state for tropical South America, *Geophysical Research Letters*, *30*(23), 2003.

Parton, W., D. Schimel, C. C.V., and D. Ojima, Analysis of Factors Controlling Soil Organic-Matter Levels in Great-Plains Grassland, *Soil Science Society of America Journal*, *51*(5), 1173–1179, 1987.

Parton, W. J., J. Stewart, and C. Cole, Dynamics of C, N, P and S in Grassland Soils - A Model, *Biogeochemistry*, *5*(1), 109–131, 1988.

Peros, M. C., K. Gajewski, and A. E. Viau, Continental-scale tree population response to rapid climate change, competition and disturbance, *Global Ecology and Biogeography*, *17*(5), 658–669, doi:DOI10.1111/j.1466-8238.2008.00406.x, 2008.

Potter, C. S., J. T. Randerson, C. B. Field, P. A. Matson, P. M. Vitousek, H. A. Mooney, and S. A. Klooster, Terrestrial Ecosystem Production - a Process Model-Based on Global Satellite and Surface Data, *Global Biogeochemical Cycles*, *7*(4), 811–841, 1993.

Prentice, I., S. Harrison, D. Jolly, and J. Guiot, The climate and biomes of Europe at 6000 yr BP: Comparison of model simulations and pollen-based reconstructions, *Quaternary Science Reviews*, *17*(6-7), 659–668, 1998.

Prentice, I. C., M. Heimann, and S. Sitch, The carbon balance of the terrestrial biosphere: Ecosystem models and atmospheric observations, *Ecological Applications*, *10*(6), 1553–1573, 2000.

Rasch, P. J., and D. L. Williamson, On shape-preserving interpolation and semi-Lagrangian transport, *SIAM J. Sci. Stat. Comput.*, *11*(4), 656–687, doi:10.1137/0911039, 1990.

Reichstein, M., et al., Modeling temporal and large-scale spatial variability of soil respiration from soil water availability, temperature and vegetation productivity indices, *Global Biogeochemical Cycles*, *17*(4), 2003.

Reichstein, M., et al., On the separation of net ecosystem exchange into assimilation and ecosystem respiration: review and improved algorithm, *Global Change Biology*, *11*(9), 1424–1439, doi:DOI10.1111/j.1365-2486.2005.001002.x, 2005.

Running, S. W., and J. Coughlan, A General-model of forest ecosystem processes for regional applications .1. Hydrologic balance, canopy gas-exchange and primary production processes, *Ecological Modelling*, *42*(2), 125–154, 1988.

Rupp, T., F. Chapin, and A. Starfield, Response of subarctic vegetation to transient climatic change on the Seward Peninsula in north-west Alaska, *Global Change Biology*, *6*(5), 541–555, 2000.

Russell, J., and J. Wallace, Annual carbon dioxide drawdown and the Northern Annular Mode, *Global Biogeochemical Cycles*, *18*(1), doi:DOI10.1029/2003GB002044, 2004.

Schimel, D., B. H. Braswell, E. A. Holland, R. McKeown, D. Ojima, T. Painter, W. J. Parton, and A. Townsend, Climatic, Edaphic, and Biotic Controls over Storage and Turnover of Carbon in Soils, *Global Biogeochemical Cycles*, *8*(3), 279–293, 1994.

Snyder, P., C. Delire, and J. Foley, Evaluating the influence of different vegetation biomes on the global climate, *Climate Dynamics*, *23*(3-4), 279–302, doi:DOI10.1007/s00382-004-0430-0, 2004.

Solomon, S., D. Qin, M. Manning, Z. Chen, M. Marquis, K. Averyt, M. Tignor, and H. Miller, *Climate change 2007: the physical science basis*, Cambridge University Press Cambridge, New York, Melbourne, Madrid, Cape Town, Singapore, São Paulo, Delhi, 2008.

Street-Perrott, F., D. Marchand, N. Roberts, and S. Harrison, Global lake-level variations from 18, 000 to 0 years ago: A palaeoclimate analysis, , DOE/ER/60304-H1, Oxford Univ.(UK). Geography School, 1989.

Swann, A. L., I. Y. Fung, S. Levis, G. B. Bonan, and S. C. Doney, Changes in Arctic vegetation amplify high-latitude warming through the greenhouse effect, *Proceedings of the National Academy of Sciences of the United States of America*, *107*(4), 1295–1300, doi:DOI10.1073/pnas.0913846107, 2010.

Tarasov, P., et al., Present-day and mid-Holocene biomes reconstructed from pollen and plant macrofossil data from the former Soviet Union and Mongolia, *Journal of Biogeography*, *25*(6), 1029–1053, 1998.

Tjoelker, M., J. Oleksyn, and P. Reich, Modelling respiration of vegetation: evidence for a general temperature-dependent Q(10), *Global Change Biology*, *7*(2), 223–230, 2001.

Tucker, C. J., Red and photographic infared linear combinations for monitoring vegetation, *Remote Sensing of Environment*, *8*(2), 127–150, 1979.

Valentini, R., et al., Respiration as the main determinant of carbon balance in European forests, *Nature*, *404*(6780), 861–865, 2000.

Van't Hoff, J., Lectures on theoretical and physical chemistry. Part 1. Chemical dynamics, *Trans. Lehfeldt RA. Edward Arnold, London*, pp. 224–229, 1898.

Webster, K. L., I. F. Creed, M. D. Skowronski, and Y. H. Kaheil, Comparison of the Performance of Statistical Models that Predict Soil Respiration from Forests, *Soil Science Society of America Journal*, *73*(4), 1157–1167, doi:10.2136/sssaj2008.0310, 2009.

Woodhouse, C. A., and J. T. Overpeck, 2000 years of drought variability in the central United States, *Bulletin of the American Meteorological Society*, *79*(12), 2693–2714, 1998.

Woodward, F. I., M. R. Lomas, and T. Quaife, Global responses of terrestrial productivity to contemporary climatic oscillations, *Philosophical Transactions of the Royal Society B-Biological Sciences*, *363*(1504), 2779–2785, doi:DOI10.1098/rstb.2008.0017, 2008.

Zeng, N., J. D. Neelin, K.-M. Lau, and C. J. Tucker, Enhancement of Interdecadal Climate Variability in the Sahel by Vegetation Interaction, *Science*, *286*(5444), 1537–1540, doi:10.1126/science.286.5444.1537, 1999.